Adaptive Clutter Rejection Filters
For Airborne Doppler Weather Radar
Applied To The
Detection Of Low Altitude Windshear

by

Byron M. Keel

Technical Report #11
December 4, 1989

Radar Systems Laboratory
Electrical and Computer Engineering Department
Clemson University
Clemson, SC 29634-0915

NASA

(NASA-CR-186211) ADAPTIVE CLUTTER REJECTION
FILTERS FOR AIRBORNE DOPPLER WEATHER RADAR
APPLIED TO THE DETECTION OF LOW ALTITUDE
WINDSHEAR (Clemson Univ.) 190 p   CSCL 17I

N90-14453

Unclas
G3/32 0253323

ACKNOWLEDGEMENTS

In the filter evaluation process, post-filtered pulse-pair width estimates and power levels are also used to measure the effectiveness of the filters.

The results presented support the use of an adaptive clutter rejection filter for reducing the clutter induced bias in pulse-pair estimates of windspeed. The adaptive clutter rejection filter is also shown to perform better than one clutter rejection filter commonly used in land based air traffic control radar systems.

TABLE OF CONTENTS

Table of Contents (Continued)

Table of Contents (Continued)

LIST OF TABLES

LIST OF FIGURES

List of Figures (Continued)

List of Figures (Continued)

List of Figures (Continued)

CHAPTER I
MICROBURST DETECTION

Microburst

The contribution of microbursts to aircraft accidents was first recognized by Fujita [1] in the late 1970's while investigating the crash of Eastern 66 on June 24, 1975 at John F. Kennedy Airport in New York City. Between 1964 and 1985, an estimated 26 major aircraft accidents resulting in 626 fatalities and over 200 injures have been attributed to the microburst described by Fujita. Based on these figures, the FAA and NASA have proposed the use of airborne Doppler weather radar for the detection of a microburst in the vicinity of airport runways [2].

The term "microburst" was first used by Fujita to describe the vertical flow of wind which results in an horizontal outflow in all directions upon impact with the ground (Figure 1). The horizontal outflow may extend in all directions within a 4km radius. The duration of a microburst is usually less than 10 minutes. This limited duration and the geographical boundaries of the horizontal outflow permit microbursts to go undetected by non-Doppler radars or ground-based anemometers [1]. Horizontal outflows extending in radius greater than 4km are termed macroburst and are easier to detect due to their large physical size.
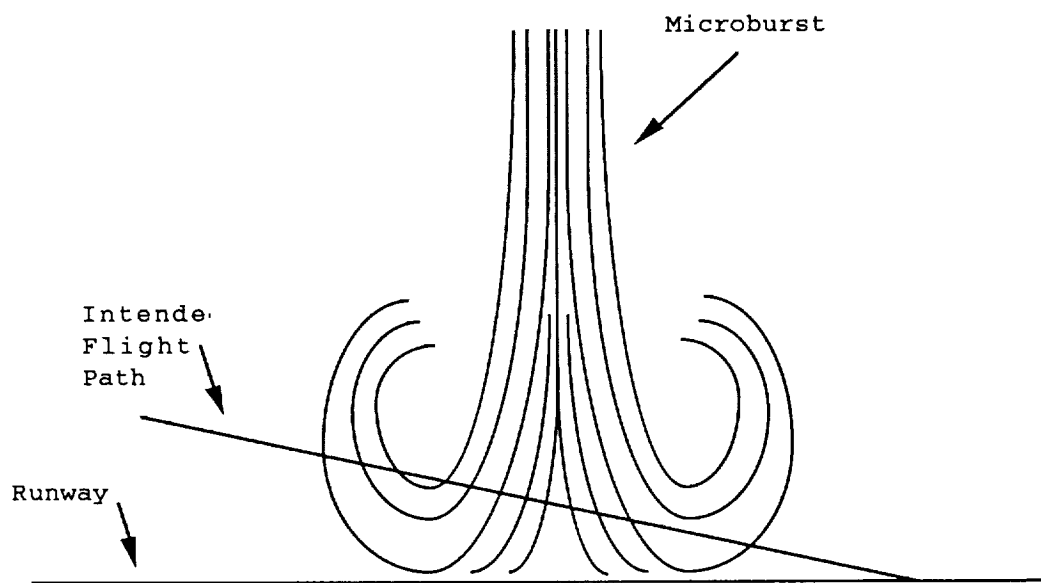
Figure 1. Illustration of the outflow from a microburst.

The aviational hazard associated with a microburst exists on final approach to a runway or on takeoff (Figure 1). Headwinds are encountered by an aircraft on final approach as it moves through one side of the microburst. The pilot must then compensate to bring the aircraft down to the glide slope. At this point, the pilot has reduced his speed and is vulnerable to the unexpected downflow and tailwinds associated with the other side of the microburst. On takeoff, the downflow and tailwinds associated with the microburst combine to reduce the necessary lift required by the aircraft.

Microburst can be subdivided into two categories based on the amount of precipitation present. A microburst containing high levels of precipitation is defined as being a "wet microburst". A low level of precipitation within the microburst leads to the term "dry microburst". A high cloud base may allow time for evaporation in dry regions leading to the low levels present in the dry microburst.

The precipitation present in a microburst provides the necessary targets for a Doppler weather radar which can be used to measure horizontal components of wind speed with respect to the aircraft. A wet microburst contains a sufficient target base to provide radar returns representative of the relative windspeed within the microburst. The detection of windspeed within a dry microburst is hampered due to the decreased target concentration.

A signature based on average horizontal components of windspeed relative to position within a microburst can be defined. This signature develops as the horizontal component of windspeed increases with distance from the center of the microburst. Figure 2 gives an example of the characteristic "S" curve which relates the average horizontal component of windspeed within a microburst to distance from the center of the microburst. The Doppler weather radar proposed by the FAA and NASA is intended to obtain information about average windspeed versus range and thus identify the presence of a microburst.

Pulsed Doppler Weather Radar

A Doppler weather radar is based on the Doppler effect defined by Christian Johann Doppler. The Doppler effect, applied to radar, relates the frequency shift in an electromagnetic signal to the relative motion of the target. The linear approximation between the frequency shift, f_d, and the speed of the target, v, is given by

$$f_d = 2f_t v/c. \tag{1}$$

The slope of this line is twice the ratio of the transmitted frequency, f_t, to the speed of light, c. Figure 3 illustrates the shift in frequency of an electromagnetic signal incident upon a target with velocity, v.

A Doppler radar can also be used to supply ranging information. This is accomplished by pulse modulating the
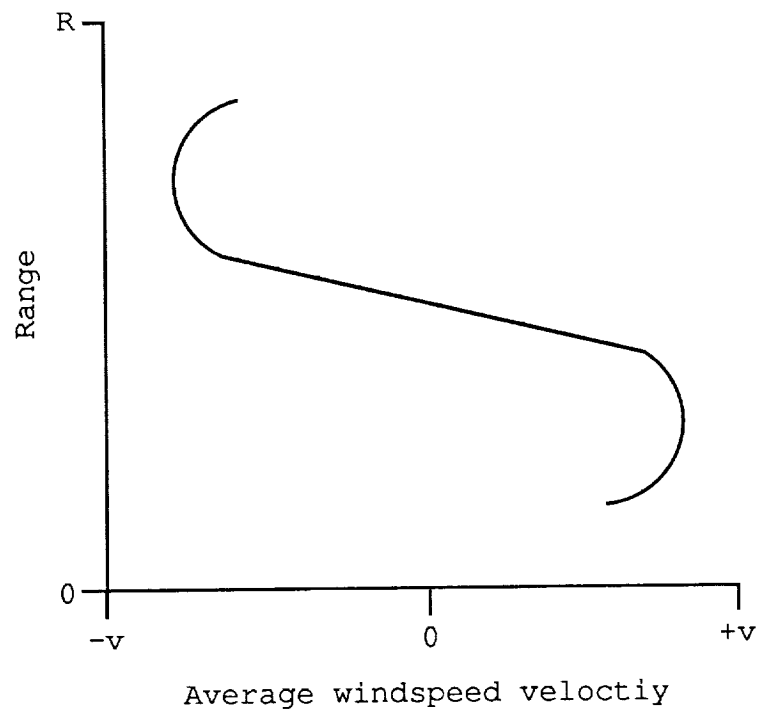
Figure 2. "S" curve associated with a microburst.
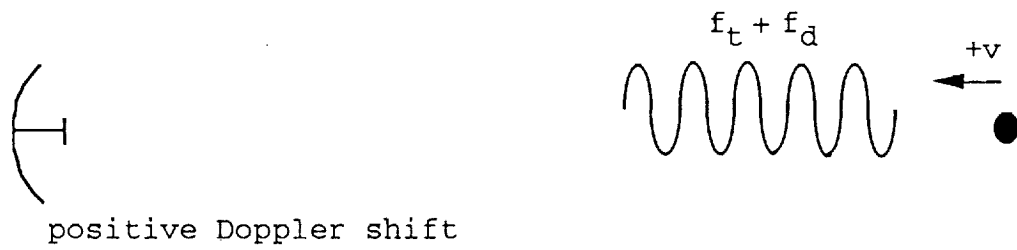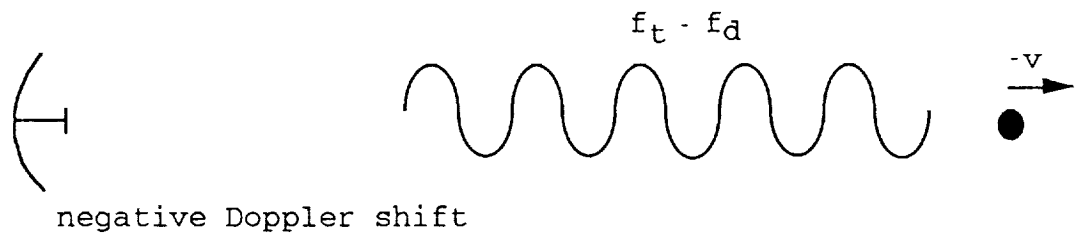
Figure 3. Doppler return from a moving target.

transmitted waveform and gating the return signal at equal time intervals corresponding to successive target ranges (range bins or range cells) before the next pulse is transmitted. This is illustrated in Figure 4. The pulse repetition frequency, PRF, limits the maximum unambiguous range, R_u, where

$$R_u = c/2PRF \qquad (2)$$

shows that the transmitted signal must traverse its path to and from the target during the time interval allotted by the PRF. The ability to resolve two targets, a distance, D, apart, is also related to the PRF through

$$D = c(\tau/2) \qquad (3)$$

where τ is the pulse width.

The pulse modulation of the transmitted signal requires a coherent phase between pulses in order to extract frequency shift information. This is accomplished by maintaining a coherent oscillator (COHO) within the radar. The output from the COHO is at an intermediate frequency, IF, and is mixed with a stable local oscillator (STALO) to reach the required transmission frequency (RF). The signal to be transmitted is then pulse modulated and amplified.

The return signal, received during the gating process, is demodulated using the STALO in order to convert to the IF. In order to resolve the sign of the frequency shift, a second IF signal is formed which has a 90 degree phase shift with
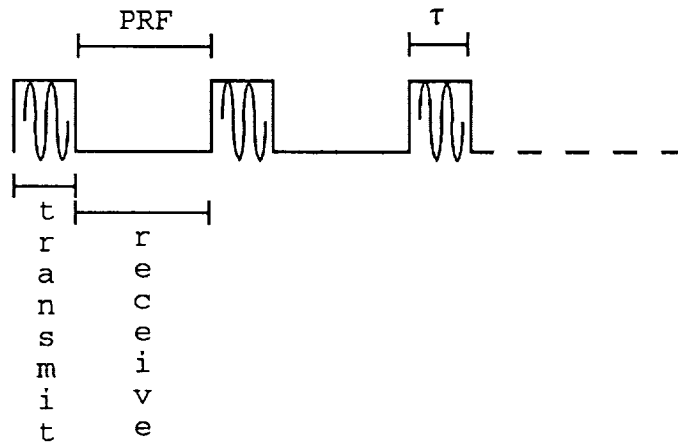
(a) Transmit and receive cycles.
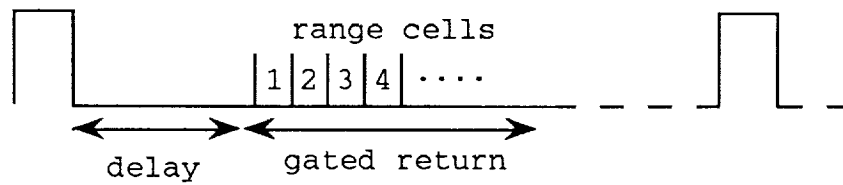
(b) Gated return.

Figure 4. Pulse modulation for a Doppler radar.

respect to the received IF signal. The two channels are termed inphase (I channel) and quadrature (Q channel) corresponding to the received IF signal and the 90 degree phase shifted version, respectively. A second demodulation is required to convert the IF signal to the Doppler frequency range. This is accomplished by mixing the COHO with the I and Q signals. The gated return is finally sampled and its value stored for future processing. Figure 5 shows a block diagram of a coherent pulsed Doppler radar [3].

The samples taken for a particular range cell over successive pulses are stored and then processed to determine the average target speed at that range. The pulse repetition frequency is also the sampling frequency for the range cell data since one sample is obtained per pulse per range cell. This sampling frequency, PRF, is small compared to the sampling frequency between successive range cells and therefore provides the smaller bandwidth needed to resolve the Doppler frequencies using conventional Fourier analysis or parametric spectral estimation.

Pulse-Pair Estimator

The precipitation present in a microburst yields multiple point targets within a range cell. The radar return from a range cell therefore consists of the sum of the returns from the individual targets (raindroplets). Fourier spectral analysis of this range cell data reveals that the
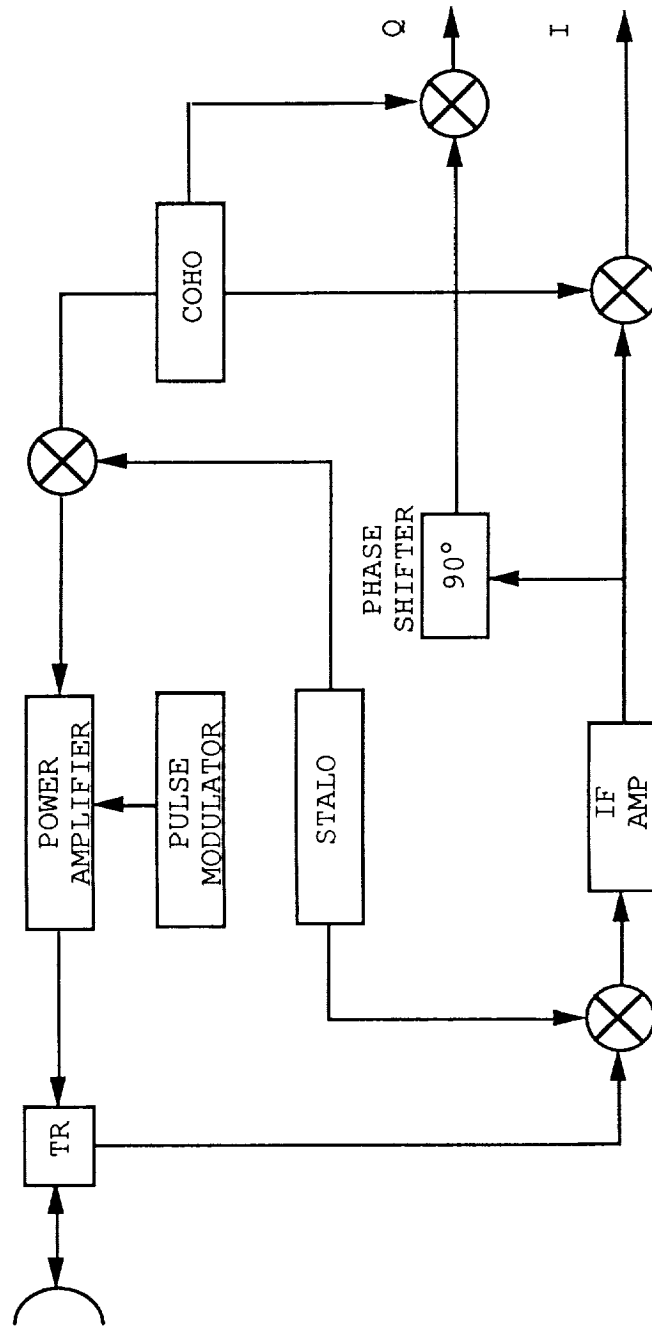
Figure 5. Block diagram of a coherent pulsed Doppler radar.

estimated windspeed distribution can frequently be described as Gaussian in form with an associated mean and width [4].

The pulse-pair algorithm developed by Rummler [5] can be used to estimate the windspeed mean and width within a range cell. The algorithm uses estimates of the zeroth and first lag of the autocorrelation to determine the mean and width estimates. The pulse-pair width estimate, w, for the range cell data described previously can be written as

$$w = \frac{(PRF)^2}{2(\pi)^2} \left[1 - \frac{|R(1)|}{R(0)} \right] . \tag{4}$$

The autocorrelation lags in Equation 4 are estimated using

$$R(1) = \frac{1}{N} \sum_{n=0}^{N-1} V^*(n) V(n+1) \tag{5}$$

and

$$R(0) = \frac{1}{N} \sum_{n=0}^{N-1} V^*(n) V(n) \tag{6}$$

where $V(n)$ is the sampled complex time series and N is the total number of samples. The pulse-pair mean estimate, f, takes the form

$$f = \frac{(PRF)\{ARG[R(1)]\}}{2\pi} . \tag{7}$$

In comparing the pulse-pair method to Fourier based methods for estimating the mean and width, it can be shown that the

pulse-pair method is superior in cases where the signal-to-noise ratio, SNR, is small [6]. The pulse-pair method also offers an advantage in terms of calculation speed over Fourier based methods.

F-Factor

A hazard index or F-factor has been defined by Bowles [7] to measure the danger associated with microburst. The F-factor takes the form

$$F = W'_x/g - W_h/v \qquad (8)$$

where W'_x is the rate of change of the wind velocity along the flight path, v is the relative speed of the aircraft, g is the acceleration due to gravity, and W_h is the vertical component of wind velocity along the flight path. A forward-looking Doppler radar can only measure radial velocities of wind along the flight path of the airplane and therefore estimates of W_h can not be obtained. The radial component, F_R, can be written as

$$F_R = (v/g)(\Delta W_x/\Delta R) \qquad (9)$$

where ΔW_x is the change in radial velocity between range bins and ΔR is the distance between range bins. Estimates of the average radial veloctiy, W_x, can be obtained from the return data using the pulse-pair algorithm.

Statement of the Problem

The ability of an airborne Doppler radar system to detect a microburst in the near terminal area depends heavily on the capabilities of that system to measure the horizontal component of windspeed versus range. The reflectivity associated with the precipitation present in the microburst is not the only contributing factor in this detection problem. Clutter return from objects in the near terminal area contributes to a loss in the signal-to-noise ratio and can impose a bias on estimates of windspeed. This thesis looks at reducing the effect of ground clutter on the pulse-pair mean estimates of windspeed through the use of clutter rejection filters based on modeling the clutter return in the near terminal area.

The modeling techniques and coefficient estimation algorithms used in this thesis are discussed in Chapter II. Emphasis is placed on modeling the clutter as an autoregressive process and using an adaptive least squares prediction error lattice filter for determining the values of the model coefficients. Block processing and gradient adaptive algorithms are also discussed as alternative means for determining the model coefficients.

In Chapter III, a model is used to generate microburst and clutter return data. The model was developed by NASA and uses actual clutter data taken from the Denver-Stapleton airport. Inputs to the model include microburst and radar system parameters. Using data generated from this model,

analysis of the pulse-pair estimates and power levels of a dry and a wet microburst are made in order to develop test cases for evaluating the performance of the adaptive clutter rejection filters. Spectral analysis and pulse-pair estimate analysis of the clutter returns are also given in Chapter III. The model clutter is observed to have the majority of its power contained in a narrow band of the Doppler spectrum and centered around zero. The clutter spectrum for this data set does not contain specular components as in the case of return from traffic on a nearby highway but this scenario should not be ruled out.

The optimum clutter rejection filter is defined in Chapter IV, based on modeling the clutter in each range cell as an AR process. A complex normalized form of the least squares adaptive prediction error lattice filter, which offers possible fixed point implementation and involves fewer update equations than the unnormalized form, is used to determine the model coefficients. Analysis of pulse-pair estimates and power levels after filtering reflects the ability of the filters to remove the clutter without further biasing the pulse-pair estimates. Two other filtering schemes, one based on modeling the clutter to obtain a single filter for use over several range cells, and one based on conventional filtering techniques used in land based air traffic control radar systems, are also evaluated.

Chapter V contains conclusions and recommendations for future work. Appendix A contains a derivation of a complex

least squares adaptive lattice structure. Appendix B contains a listing of the parameters used in the simulation model. Appendix C and D contain spectral estimates of dry microburst returns with and without clutter, respectively. Appendix E gives spectral estimates of the clutter return. Appendix F and G give the filter magnitude and phase response, respectively, based on modeling the clutter in each range cell. Appendix H, I, and J contain filtered spectral estimates where the filters were based on modeling the clutter in each range, modeling the clutter in range cell 20, and using a pulse canceller, respectively.

CHAPTER II

CLUTTER MODELING

Introduction

Data collected from a range cell may contain both weather return and ground clutter (e.g. return from ground structures). Figure 6 represents a range cell containing a return from a microburst in addition to clutter. The clutter tends to bias the pulse-pair estimates of windspeed mean and width. Clutter may be centered around zero Doppler due to stationary objects on the ground or very specular in nature as in the case of traffic on a nearby highway.

With clutter and weather spectra separated in frequency, a filtering scheme should be able to reduce the effects of clutter on the pulse-pair estimates of windspeed. Haykin [8] has suggested a means for modeling the clutter in the airport terminal area as an autoregressive, AR, process. The model can then be used to eliminate the clutter from the return signal. Gibson [9] has also used this modeling technique to design adaptive clutter rejection filters for use in an air traffic enviroment. The clutter rejection filters based on modeling the clutter offer a better estimate of the character of the clutter spectrum than the traditional moving-target indicator [9], MTI, filter. The MTI filter is a high pass filter in the form of a pulse canceller. This filter is used
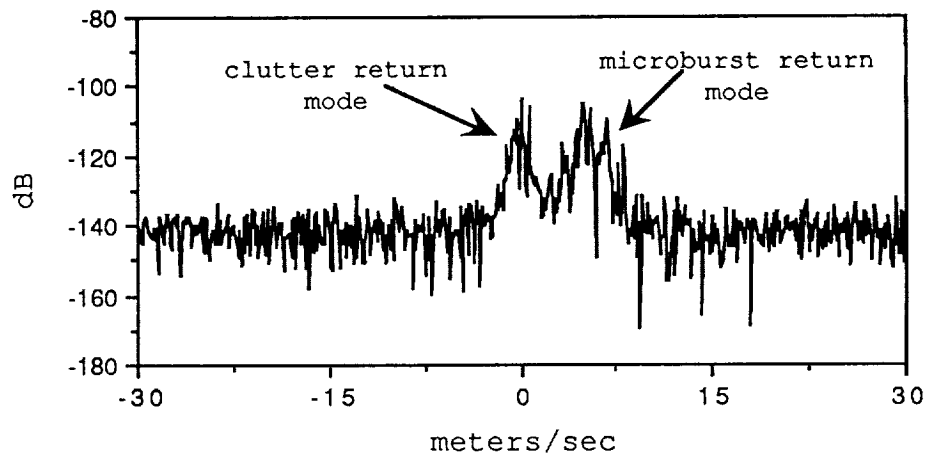
Figure 6. Fourier spectral estimate of a range cell containing microburst and clutter return.

as a gross means for removing the clutter and does not take into account the spectrum of the clutter other than the fact that it is usually centered around zero Doppler.

ARMA Modeling

The AR process used for modeling clutter in the airport terminal area is actually an extension of the autoregressive-moving average, ARMA, model [10] used to describe a stochastic process. The ARMA model expresses the stochastic process in terms of a linear difference equation

$$y_T = -\sum_{k=1}^{N} a_k \, y_{T-k} + \sum_{k=0}^{M} d_k \, u_{T-k} \qquad (10)$$

where $d(0) = 1$. The input, u_T, to the system is assumed to be generated by a white noise process. The z-transform of the transfer function between the input, u_T, and the output, y_T, in Equation (10) can be written as

$$H(z) = \frac{D(z)}{A(z)} \qquad (11)$$

where

$$A(z) = 1 + \sum_{k=1}^{N} a_k \, z^{-k} \qquad (12)$$

and

$$D(z) = 1 + \sum_{k=1}^{M} d_k \, z^{-k} . \qquad (13)$$

The power spectrum of the output of the ARMA model, $P_y(e^{j\omega})$, takes the form

$$P_y(e^{j\omega}) = |H(e^{j\omega})|^2 P_u(e^{j\omega}) \tag{14}$$

where $P_u(e^{j\omega})$ and $H(e^{j\omega})$ are z-transforms of the input and transfer function, respectively, evaluated at $z = e^{j\omega}$ [11].

AR Modeling

Wold's decomposition theorem [10] allows for an approximation of the ARMA model given in Equation (10). The model of interest is an autoregressive, AR, model of the form

$$y_T = -\sum_{k=1}^{N} a_k \, y_{T-k} + u_T \tag{15}$$

with an associated transfer function

$$H_{AR}(z) = \frac{1}{A(z)} \, . \tag{16}$$

Wold's decomposition theorem states that an ARMA model of order (N,M) can be represented as an AR model of possibly infinite order.

The power spectrum for the AR process in Equation (15) can be written as

$$P_{AR}(f) = \frac{\sigma^2 T}{\left| \, 1 + \sum_{k=1}^{N} a_k \, \exp(-j2\pi f T k) \, \right|^2} \tag{17}$$

where σ^2 is the variance of the input white noise process, and T is the sampling period. The input to the system was assumed to be generated by a white noise process to allow the frequency response of the input to be represented as a flat spectrum of magnitude σ^2. The power spectrum given in Equation (17) was also developed by Burg in maximizing the entropy associated with estimating unknown autocorrelation lags [12]. Park [13] discusses several advantages of Burg's maximum entropy method, MEM, in spectral estimation over Fourier based techniques. These advantages are revealed in its high resolution capability and absence of leakage.

Levinson-Durbin Algorithm

A method for determining the coefficients of the AR model can be obtained from the Yule-Walker equations

$$r_y(k) = - \sum_{j=1}^{N} a_j r_y(k-j) + \sigma^2 \qquad k = 0$$

$$\tag{18}$$

$$r_y(k) = - \sum_{j=1}^{N} a_j r_y(k-j) \qquad 1 \le k \le N$$

which relate the coefficients of the model to the autocorrelation of the process, $r_y(k)$. Equation (18) can be written in matrix form as

$$
\begin{bmatrix}
r_y(0) & r_y(-1) & \ldots & r_y(-N) \\
r_y(1) & r_y(0) & \ldots & r_y(-(N-1)) \\
\cdot & \cdot & \cdot & \cdot \\
\cdot & \cdot & \cdot & \cdot \\
\cdot & \cdot & \cdot & \cdot \\
r_y(N) & r_y(N-1) & \ldots & r_y(0)
\end{bmatrix}
\begin{bmatrix}
1 \\
a_1 \\
\cdot \\
\cdot \\
\cdot \\
a_N
\end{bmatrix}
=
\begin{bmatrix}
\sigma^2 \\
0 \\
\cdot \\
\cdot \\
\cdot \\
0
\end{bmatrix} . \quad (19)
$$

Estimates of the negative autocorrelation lags can be obtained from the fact that $r^*_y(m) = r_y(-m)$, $m = 0, \ldots, N$, for the stationary data case. The matrix on the far left of Equation (19) is defined as Toeplitz due to the equal-valued elements along each diagonal of this Hermitian matrix. Equation (19) containing the Toeplitz matrix can be solved using the Levinson-Durbin Algorithm [10] which provides a recursive method for determining the coefficients, $\{a_1, a_2, \ldots, a_N\}$. This algorithm is given in Table I. The Levinson-Durbin algorithm provides coefficients, $\{a_{1,1} \ \sigma^2_1\}$ $\ldots \{a_{N,1} \ldots a_{N,N} \ \sigma^2_N\}$, for all orders of the model up to N.

Linear Prediction Error Filter

The AR model in Equation (15) can also be interpreted as a linear prediction error filter, LPEF, that estimates y_T based on previous samples of the output with an associated estimation error, u_T [11]. The output from the prediction error filter can be considered as samples from a white process due to the definition of the input, u_T, in the AR model. Therefore, the filter in Figure 7 is sometimes termed

TABLE I

Levinson-Durbin Algorithm

$\sigma^2_0 = r_y(0)$

$a_{1,1} = -r_y(1)/r_y(0)$

for $i = 1, 2, \ldots, N$

$k_i = -[r_y(i) + \sum_{j=1}^{i-1} a_{i-1,j} r_y(i-j)]/\sigma^2_{i-1}$

$a_{i,i} = k_i$

$a_{i,j} = a_{i-1,j} + k_i a^*_{i-1,j-1} \qquad 1 \leq j \leq i-1$

$\sigma^2_i = (1 - |k_i|^2)\sigma^2_{i-1}$

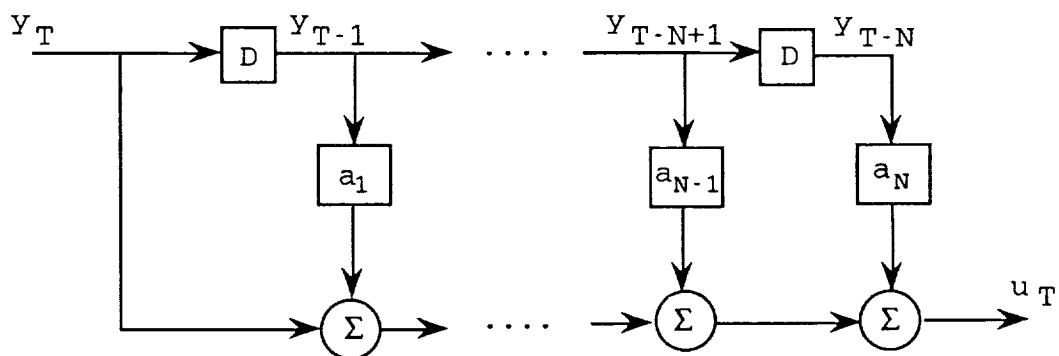where

$a_j = a_{N,j} \quad 1 \leq j \leq N$

Figure 7. Linear prediction error filter implemented as a tapped delay line.

a whitening filter. The resulting transfer function for the whitening filter

$$H_W(z) = A(z) \tag{20}$$

is just the inverse of that for the AR model in Equation (16). This whitening filter is a finite impulse response, FIR, filter which lends itself to the tap delay line implementation as seen in Figure 7.

Lattice Prediction Error Filter

The Levinson-Durbin algorithm also provides insight into another implementation of the linear prediction error filter defined in Figure 7. This new implementation involves two different errors, a forward linear prediction error, $e_{N,T}$, and a backward linear prediction error, $r_{N,T}$, where

$$e_{N,T} = \sum_{m=0}^{N} a_{N,m} y_{T-m} \tag{21}$$

$$r_{N,T} = \sum_{m=0}^{N} b_{N,m} y_{T-m} \tag{22}$$

and $a_{N,0} = b_{N,N} = 1$. The forward linear prediction error in Equation (21) is the error in predicting y_T based as N past samples, $\{y_{T-1}, y_{T-2}, \ldots, y_{T-N}\}$. The backward linear prediction error in Equation (22) is the error in predicting y_{T-N} based on N future samples, $\{y_T, y_{T-1}, \ldots, y_{T-N+1}\}$. Haykin [11] shows that for a stationary process the coefficients for the backward prediction error are the

complex conjugates of the forward prediction error coefficients,

$$b_{N,m} = a^*_{N,N-m+1} \qquad m = 1,2,\ldots,N \qquad (23)$$

in reverse order.

Based on the Levinson-Durbin algorthim, an order recursive implementation of Equations (21) and (22) can be formulated using the reflection coefficient, k_{n+1}, [11] where

$$e_{n+1,T} = e_{n,T} + k_{n+1}r_{n,T-1} \qquad (24)$$
$$r_{n+1,T} = r_{n,T-1} + k^*_{n+1}e_{n,T} \qquad (25)$$

for $n = 0,\ldots,N-1$. This order recursive implementation of a linear prediction error filter can be implemented as a lattice filter, shown in Figure 8.

The lattice prediction error filter has several properties which make it advantageous over the direct realization of a FIR filter. Haykin [11] shows that the reflection coefficients, k_{n+1}, must have magnitude less than one and that this assures minimum phase for the filter (no zeros outside the unit circle). Also, Friedlander [14] refers to several studies which favor a lattice filter over a direct realization in terms of the effects of roundoff noise due to finite word length. Another major advantage is the ability to obtain the outputs from the lattice filter for all orders up to N using only N reflection coefficients. A direct realization would require N^2-2N coefficients in order to implement the N required filter outputs.
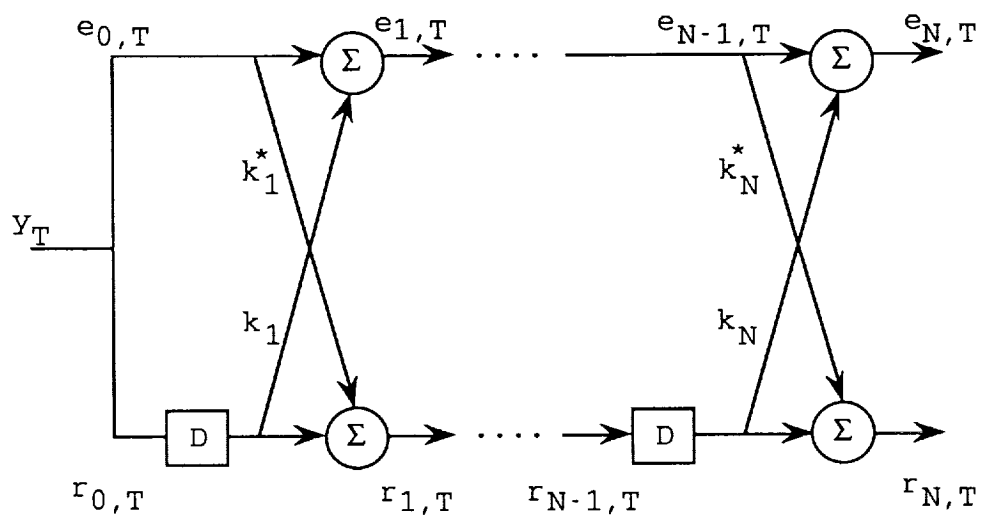
Figure 8. Linear prediction error filter implemented as a lattice structure.

Coefficient Determination

Burg's Block Implementation

The Burg algorithm [11] defines a block implementation for determining the reflection coefficients from the actual sampled data, y_T. Once the reflection coefficients have been determined, the Levinson-Durbin algorithm can be used to compute the filter coefficients. Burg's method is based on minimizing the sum of the forward and backward prediction error energies. This cost function takes the form

$$E_n = \sum_{T=n}^{M-1} |e_{n,T}|^2 + \sum_{T=n}^{M-1} |r_{n,T}|^2 \tag{26}$$

where M is the data length. This function is minimized with the constraint that the Levinson-Durbin algorithm holds. Taking the derivative of E_n with respect to k_i, $i = 1,2,\ldots,N$, and setting the result equal to zero yields [15]

$$k_i = \frac{-2 \sum_{T=i}^{M-1} r^*_{i-1,T-1} e_{i-1,T}}{\sum_{T=i}^{M-1} (|r_{i-1,T-1}|^2 + |e_{i-1,T}|^2)} \tag{27}$$

The filter coefficients, for all orders up to N, can be obtained by recursively implementing the Burg algorithm in Equation (27), the Levinson-Durbin algorithm in Table I, and the forward and backward error order updates in Equations (24) and (25). The block implementation of the Burg algorithm requires large amounts of storage space and considerable computation.

Adaptive Implementation

An adaptive approach to determining the reflection coefficients reduces the large storage requirements needed to process the data as a block of information. Two methods which have found considerable use are the gradient adaptive approach and an adaptive scheme based on least squares. Besides reducing the storage requirements, the adaptive schemes are able to track changes in a nonstationary environment.

Gradient Adaptive

A complex gradient adaptive algorithm presented by Symons [16] is based on the cost function

$$H_{n+1,T} = \sum_{i=1}^{T} [|e_{n+1,i}|^2 + |r_{n+1,i}|^2] \qquad (28)$$

where

$$e_{n+1,T} = e_{n,T} - k_{n+1,T} r_{n,T-1} \qquad (29)$$

and

$$r_{n+1,T} = r_{n,T-1} - k^*_{n+1,T} e_{n,T} . \qquad (30)$$

The gradient of the cost function with respect to $k_{n+1,T}$ yields

$$\frac{\delta H_{n+1,T}}{\delta k_{n+1,T}} = 2 \sum_{i=1}^{T} [e_{n+1,i} r^*_{n,i-1} + r^*_{n+1,i} e_{n,i}] . \qquad (31)$$

An estimate of the gradient in Equation (31) can be obtained by evaluating it at (i = T) to form an instantaneous estimate [11]. The time update of the estimated reflection coefficients, $k_{n+1,T}$, can now be written as

$$k_{n+1,T+1} = k_{n+1,T} - \mu_{n,T}[e_{n+1,T}r^*_{n,T-1} + r^*_{n+1,T}e_{n,T}] \tag{32}$$

where $\mu_{n,T}$ is the step size controlling the convergence properties of the algorithm. Griffiths [14],[17] has chosen $\mu_{n,T}$ to be inversely proportional to the prediction error power, $R_{n,T}$. Table II gives one version of the gradient adaptive implementation given by Giffiths which has been modified based on Symons results to support complex data. The associated lattice structure is equivalent to the one given in Figure 8, but with the reflection coefficient, k_{n+1}, replaced with the reflection coefficient, $-k_{n+1,T}$. Friedlander [14] provides a means for determining the AR model coefficients from the estimated reflection coefficients, shown in Table III, which is based on the transfer functions, $A_{N,T}(z)$ and $B_{N,T}(z)$, between the input x_T and the errors, $e_{N,T}$ and $r_{N,T}$, respectively, where

$$A_{N,T}(z) = 1 + a_{N,1}z^{-1} + a_{N,2}z^{-2} + \ldots + a_{N,N}z^{-N} \tag{33}$$

$$B_{N,T}(z) = 1 + b_{N,1}z^{-1} + b_{N,2}z^{-2} + \ldots + b_{N,N}z^{-N} . \tag{34}$$

This lattice structure implemenation of the transfer functions is given in Figure 9.

TABLE II

Gradient Adaptive Lattice Algorithm

Initialization:

$K_{p,-1} = 0 \quad p = 1,\ldots,N$

$r_{p,-1} = r_{p,-2} = e_{p,-1} = 0 \quad p = 0,\ldots,N$

$R_{p,-1} = \sigma$, σ is an a priori estimate of the error covariance

For each data point

$e_{0,T} = r_{0,T} = y_T$

Do for $p = 0 \ldots N-1$

$k_{p+1,T} = k_{p+1,T-1} + \beta [e_{p+1,T-1} r^*_{p-1,T-2}$

$\qquad + r^*_{p+1,T-1} e_{p,T-1}]/R_{p,T-1}$

$e_{p+1,T} = e_{p,T} - k_{p+1,T} r_{p,T-1}$

$r_{p+1,T} = r_{p,T-1} - k^*_{p+1,T} e_{p,T}$

$R_{p,T} = \alpha R_{p,T-1} + [e^2_{p,T} + r^2_{p,T-1}]$

β: controls convergence rate

α: reduces influence of past data samples

TABLE III

Algorithm for Determining the AR Model Coefficients
Based on a Gradient Adaptive Lattice Structure

Initialize: $b_{p,-1} = 0$, $p = 0,\ldots,N\text{-}1$

For $i = 0,\ldots,N$:

$a_{0,i} = b_{0,i} = [1$ for $(i = 0)$, 0 for $(i > 0)]$

For $p = 0,\ldots,N\text{-}1$:

$a_{p+1,i} = a_{p,i} - k_{p+1}b_{p,i-1}$

$b_{p+1,i} = b_{p,i-1} - k^{*}_{p+1}a_{p,i}$

$a_i = a_{N,i}$

$A_{0,T}(z)$ $A_{1,T}(z)$ $A_{N-1,T}(z)$ $A_{N,T}(z)$

INPUT

$-k_{1,T}^{*}$ $-k_{N,T}^{*}$

$-k_{1,T}$ $-k_{N,T}$

$B_{0,T}(z)$ $B_{1,T}(z)$ $B_{N-1,T}(z)$ $B_{N,T}(z)$
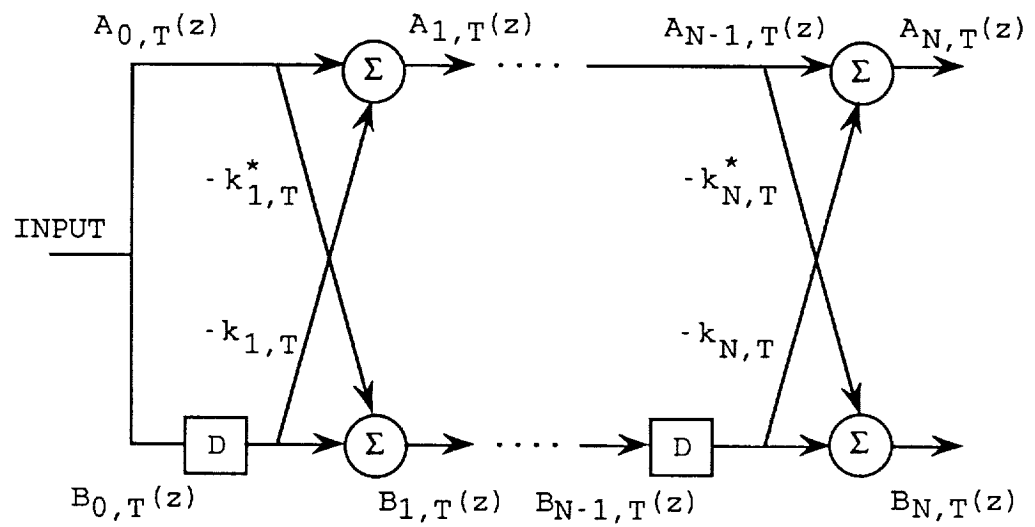
Figure 9. Transfer function implemented as a lattice structure for the gradient adaptive prediction error filter case.

Least Squares Adaptive

An exact solution for the reflection coefficient order-time update can be found using a least squares, LS, adaptive implementation. In the LS case, the sum of the squared magnitude of the forward error, up to time T,

$$\varepsilon = \sum_{t=0}^{T} |e_{N,t}|^2 \qquad (35)$$

is minimized with respect to the coefficients $\{a_{N,i}, i = 1,...,N\}$ using the principle of orthogonality. The resulting LS adaptive lattice implementation of the prediction error filter [10] is given in Table IV and the associated lattice filter in Figure 10. A derivation of this LS adaptive lattice algorithm can be found in Appendix A. The AR model coefficients can be obtained in a similiar manner to that for the gradient adaptive algorithm. Friedlander [14] provides the algorithm in Table V and the associated lattice structure in Figure 11. A derivation of this lattice structure implementation of the transfer function is given by Honig and Messerschmitt [18] for the real coefficient case. A derivation for the complex coefficient case is given in Appendix A. A major advantage of the LS adaptive implementation over gradient adaptive methods lies in the superior convergence rates of the LS implementation due to the exact solution it gives for the adaptation [14].

TABLE IV

Complex Least Squares Adaptive Lattice Algorithm

Input parameters:

N = maximum order of lattice

y_T = data sample at time T

α = exponential weighting factor

Do for $T = 0$ to T_{max}

$e_{0,T} = r_{0,T} = x_T$

$R^e_{0,T} = R^r_{0,T} = \alpha R^e_{0,T-1} + y_T y^*_T$

$\gamma_{0,T} = 1$

Do for $n = 0$ to $\{min(N,T)-1\}$

$k_{n+1,T} = \alpha k_{n+1,T-1} + e^*_{n,T} r_{n,T-1}/\gamma_{n,T-1}$

$\gamma_{n+1,T} = \gamma_{n,T} - r^*_{n,T} R^{-r}_{n,T} r_{n,T}$

$k^r_{n+1,T} = k_{n+1,T} R^{-r}_{n,T-1}$

$e_{n+1,T} = e_{n,T} - k^{*r}_{n+1,T} r_{n,T-1}$

$R^e_{n+1,T} = R^e_{n,T} - k^r_{n+1,T} k^*_{n+1,T}$

$k^e_{n+1,T} = R^{-e}_{n,T} k_{n+1,T}$

$r_{n+1,T} = r_{n,T-1} - k^e_{n+1,T} e_{n,T}$

$R^r_{n+1,T} = R^r_{n,T-1} - k^*_{n+1,T} k^e_{n+1,T}$

Note: Division by zero where $y = \gamma$, R^r, R^e, set $1/y = 0$.
    Initialize the variables k, r, R^e, R^r, and γ to zero.

Figure 10. Least squares adaptive lattice prediction error filter.

TABLE V

Algorithm for Determining the AR Model Coefficeints
Based on a Complex LS Adaptive Lattice Structure

For $i = 0, \ldots, N$ do the following

$b_{p,-1,T} = 0$ for $p = 0, \ldots, N-1$

$a_{0,0,T} = b_{0,0,T} = 1$ for $i = 0$

$c_{0,0,T} = 0$ for $i = 0$

$a_{0,i,T} = b_{0,i,T} = c_{0,i,T} = 0$ for $i > 0$

For $p = 0, \ldots, N-1$

$b_{p,i,T-1} = b_{p,i,T} + c_{p,i,T} r_{p,T} / \gamma_{p,T}$

$c_{p+1,i,T} = c_{p,i,T} + b_{p,i,T} R^{-r}_{p,T} r^{*}_{p,T}$

$a_{p+1,i,T} = a_{p,i,T} - b_{p,i-1,T-1} R^{-r}_{p,T-1} k^{*}_{p+1,T}$

$b_{p+1,i,T} = b_{p,i-1,T-1} - a_{p,i,T} R^{-e}_{p,T} k_{p+1,T}$

(a) The overall structure.

(b) A single section.

Figure 11. Transfer function implemented as a lattice structure for the least squares adaptive prediction error filter case.

Model Order

In the AR modeling process the appropriate model order N is usually not known *a priori*. The use of too low a model order results in a smoothed spectral estimate and too high a model order induces spurious detail into the spectral estimate. A method for determining the correct model order based on some error criterion can be devised. The coefficient estimation techniques presented previously have monotonically decreasing error powers which prevent the use of the error power as the sole determining factor of the correct model order. Akaike [19], [20] has developed two criteria for determining model order selection. The first criterion is based on minimizing the average error, E_N, for a one step prediction and is termed a final prediction error, FPE, criterion. The FPE criterion takes the form

$$FPE_N = E_N \left[\frac{M+N+1}{M-N-1} \right] \tag{36}$$

where M is the number of data samples used. The model order, N, is choosen so as to minimize FPE. This method has been found to predict too low a model order in some cases. Akaike has developed a second criterion which is based on minimizing an information theoretic function assuming the process has Gaussian statistics. The Akaike information criterion, AIC, takes the form

$$AIC_N = \ln(E_N) + 2(N+1)/M \tag{37}$$

where the model order, N, is choosen to minimize the AIC.

CHAPTER III

THE EFFECTS OF CLUTTER IN

ESTIMATING WINDSPEED

NASA Model

To support the development of an airborne pulsed Doppler radar system for the detection of microbursts in the near terminal area, NASA [2] has developed a simulation model for generating pulsed Doppler weather radar data containing microburst and clutter returns. The model is designed to allow for the input of clutter and microburst information as well as radar system parameters. Appendix B gives a listing of the possible input parameters to the model.

To study pulse-pair estimates of radial wind velocity, two data sets were generated using the simulation model, one set contained a wet microburst and one set contained a dry microburst with the microburst centered 5km from touchdown. Appendix C contains Fourier spectral estimates of the simulated dry microburst and clutter return. Each data set included clutter based on actual clutter collected in the vicinity of the Denver Stapleton airport. In each case the data represented a stationary situation with the the aircraft positioned 7km from touchdown on a 3 degree glide slope with the first range bin recorded 1km from the aircraft. According to the simulated radar pulse width, successive range bins were located 150m from each other. Radar returns

were collected over 40 range bins from 512 pulses transmitted
by the radar at a pulse repetition frequency of 3723.0 Hz.
Other parameters related to the model for both the dry and
wet microburst can be found in Appendix B.

Bias in Pulse-Pair Mean Estimates
Due to Clutter

Figure 12 shows the resulting pulse-pair estimates of
average windspeed for each range bin in the case of a radar
return containing a wet microburst plus clutter. Equation
(1) was used to convert the pulse-pair mean frequencies to
the corresponding Doppler velocities.   This figure
illustrates the characteristic "S" curve associated with
microburst. Estimates of average windspeed go from positive
to negative as one moves through the microburst with zero
radial velocity near the center of the microburst, range cell
27.   In the case of the dry microburst in Figure 13, the
familiar "S" curve is no longer distinguishable.   Two
factors, bias due to clutter [21] and low signal-to-noise
ratios, SNR, contribute to these poor estimates of windspeed
within the dry microburst by the pulse-pair estimator. The
effect of the bias due to clutter is less evident in the case
of a wet microburst due to the expected higher
signal-to-clutter ratios, SCR's. Due to the overwhelming
effect of clutter and low SNR's on the pulse-pair estimates
of windspeed, the dry microburst will be choosen as the test
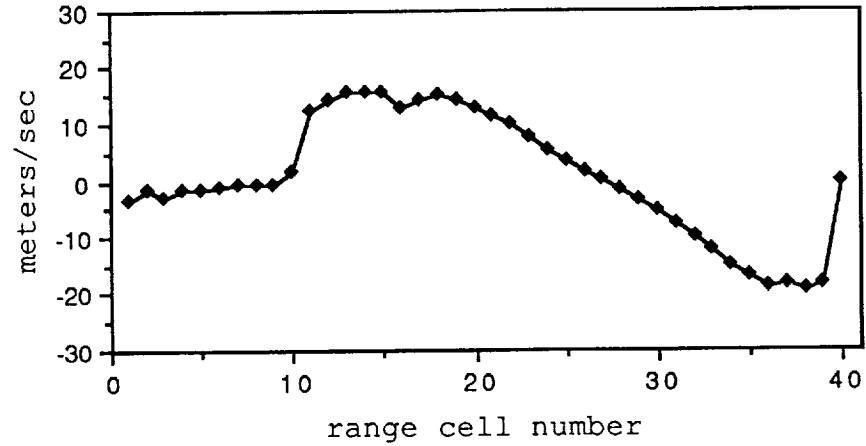
Figure 12. Pulse-pair mean estimates of the return from a
wet microburst and clutter.
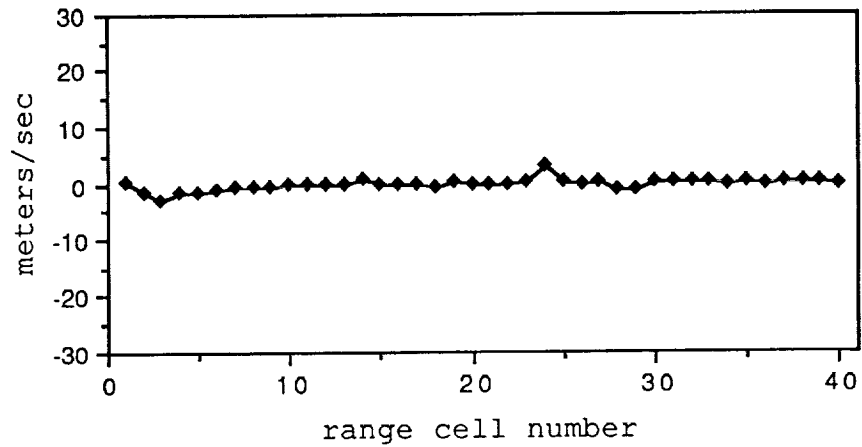
Figure 13. Pulse-pair mean estimates of the return from a
dry microburst and clutter.

case where any findings should also apply for the wet microburst case with higher SNR's and SCR's expected in a majority of the range cells.

Analysis of a Dry Microburst

A clutter rejection filter has been proposed as a means for removing the bias in the pulse-pair estimates. Before attempting to define this clutter rejection filter, a study of the pulse-pair estimates of a dry microburst without clutter is essential for interpreting the results after filtering. In the dry microburst case, the windspeeds versus distance from the of the center microburst are still characterized by the familiar "S" curve. Pulse-pair estimates in the presence of the dry microburst without clutter should therefore reflect this physical phenomena.

The model is now used to generate the same dry microburst but without clutter. The pulse-pair mean estimates for this set of data are shown in Figure 14. Range cells 23 through 32 in Figure 14 are indicative of the "S" curve associated with the microburst. A spectral analysis, using a 512 point DFT, of range cells 25, 27, and 29, shown in Figure 15, reveals that these range cells do indeed contain microburst information with SNR's on the order of 20 dB. As a note of reference, all Fourier spectral analysis presented in this thesis will be based on 512 data samples with no zero padding and will be normalized by the number of data points.
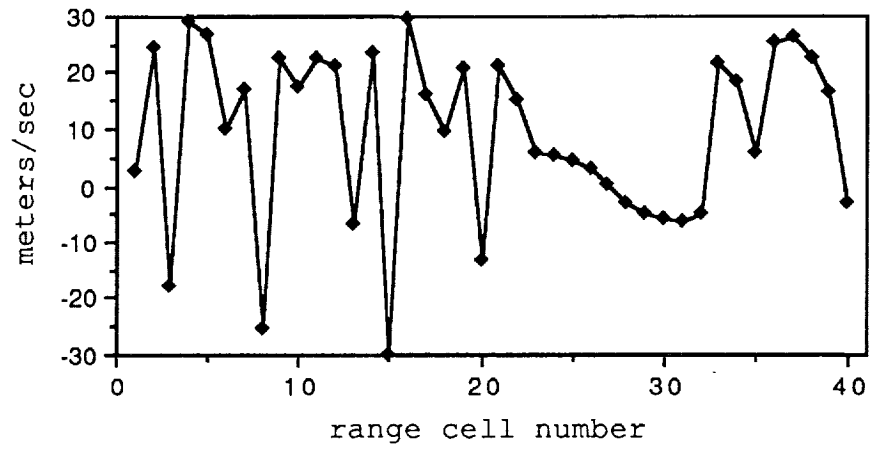
Figure 14. Pulse-pair mean estimates of the return from a dry microburst.
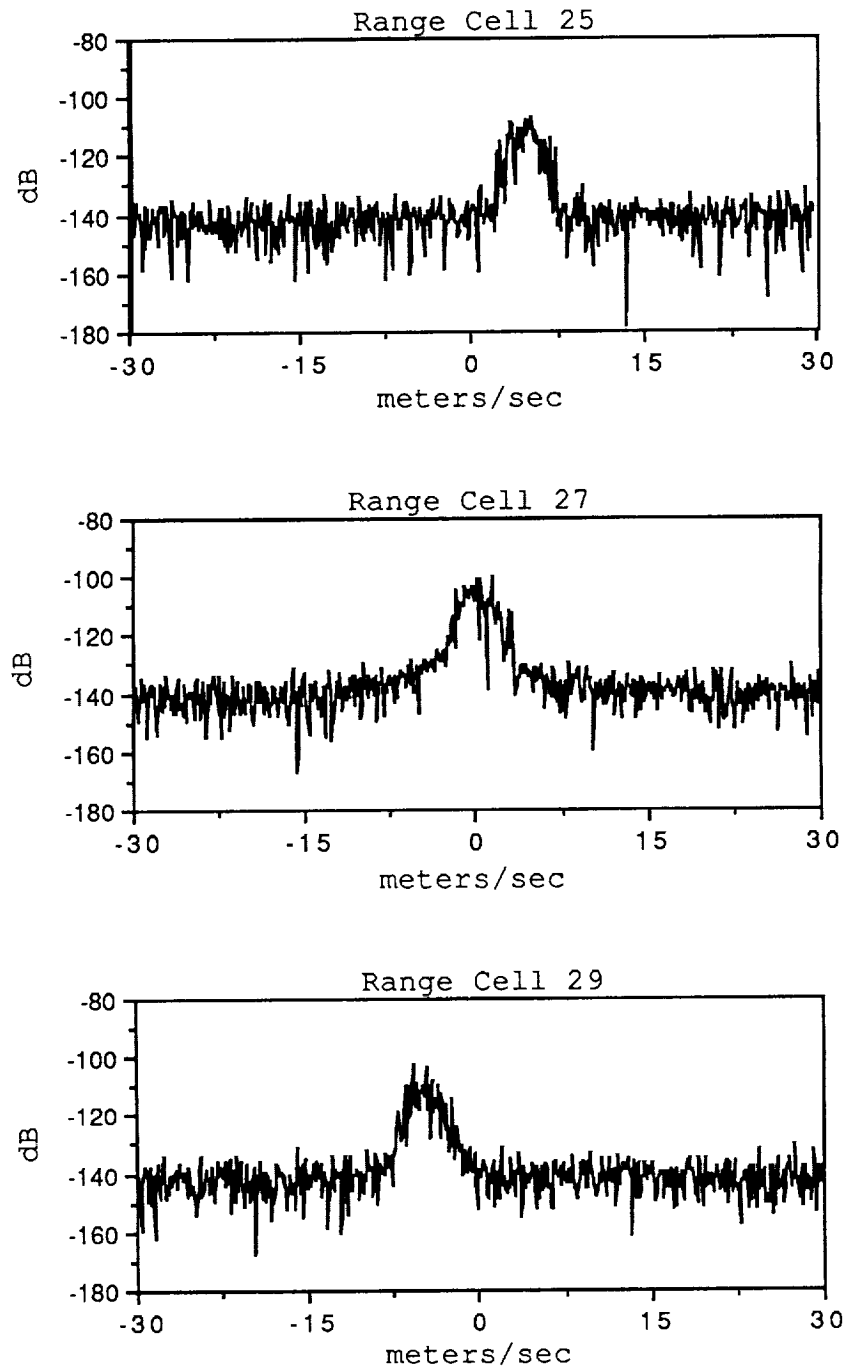
Figure 15. Fourier spectral analysis of range cells 25, 27, and 29 containing a dry microburst.

In Figure 14, range cells outside of 23 through 32 have what appear to be random estimates of mean windspeed. Figure 16 provides a spectrum of range cell 15 and is typical of the spectral content in these range cells where the SNR's are very low. This low SNR can be used to explain the random mean estimates of windspeed found in these range cells [6]. Spectral estimates for all 40 range cells are given in Appendix D for the dry microburst without clutter case.

Validation of Mean Estimates

Width Estimates

A method for determining valid pulse-pair mean estimates may be found by examining pulse-pair width estimates and power levels. Large widths estimates may indicate the presents of a bi-modal distribution or low SNR and serve as an indicator of questionable estimates on a range cell by range cell evaluation. This concept is supported by the width estimates of the dry microburst data without clutter given in Figure 17. The large width estimates (approximately 13 meters/sec) in the range cells away from the center of the microburst (range cell 27) are indicative of the low SNR expected in the dry microburst environment.

Power Levels

Power levels may also provide a level of significance that can be associated with the pulse-pair mean estimates of windspeed. Figure 18 gives the power levels associated with the dry microburst data without clutter. The power levels
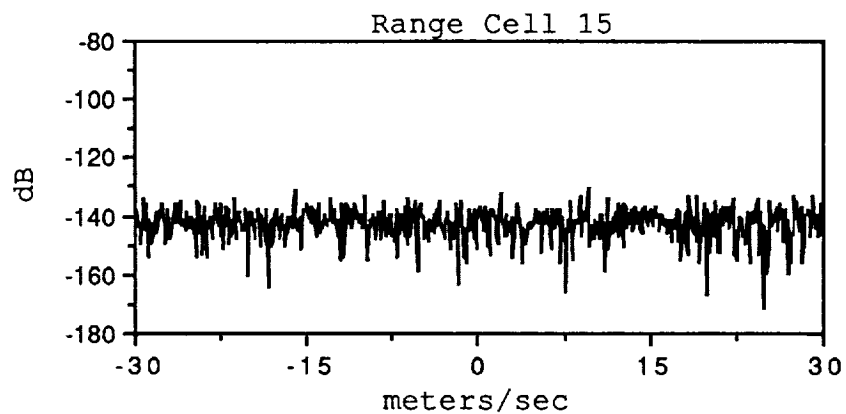
Figure 16. Fourier spectral estimate of range cell 15 with a low SNR.
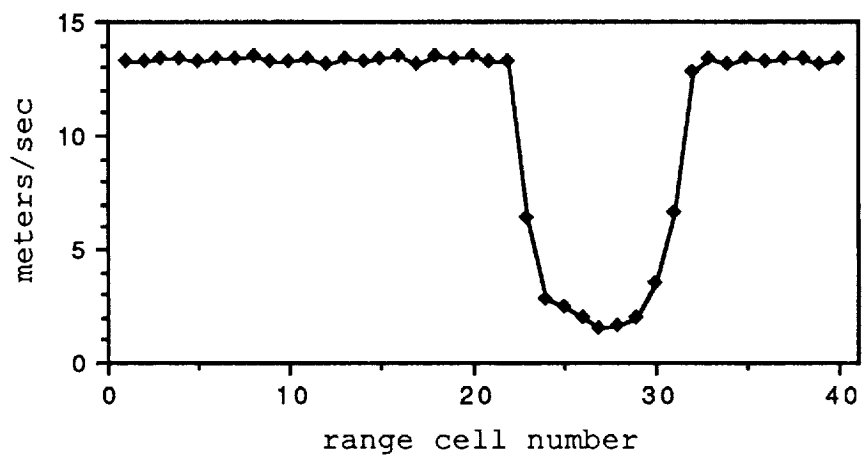
Figure 17. Pulse-pair width estimates of the return from a dry microburst.
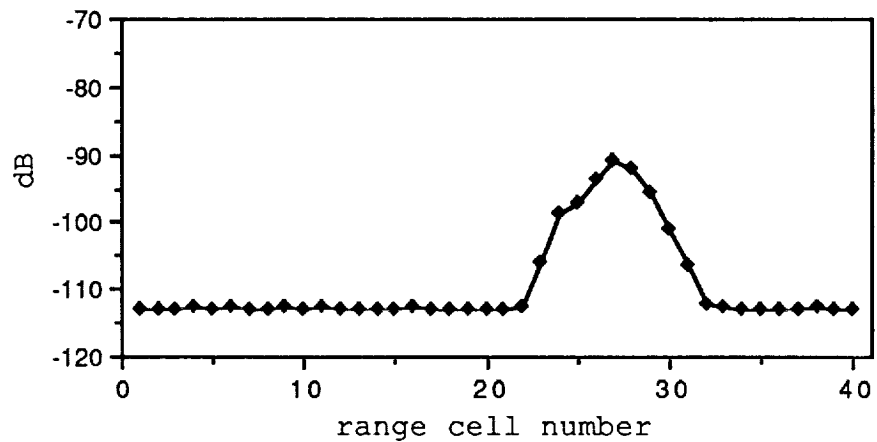
Figure 18. Power levels associated with the return from a dry microburst.

were computed as a sum of the squared magnitudes of the IQ radar return samples. The resulting power levels in this thesis are therefore normalized by the sampling period. The range cells near the center of the microburst (24-30) have approximately a 10dB to 20dB relative gain in power compared to range cells away from the center of the microburst. This gain can be associated with the higher target concentrations near the center of the dry microburst. The low levels of power indicate the presence of noise only.

Threshold Levels

The analysis given in the previous two sections suggests that the power levels and the pulse pair width estimates may be useful in forming a statistic to identify the levels of significance to associate with the pulse-pair mean estimates. The threshold power levels can be obtained based on statistics of noise and clutter power levels. After filtering, the power in the return data can be contributed two sources: noise and weather information. Thresholds for width estimates may be defined by statistical analysis of radar returns in windshear situations. The actual statistic will not be formulated in this thesis, but the power levels and pulse-pair width estimates will be used as guides for evaluating the significance of pulse-pair mean estimates.

Clutter Analysis

At this point, a study of the clutter may reveal possible filtering techniques for removing the bias imposed by the clutter on the pulse-pair estimates of windspeed. The radar simulation model can be used to generate range bins containing clutter only. Pulse-pair estimates of mean clutter speed, where "clutter speed" refers to the Doppler spectrum associated with the clutter, are given in Figure 19. The clutter tends to be centered around zero Doppler due to stationary objects along the flight path, but a slight shift in speed to negative Doppler occurs in the first few range cells. This shift can be contributed to returns from sidelobes which contain information from objects at close range which have a different relative velocity with respect to the aircraft than objects along the intended flight path. The demodulation of the return signal to Doppler frequencies is based on the relative ground velocity of the aircraft along the intended flight path.

Figure 20, containing range cells 6, 20, and 35, is typical of the spectral estimates of the clutter for this set of 40 range cells. Appendix E contains Fourier spectral estimates of the clutter for all 40 range cells. This particular set of clutter return data does not contain any specular clutter away from zero Doppler which may result from traffic on a nearby highway, but this scenario should not be ruled out. Even though the clutter tends to be centered around zero Doppler, the actual width and power associated
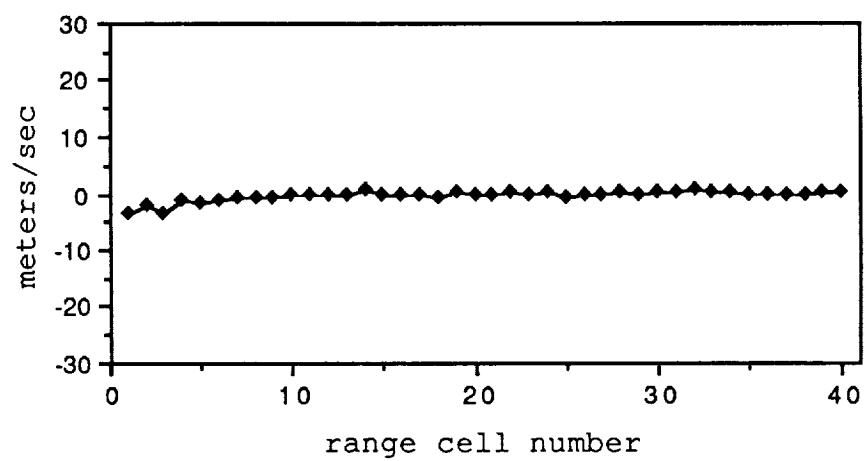
Figure 19. Pulse-pair mean estimates of the return from clutter.
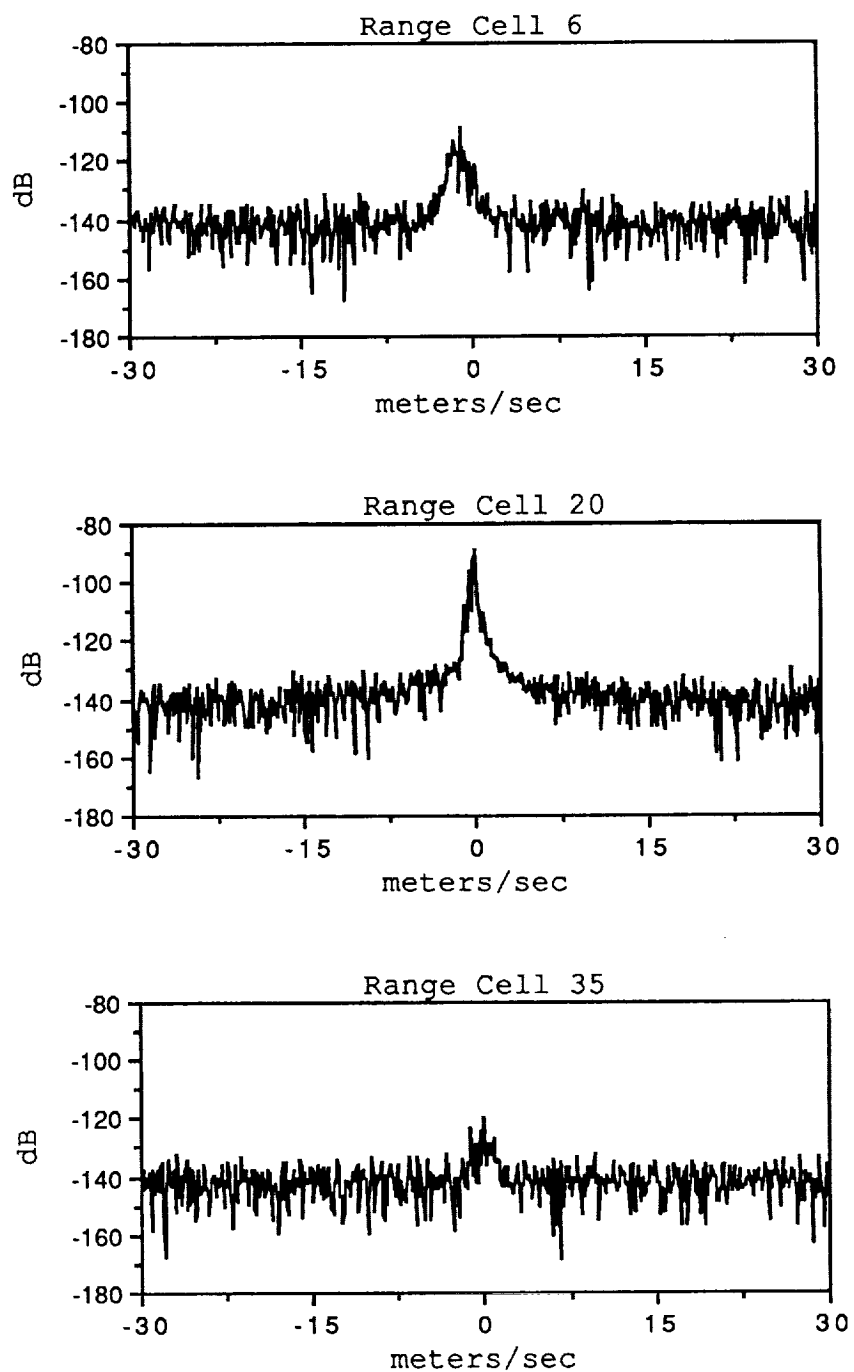
Figure 20. Fourier spectral estimates of range cells 6, 20, and 35 containing clutter.

with the clutter varies from one range cell to the next. This variation can be seen in Figures 21 and 22 which represent the power and width estimates, respectively, associated with each range cell. These width estimates were obtained using the pulse-pair algorithm. The large width estimates in some of the range cells may be the result of low power levels within the these range cells which effect the performance of the pulse-pair estimator [6]. The actual clutter will also vary from airport to airport and even from runway to runway due to the varied physical environments. This imposes a problem in designing an optimum filter to remove the clutter from the radar return data.
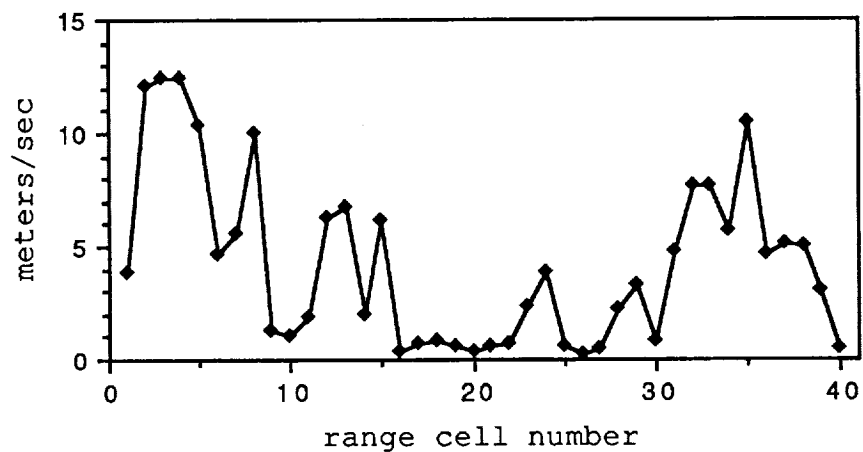
Figure 21. Pulse-pair width estimates of the return from clutter.
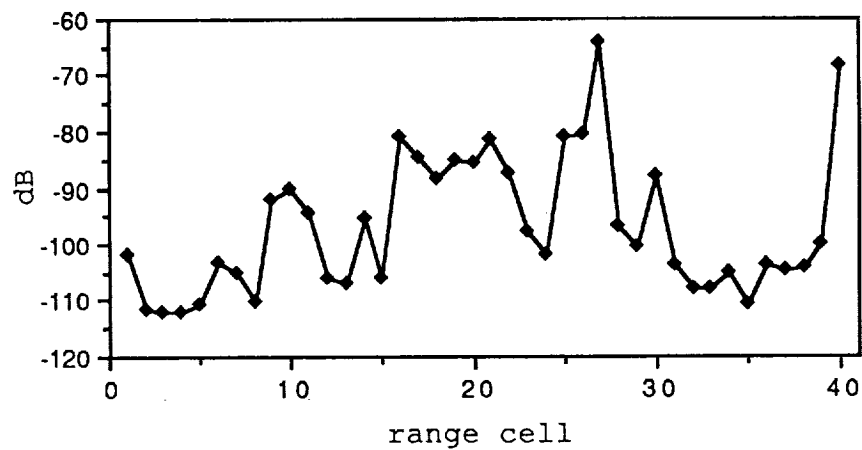
Figure 22. Power levels associated with the return from clutter.

CHAPTER IV

CLUTTER REJECTION FILTERS

The Optimum Clutter Rejection Filter

Based on observations of the variation in the simulation model clutter spectra over many range cells it appears that the optimum filtering scheme for removing the clutter from the return data in a particular range cell would need to be based on the geographical location of the range cell. Even for a given runway, periodic updates of the filters used on final approach would need to be obtained due to glideslope flight path variations and also changes in the physical environment of the airport terminal area. This scenario suggests some type of adaptive modeling process to define the clutter in each range cell with updating as warranted.

Adaptive modeling can be accomplished using the AR model defined in Chapter II implemented as an adaptive LS lattice structure in order to determine the model parameters. The lattice structure was chosen for its ability to provide coefficients of the model recursively for all orders up to N. This provides the ability to use different model orders for each range cell based on the requirements mandated by the clutter. The adaptive LS lattice structure implementation for determining the model coefficients is choosen for its superior convergence rates over gradient adaptive schemes. The lattice structure also insures that the resulting filter

will be stable. The model parameters could be obtained on approach to a runway on days when favorable weather conditions exist. In the presence of a microburst or other source of windshear, the best possible filters could then be available to remove unwanted ground clutter from the return data, enhancing the ability to detect windshear.

The Complex Square Root Normalized Recursive Least Squares Lattice Estimation Algorithm

An alternative form of the adaptive LS lattice structure given in Chapter II can be obtained, involving fewer update equations and potential for fixed point implementation. This alternative implementation is termed a normalized recursive LS lattice structure. A complex form of the algorithm, needed to process the I and Q data, was not available in the literature. A modification of the normalized recursive LS lattice algorithm for real data given by Lee [22] has been developed to handle complex data. The derivation is given in Appendix A. Table VI gives the necessary equations needed to implement the complex square root normalized recursive least squares lattice estimation algorithm given in Figure 23.

The complex square root normalized recursive least squares lattice estimation algorithm requires only 3 equations per order update compared to six in the unnormalized version in Table IV. The normalizations also restrict the magnitude of the normalized reflection coefficients, Γ, forward errors, v, and backward errors, η to

TABLE VI

Complex Square Root Normalized Recursive Least
Squares Lattice Estimation Algorithm

Initialize:

$R_{-1} = \sigma$ σ is a small positive value

for $T = 0, T_{max}$

$R_T = \alpha R_{T-1} + y^{*}_T y_T$

$v_{0,T} = \eta_{0,T} = y_T (R_T)^{-1/2}$

for $n = 0$ to $[\min\{T,N\} - 1]$

$\Gamma_{n+1,T} = [1 - v^{*}_{n,T} v_{n,T}]^{1/2} \Gamma_{n+1,T-1}$

$\qquad [1 - \eta^{*}_{n,T-1} \eta_{n,T-1}]^{1/2} + v^{*}_{n,T} \eta_{n,T-1}$

$v_{n+1,T} = [1 - \Gamma^{*}_{n+1,T} \Gamma_{n+1,T}]^{-1/2} [v_{n,T} - \Gamma^{*}_{n+1,T} \eta_{n,T-1}]$

$\qquad [1 - \eta^{*}_{n,T-1} \eta_{n,T-1}]^{-1/2}$

$\eta_{n+1,T} = [1 - \Gamma^{*}_{n+1,T} \Gamma_{n+1,T}]^{-1/2} [\eta_{n,T-1} - \Gamma_{n+1,T} v_{n,T}]$

$\qquad [1 - v^{*}_{n,T} v_{n,T}]^{-1/2}$

Note: Division by zero where $y = 1/x : x = 0$ should result in
$y = 0$. Initialize the variables Γ, v, and η to zero.

$$x^c = [1-x^*x]^{-1/2}$$

Figure 23. Complex square root normalized least squares adaptive lattice prediction error filter.

values less than one. This conditioning of the variables allows for fixed implementation.

The transfer function for the normalized recursive least squares lattice estimation algorithm in Figure 24 can be written as

$$\underline{A}_{N,T}(z) = \underline{a}_{N,0} + \underline{a}_{N,1}z^{-1} + \underline{a}_{N,2}z^{-2} + \ldots + \underline{a}_{N,N}z^{-N} \quad (38)$$

$$\underline{B}_{N,T}(z) = \underline{b}_{N,0} + \underline{b}_{N,1}z^{-1} + \underline{b}_{N,2}z^{-2} + \ldots + \underline{b}_{N,N}z^{-N} \quad (39)$$

$$\underline{C}_{N,T}(z) = \underline{c}_{N,0} + \underline{c}_{N,1}z^{-1} + \underline{c}_{N,2}z^{-2} + \ldots + \underline{c}_{N,N}z^{-N} \,. \quad (40)$$

The normalized transfer functions $\underline{A}_{N,T}(z)$ and $\underline{B}_{N,T}(z)$ correspond to the transfer functions between the normalized input, $y_T R_T^{-1/2}$, and the normalized forward, $v_{N,T}$, and backward, $\eta_{N,T}$, errors, respectively. The normalized transfer function $\underline{C}_{N,T}(z)$ corresponds to an auxillary variable defined in Appendix A and is only needed for the implementation of the normalized transfer functions $\underline{A}_{N,T}(z)$ and $\underline{B}_{N,T}(z)$ as a lattice structure.

The coefficients for the transfer function of the AR model defined in Equation (15) in Chapter II, and equally so, those for the transfer function of the whitening filter defined in Equation (20) of Chapter II, can be obtained from the normalized transfer function given in Equation (38) as

$$\begin{aligned} A_{N,T}(z) &= (\underline{a}_{N,0}/\underline{a}_{N,0}) + (\underline{a}_{N,1}/\underline{a}_{N,0})z^{-1} + (\underline{a}_{N,2}/\underline{a}_{N,0})z^{-2} \\ &\quad + \ldots + (\underline{a}_{N,N}/\underline{a}_{N,0})z^{-N} \\ &= 1 + a_{N,1}z^{-1} + a_{N,2}z^{-2} + \ldots + a_{N,N}z^{-N} \,. \quad (41) \end{aligned}$$

An algorithm for obtaining the normalized coefficients is

(a) The overall structure.

$$x^c = [1-x^*x]^{-1/2}$$
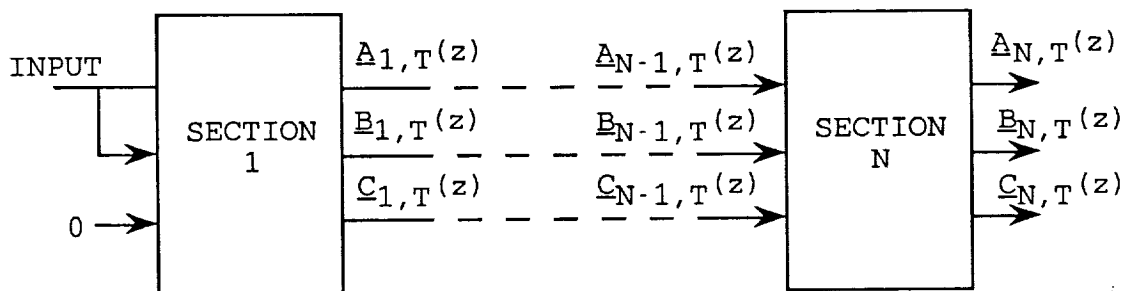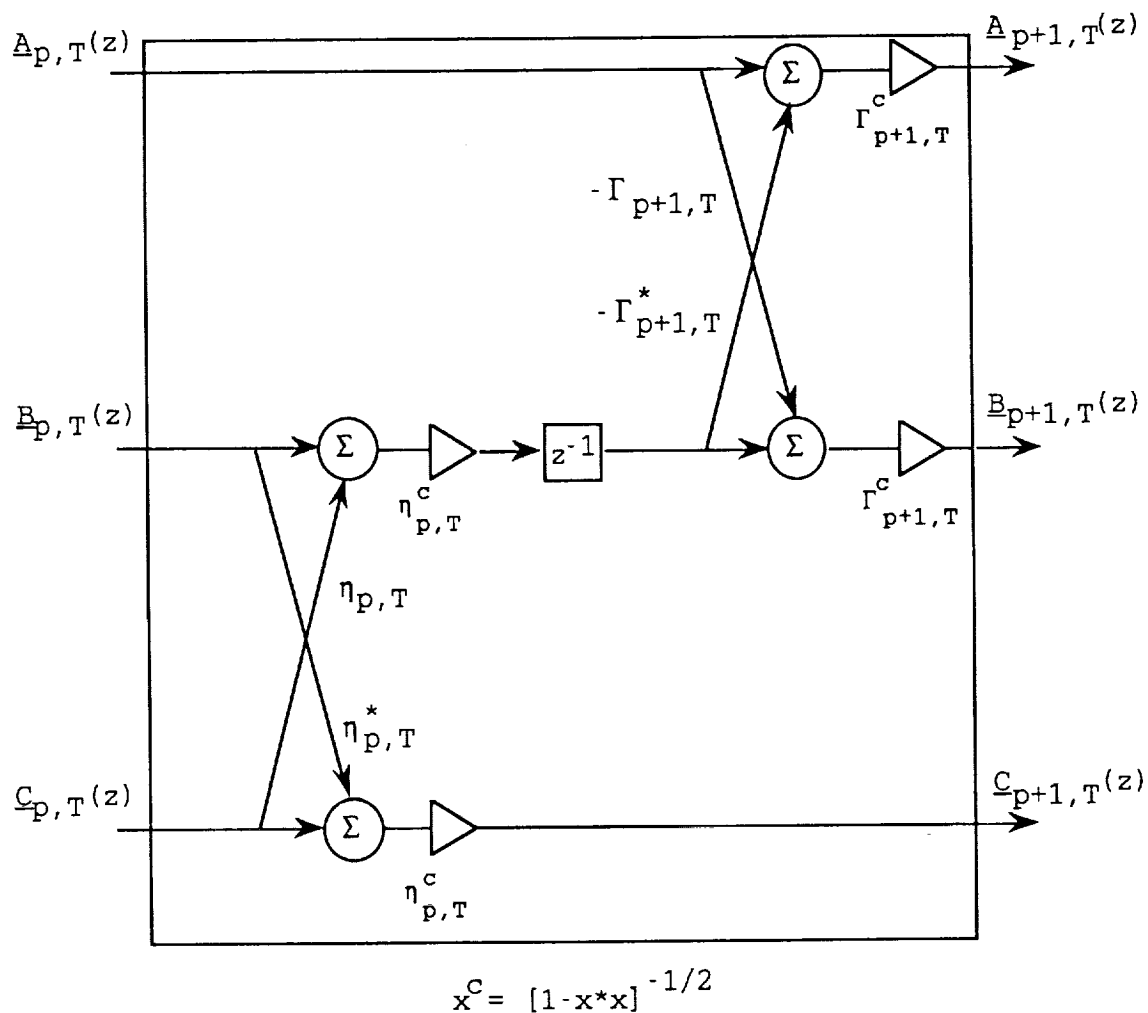
(b) A single section.

Figure 24. Transfer function implemented as a lattice structure for the complex square root normalized least squares adaptive prediction error filter case.

given in Table VII. This algorithm is given by Honig [18] and Friedlander [14] for the real data case. A derivation for the complex case is given in Appendix A.

10th Order AR Clutter Model

Spectral estimates of the range cell clutter data using the power spectrum of the AR process in Equation (17) can now be compared to Fourier estimates to evaluate the ability of the AR coefficients to model the clutter. Based on preliminary evaluations a model order of 10 was chosen for the AR process in modeling the clutter. This fixed model order simplifies the modeling process with the constraint that the model order is sufficient in a majority of the range cells. Future evaluations based on Aikaike's criterion in Chapter I or other model order determination techniques may be used if the exact model order is vital for each range cell.

Figure 25 contains a Fourier spectral estimate, based on a 512 point DFT, of the clutter contained in range cell 6. The ability to model the clutter with a 10th order AR model is evident by comparing the model given in Figure 26 with the corresponding Fourier spectral estimate. Note the ability to model the clutter in Figure 26 even when the mode of the clutter is shifted from zero Doppler. This ability to model the clutter as a low order AR process satisfies the necessary

TABLE VII

Algorithm for Determining the AR Model Coefficients Based
on a Normalized Complex LS Adaptive Lattice Structure

$R_T = \alpha R_{T-1} + x^*_T x_T$

For i = 0,...,N do the following

$b_{p,-1,T} = 0$ for p = 0,...,N-1

$a_{0,0,T} = b_{0,0,T} = R_T^{-1/2}$ for i = 0

$c_{0,0,T} = 0$ for i = 0

$a_{0,i,T} = b_{0,i,T} = c_{0,i,T} = 0$ for i > 0

For p = 0,...,N-1

$b_{p,i,T-1} = [b_{p,i,T} + c_{p,i,T}\eta_{p,T}]$
$\qquad [1-\eta^*_{p,T}\eta_{p,T}]^{-1/2}$

$c_{p+1,i,T} = [c_{p,i,T} + b_{p,i,T}\eta^*_{p,T}][1-\eta^*_{p,T}\eta_{p,T}]^{-1/2}$

$a_{p+1,i,T} = [a_{p,i,T} - b_{p,i-1,T-1}\Gamma^*_{p+1,T}]$
$\qquad [1-\Gamma^*_{p+1,T}\Gamma_{p+1,T}]^{-1/2}$

$b_{p+1,i,T} = [b_{p,i-1,T-1} - a_{p,i,T}\Gamma_{p+1,T}]$
$\qquad [1-\Gamma^*_{p+1,T}\Gamma_{p+1,T}]^{-1/2}$

where

$a_{p,i} = a_{p,i}/a_{p,0}$

Figure 25. Fourier spectral estimate of the clutter in range cell 6.
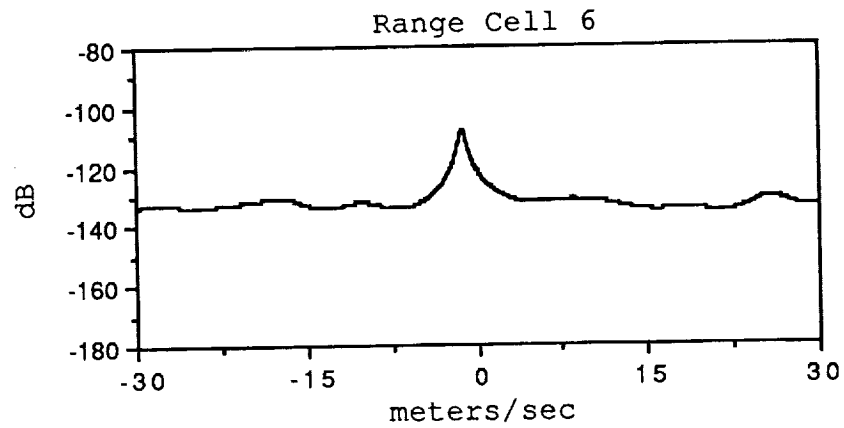
Figure 26. AR spectral estimate of the clutter in range cell 6.

limitations on storage requirements in a real world
implementation, in that only a limited number of coefficients
need be stored and completely specify the model.

10th Order Complex Coefficient FIR Filters

The coefficients of the AR model can now be used to
filter the microburst plus clutter data. The whitening
filter defined in Equation (20) of Chapter II gives the
relationship between the model parameters and the filter
coefficients and can be used as a clutter rejection filter.
The discrete time filter takes the form

$$x_T = y_T + a_{N,1}y_{T-1} + \ldots + a_{N,N}y_{T-N} \tag{42}$$

where y_T is the radar return containing microburst plus
clutter data and x_T is the result of the filtering process.
This filter is a finite impulse respone, FIR, filter which
can be implemented as a tapped delay line as seen in Figure
27. Another advantage of this type of filter is the complex
coefficients obtained from the modeling process, which define
the filter unit sample response as complex, provide the
ability to define filters with nonsymmetric magnitude
frequency responses. This is necessary when the clutter is
shifted away from zero Doppler or in the case of specular
clutter which may be due to moving objects on the ground.
The phase associated with this type of complex coefficient
FIR filter is not be constrained to linear. A linear phase,
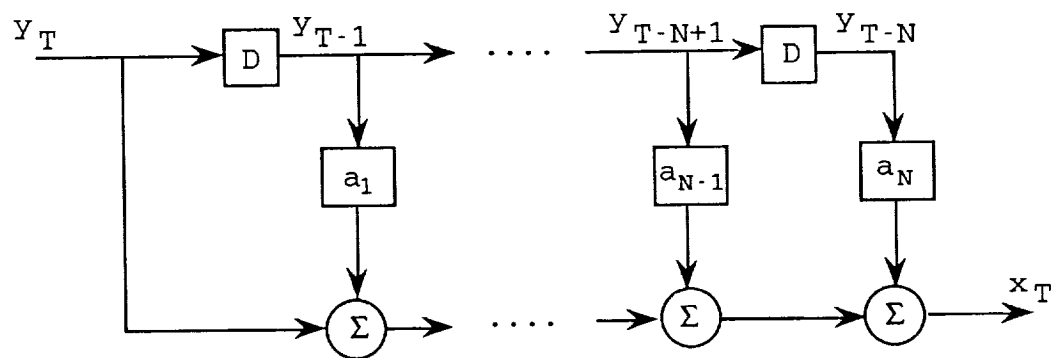
Figure 27. FIR clutter rejection filter implemented as a tapped delay line.

however, is not necessary for this filter if the pulse-pair algorithm is used to estimate windspeed mean and width in each range cell [21].

Analysis of Filtering Schemes

Filters Based on the Clutter
in Each Range Cell

Using the filter defined in Equation (42), an analysis will be made of the effects of filtering each range cell with a 10th order complex coefficient FIR filter where the coefficients are determined from the clutter using the complex square root normalized adaptive least squares lattice estimation algorithm. This analysis will be based on simulated radar returns from a dry microburst plus clutter data where the effect of bias on the pulse-pair mean estimates of windspeed is significant. Any resulting generalizations from this analysis can be applied in the wet microburst case where the effect of bias is reduced due to higher SNR's and SCR's. The magnitude and phase response of the filters defined for each range cell are given in Appendix F and G, respectively. The spectral content of the filtered range cells is given in Appendix H. Figure 28 shows the pulse-pair estimates of the post filtered data containing a dry microburst plus clutter. The characteristic "S" curve is now evident in range cells 23 through 32. The ability to remove the clutter without further biasing the pulse-pair estimates of the dry microburst is evident in Figure 29 by comparing the post filtered estimates of windspeed to those
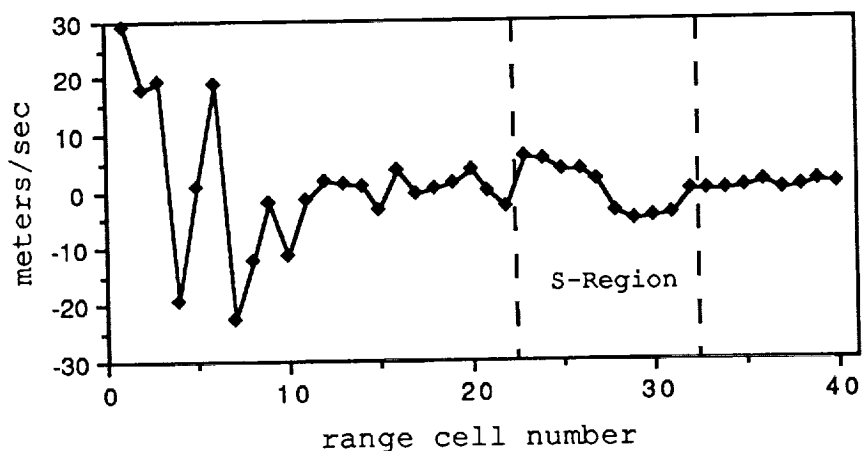
Figure 28. Pulse-pair mean estimates of filtered dry microburst plus clutter data where the appropriate filter based on the clutter in each range cell has been applied.
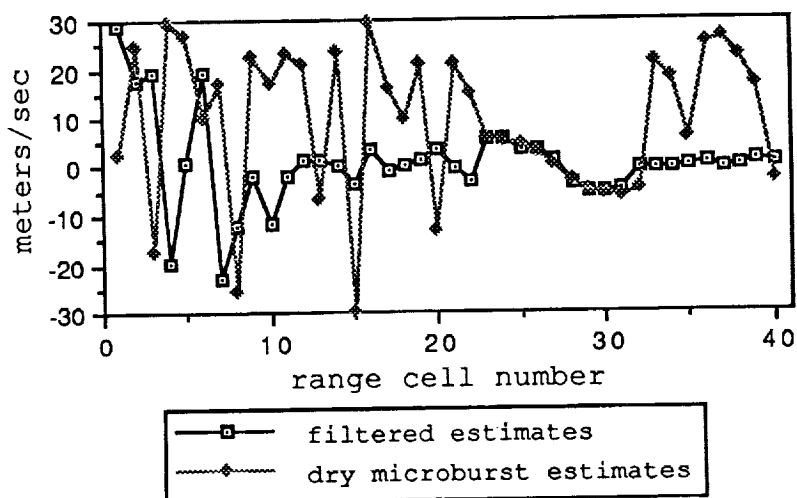
Figure 29. Pulse-pair mean estimates of filtered dry microburst plus clutter data where the appropriate filter based on the clutter in each range cell has been applied compared to estimates given in the case of a dry microburst without clutter.

from the data containing a dry microburst only. The fluctuating estimates of windspeed outside of range cells 23 through 32 in Figure 28 may be attributed to instabilities in the pulse-pair estimator when the resulting filtered data contains a very low SNR. A low SNR after filtering is illustrated in Figure 30 with the filtered spectrum of range cell 7.

The pulse-pair mean estimates after filtering will now be evaluated using pulse-pair width estimates and power levels. Using the pulse-pair width estimates of the dry microburst without clutter, shown in Figure 17, as a basis for setting thresholds on valid mean estimates, assume that a width estimate threshold of 7 m/sec is set. This choice of threshold is not based on a statistical evaluation but is used only for relative comparisons. Pulse-pair width estimates from filtered dry microburst plus clutter data, illustrated in Figure 31, reveal that range cells 23-26 and 28-31, which contain valid mean estimates, have width estimates below this threshold. This correlates with the previous estimates of returns from the dry microburst without clutter. With this criterian, the mean estimate at the center of the microburst (range cell 27) would be considered questionable. A large width estimate of approximately 11m/sec is likely since the clutter and microburst information would have the highest probability of occupying the same frequency ranges near zero Doppler, and would both
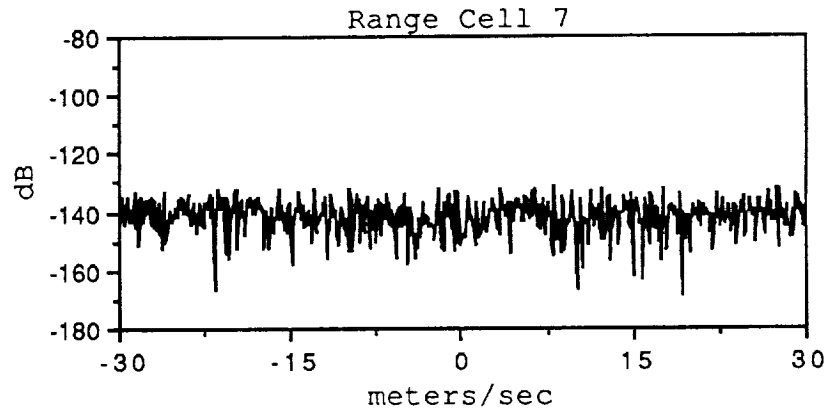
Figure 30. Filtered spectrum of range cell 7.
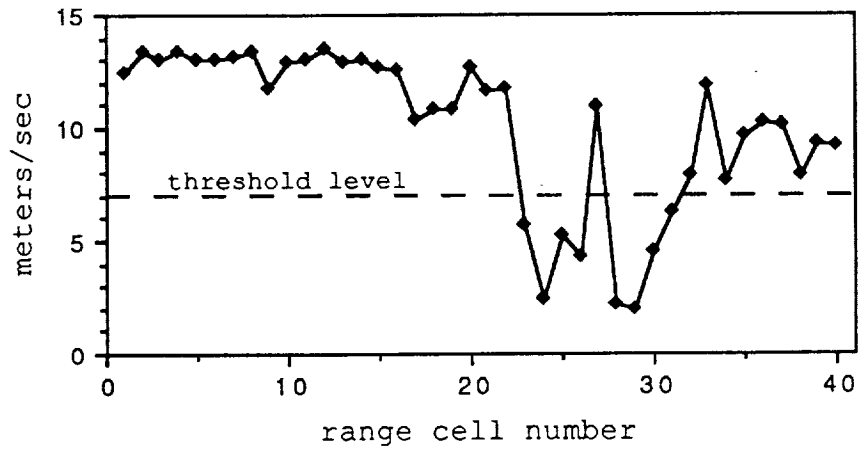
Figure 31. Pulse-pair width estimates after filtering using the filter coefficients obtained from the clutter in each range cell.

be extracted in the filtering process resulting in a very low signal to noise ratio.

A minimum threshold for power level estimates might also be defined using the dry microburst without clutter estimates in Figure 18. For comparison, a -105 dB threshold will be set. Based on this threshold, the power levels in Figure 32 define range cells 23-31 and range cell 40 as having adequate return power levels to provide valid mean estimates. The power levels for range cells 27 and 40 do not correlate with the information provided by the width estimate analysis in labeling range cells 27 and 40 as having questionable mean estimates. This contradiction between width estimates and power levels, concerning valid mean estimates, reflects a need for comparing the results of one test against the results of another before making a decision concerning the validity of a mean estimate.

Filter Based on the Clutter
in a Single Range Cell

The 10th order complex coefficient filters designed for each range cell were able to eliminate bias in the pulse-pair mean estimates due to clutter while preserving the microburst information. This ability to preserve the microburst information after filtering is evidence by the resulting output power levels and reasonable width estimates. An alternative approach to designing filters for each individual range cell is to define a single set of filter coefficients that can be used for several adjacent range cells or over the
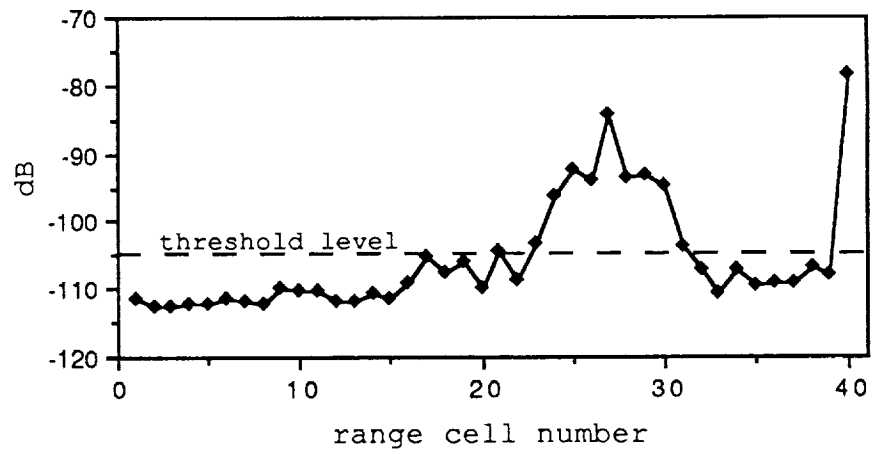
Figure 32. Power levels after filtering using the filter coefficients obtained from the clutter within each range cell.

entire set. The design of this filter could still be based on clutter statistics. The filter designed for range cell 20 was choosen to test the effects of using one filter over several range cells. The range cells selected for evaluation are those around the center of the microburst which contain clutter as well as microburst information. The magnitude and phase response of this filter is given in Figures 33 and 34, respectively. This filter has a stop band centered at zero Doppler which is characteristic of the clutter in the majority of these range cells as can be seen in Appendix F.

Figure 35 gives the pulse-pair mean estimates after filtering with the clutter rejection filter designed for range cell 20. A comparison in Figure 36 with the mean estimates from the dry microburst without clutter seems to support the possible use of one filter over range cells 23 through 32. The spectral content of the filtered range cells is given in Appendix I. In order to evaluate the mean estimates after filtering, an analysis of the power levels and width estimates will be made based on the thresholds set in the previous section.

Figure 37 gives the pulse-pair width estimates for the filtered dry microburst plus clutter data. Based on a threshold of 7m/sec, range cells 23-26 and 28-31 would be defined as having valid mean estimates. This result compares well with those found using the filters designed for each range cell. The power levels resulting from filtering are given in Figure 38 and are consistent with those found in the
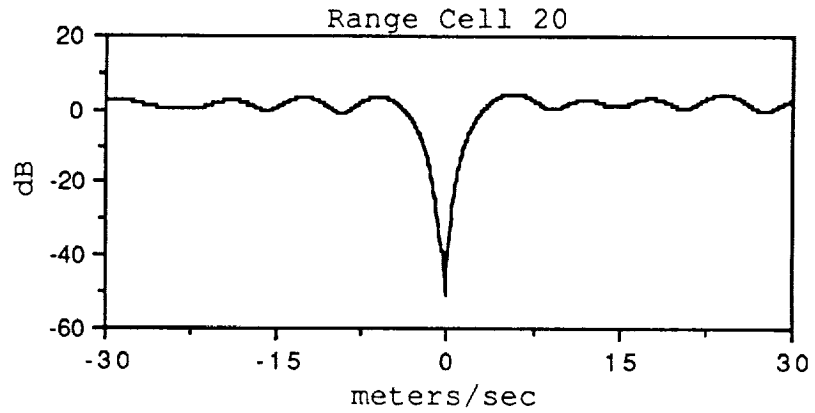
Figure 33. Magnitude response of the filter designed for range cell 20.
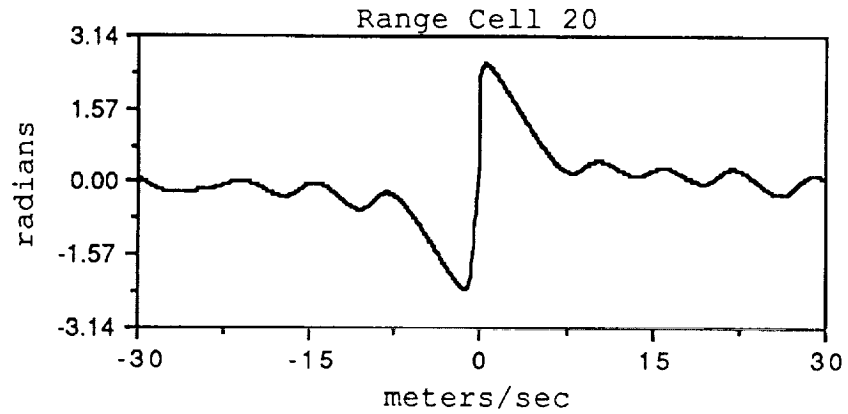
Figure 34. Phase respone of the filter designed for range cell 20.
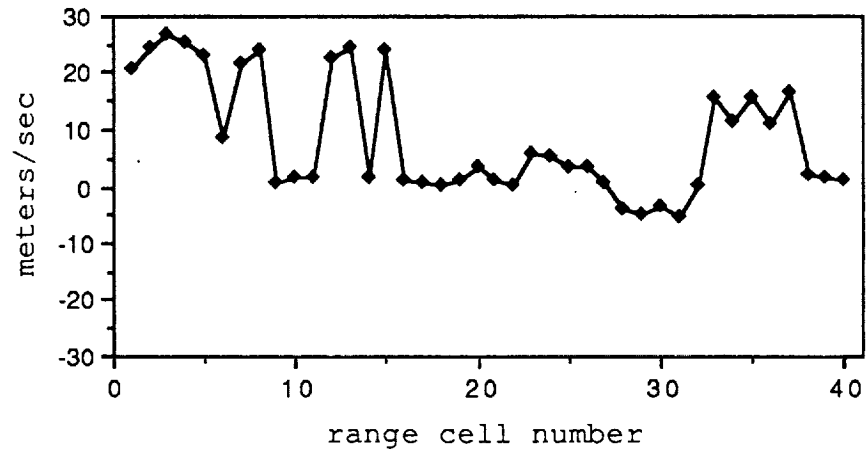
Figure 35. Pulse-pair mean estimates after filtering using the filter coefficients for range cell 20.
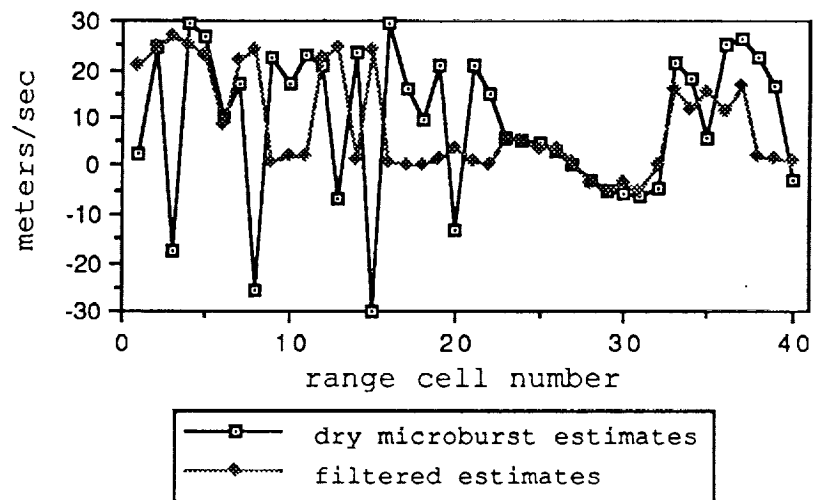
Figure 36. Pulse-pair mean estimates after filtering using the filter coefficients for range cell 20 compared to estimates given in the case of a dry microburst without clutter.
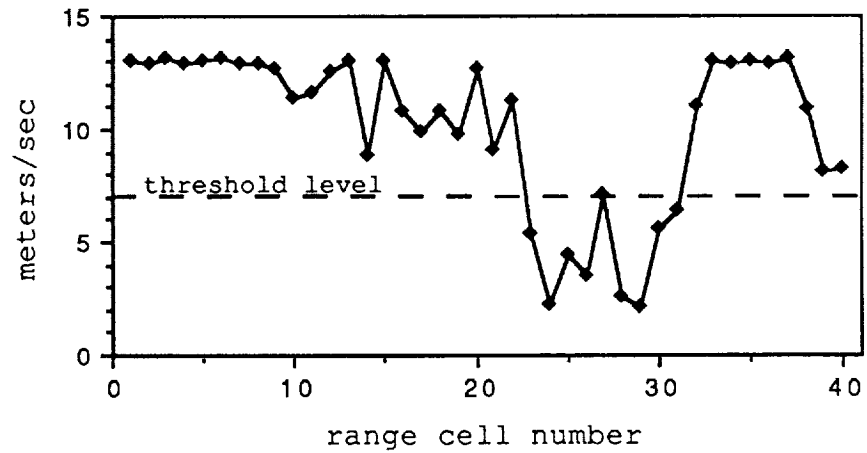
Figure 37. Pulse-pair width estimates after filtering using the filter coefficients for range cell 20.
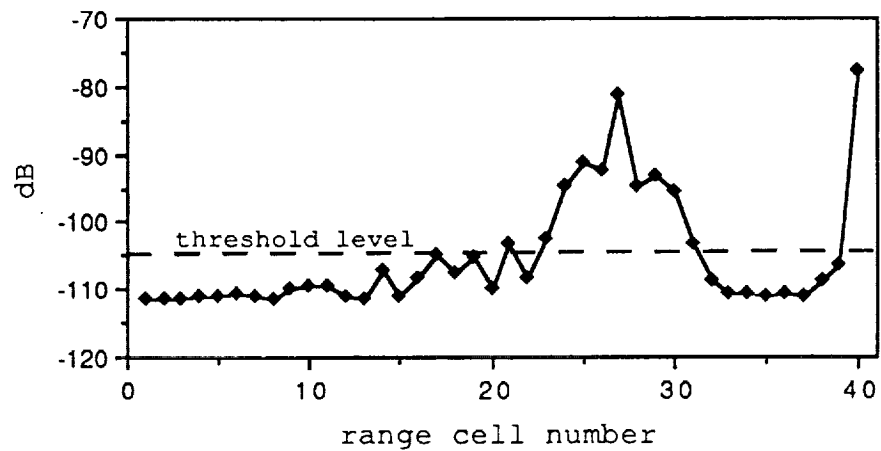
Figure 38. Power levels after filtering using the filter coefficients for range cell 20.

previous case using the appropriate filter for each range cell. These results suggest the possible use of one filter over several range cells where the range cells are known to have a similar clutter spectrum.

Comparison with a Pulse Canceller

In order to evaluate the filters based on modeling the clutter, a comparison will be made using a pulse canceller filter which is found in land based air traffic control radar systems [9]. The pulse canceller takes the form of a first order difference equation with input y_T and output x_T where

$$x_T = y_T - y_{T-1} .$$

(43)

The magnitude and phase responses of this filter are given in Figures 39 and 40, respectively. Figure 41 gives the pulse-pair mean estimates after filtering with the pulse canceller. A comparison in Figure 42 with the mean estimates from the dry microburst without clutter case reveals a larger error in the mean estimates for range cells 23 through 31 when compared to that found in the case of using the filter designed from the clutter within each range cell, Figure 28. The spectral content of the filtered range cells is given in Appendix J. For comparison, Figure 43 gives the filtered results for range cell 24 using the filter designed for range cell 24, the filter designed for range cell 20, and the pulse canceller, respectively. This comparison reveals a larger attenuation of the microburst information in the case of the
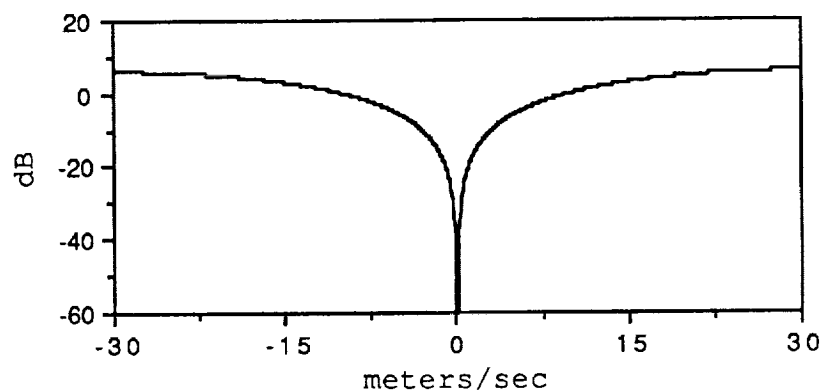
Figure 39. Magnitude response of a pulse canceller filter.
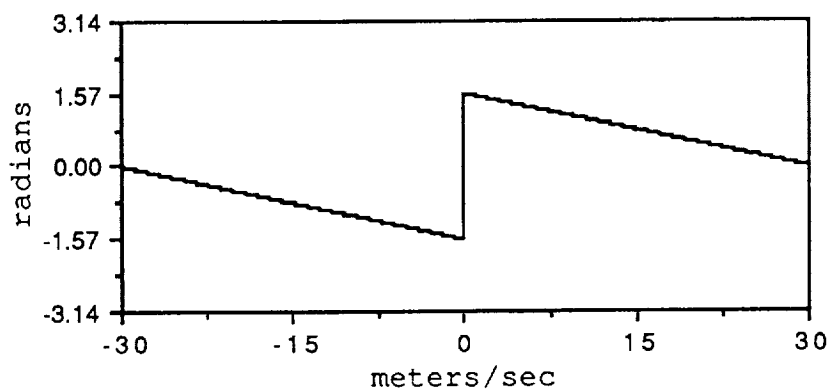
Figure 40. Phase respone of a pulse canceller filter.
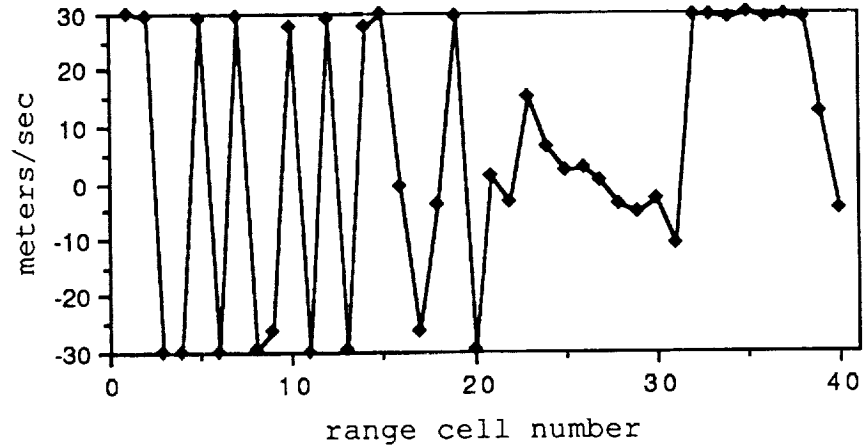
Figure 41. Pulse-pair mean estimates after filtering using a pulse canceller.
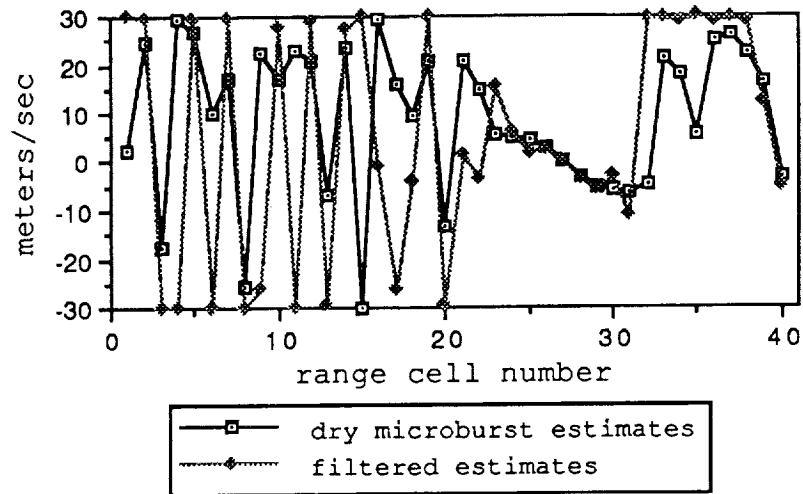
Figure 42. Pulse-pair mean estimates after filtering using a pulse canceller compared to estimates given in the case of a dry microburst without clutter.
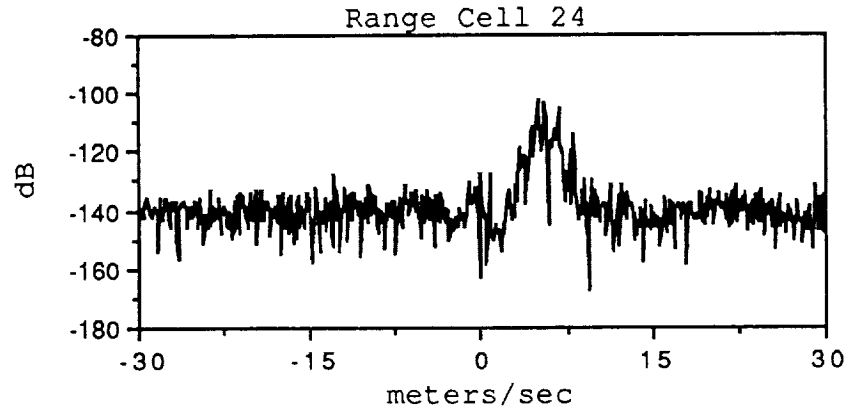
(a) Filtered using range cell 24 model coefficients.
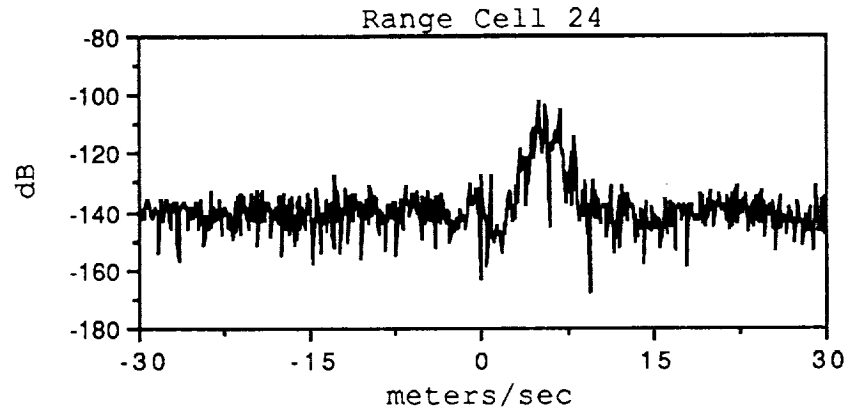
(b) Filtered using range cell 20 model coefficients.
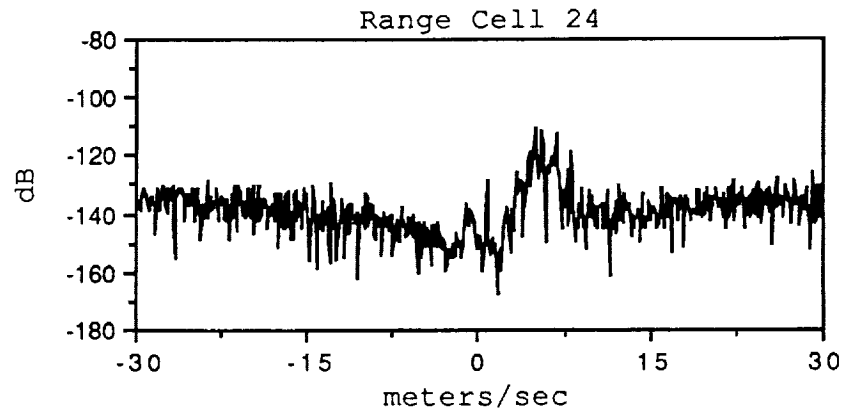
(c) Filtered using a pulse canceller.

Figure 43. Spectrum of range cell 24 after filtering.

pulse canceller. This is reflected in the lower power levels given in Figure 44 for the pulse canceller case near the center of the microburst. These resulting lower SNR's contribute to the large width estimates found after using the pulse canceller, shown in Figure 45. Only two range cells, 28 and 29, have width estimates within the 7m/sec threshold previously set to define a valid mean estimate.
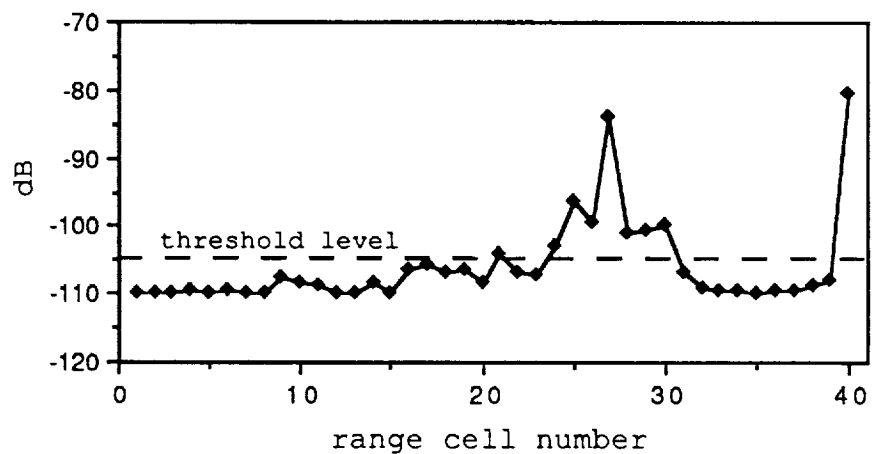
Figure 44. Power levels after filtering using a pulse canceller.
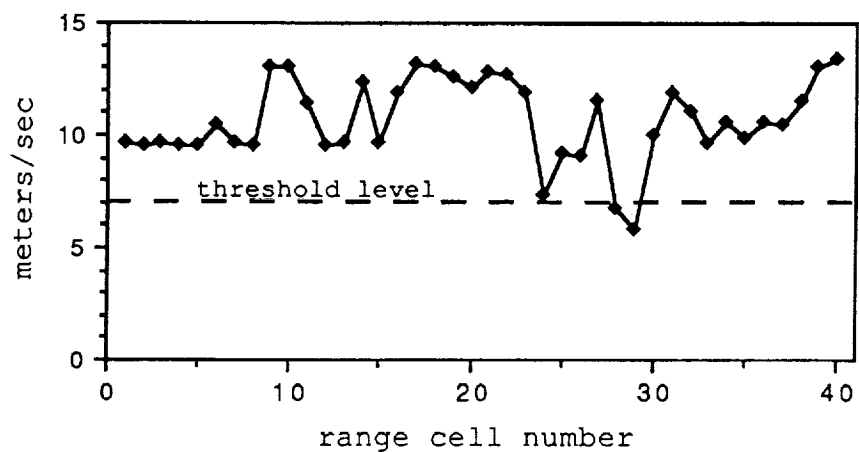
Figure 45. Pulse-pair width estimates after filtering using a pulse canceller.

CHAPTER V

CONCLUSIONS

The potential for disaster associated with low altitude windshear in the near terminal area mandates the need for some type of detection system. It is anticipated that an airborne pulsed Doppler radar system used to measure radial components of windspeed can help assess the hazard associated with windshear particularly in the case of a microburst. Clutter presents a major obstacle to the use of airborne radar at low altitudes as a remote sensor of windshear. Large clutter returns from objects in the terminal area can impose a bias on estimates of the radial components of windspeed. This thesis has addressed the use of adaptive clutter rejection filters to eliminate the source of this bias.

The adaptive clutter rejection filters investigated here are based on modeling the clutter as a low order autoregressive process. A low order filter offers implementation advantages in terms of memory requirements and computational load, both advantageous for real time implementation. The adaptive property of these clutter rejection filters offers the ability to continuously update and improve the filters as new clutter return becomes available. Because the filter coefficients are obtained from a complex square root normalized recursive least squares

lattice estimation algorithm, stable clutter rejection filters are assured. The least squares adaptive method for determining the filter coefficients also offers a faster convergence rate compared to gradient adaptive methods, and the normalization allows for implementation using fixed point arithmetic further enhancing the potential for real time implementation. Fast convergence rates are important since the clutter return is generally non-stationary over the long-term but is assumed stationary over short observation intervals. Additionally, complex coefficient FIR clutter rejection filters allow for non-symmetric magnitude responses, required in cases where the clutter spectrum is non-symmetric about zero Doppler.

Several filtering schemes used to eliminate the clutter have been considered. One such filtering scheme defines a model for each range cell at any point along the final approach to a runway. These models can then be indexed by geographical location for future use. It has been demonstrated here that the same model may be used for several range cells, thereby decreasing the amount of information to be stored. More research is needed to make general conclusions.

The pulse-pair algorithm has been used herein to determine the average windspeed within a range cell from the filtered return data. The resulting mean estimates tend to be unstable or biased when the signal to noise ratio is small. This thesis has proposed the use of pulse-pair width

estimates and power levels to form a statistic for establishing confidence in pulse-pair mean estimates.

Further research in the area of stationarity and repeatability as applied to the environment being modeled is warranted. Another area of research not addressed in this thesis but needing further study is the determination of the optimum model order. Further study of clutter environments is also needed before defining the appropriate filtering scheme to use. Particular emphasis will need to be placed on dynamic clutter models.

APPENDICES

Appendix A

The Complex Square Root Normalized Recursive
Least Squares Lattice Estimation Algorithm

Introduction

The square root normalized recursive least squares lattice estimation algorithm presented by Lee, Morf, and Friedlander [22] was derived for the real data case. This appendix looks at adapting the algorithm to process complex data. The need for a complex form of the algorithm arises when processing IQ data from a radar return or other sources of data requiring quadrature sampling [16]. This appendix will not discuss the advantages of the square root normalized form of the algorithm, but references concerning the advantages are given by Lee [22]. Honig [18] and Friedlander [14] address the issue of obtaining the linear prediction error filter coefficients from the normalized lattice parameters for the real data case. A derivation will be developed for the complex coefficient case based on that presented by Honig.

This appendix is divided into six major sections. The first section discusses the least squares approach to estimating the complex coefficients in an autoregressive model. The next two sections develop the order- and time-updates required in a recursive lattice estimation algorithm. A normalization is introduced in section four that reduces the number of updates required in the lattice

estimation algorithm. The fifth section is a summary of the equations and intializations required to implement the complex square root normalized recursive least squares lattice estimation algorithm. The final section uses the normalized lattice parameters to determine the complex prediction error filter coefficients.

Autoregressive Model
Least Squares Estimate

The task of fitting an Nth-order autoregressive model to a complex set of data $\{x_t, \ 0 \leq t \leq T\}$ involves finding a complex set of coefficients $\{a_{N,i}, \ i=1,\ldots,N\}$ to minimize the sum of the squared prediction errors

$$|\underline{e}|^2 = (\underline{x}'^* + \underline{A}_N'^* X'^*)(\underline{x} + X\underline{A}_N) \tag{A.1}$$

where

$$\underline{e} = \underline{x} + X\underline{A}_N \tag{A.2}$$

$$\underline{x}' = [x_0,\ldots,x_T] \tag{A.3}$$

$$\underline{A}_N' = [a_{N,1},\ldots,a_{N,N}] \tag{A.4}$$

and

$$X = \begin{bmatrix} 0 & 0 & \ldots & 0 \\ x_0 & 0 & \ldots & 0 \\ \cdot & x_0 & \ldots & 0 \\ \cdot & \cdot & \ldots & x_0 \\ \cdot & \cdot & \ldots & \cdot \\ x_{T-1} & x_{T-2} & \ldots & x_{T-N} \end{bmatrix} . \tag{A.5}$$

The transpose of a vector is noted as $\underline{x}'$, and the complex conjugate of a vector is noted as $\underline{x}^*$. The minimization is obtained by taking the partial derivative with respect to the complex coefficient vector $\underline{A}_N$ and setting the result equal to zero. The steps required for complex differentiation are discussed by Miller [23]. Expanding the product in Equation (A.1)

$$|\underline{e}|^2 = (\underline{x}'^*\underline{x}) + (\underline{x}'^*X\underline{A}_N) + (\underline{A}_N'^*X'^*\underline{x}) + (\underline{A}_N'^*X'^*X\underline{A}_N) \qquad (A.6)$$

and taking the partial derivative with respect to $\underline{A}_N$ yields the following

$$\partial[\underline{x}'^*\underline{x}]/\partial\underline{A}_N = 0 \qquad (A.7)$$

$$\partial[\underline{x}'^*X\underline{A}_N]/\partial\underline{A}_N = X'\underline{x}^* \qquad (A.8)$$

$$\partial[\underline{A}_N'^*X'^*\underline{x}]/\partial\underline{A}_N = 0 \qquad (A.9)$$

$$\partial[\underline{A}_N'^*X'^*X\underline{A}_N]/\partial\underline{A}_N = X'X^*\underline{A}_N^* \, . \qquad (A.10)$$

Setting the sum of the partial derivatives in Equations (A.7), (A.8), (A.9), and (A.10) equal to zero and solving for $\underline{A}_N$ yields

$$\underline{A}_N = -[X'^*X]^{-1}X'^*\underline{x} \qquad (A.11)$$

the least squares estimate of the complex predictor coefficients.

C -2

Projection Operators

The complex coefficient vector in the prediction error in Equation (A.2) can now be replaced by the least squares estimate of the complex coefficient vector in Equation (A.11) to yield

$$\underline{e} = \underline{x} - X[X'^{*}X]^{-1}X'^{*}\underline{x} \; . \tag{A.12}$$

Using the least squares estimate of the prediction error in Equation (A.12), a projection operator can now be defined as

$$P_N = X[X'^{*}X]^{-1}X'^{*} \; . \tag{A.13}$$

This operator projects the vector $\underline{x}$ onto the subspace of past observations (the columns of X). Its orthogonal complement can be defined as

$$P_N^{\perp} = (I - P_N) \; . \tag{A.14}$$

The orthogonal complement of the projection operator P_N in Equation (A.14) can now be used to define the prediction error

$$\underline{e} = P_N^{\perp}\underline{x} \tag{A.15}$$

as a projection of the observed data onto a subspace which is perpendicular to the one containing past observations.

A property of projection operators that will be useful is $P_N P_N = P_N$ and $P_N^{\perp}P_N^{\perp} = P_N^{\perp}$. A proof of this property of projection operators is

$$P_N P_N = X[X'^*X]^{-1}[X'^*X][X'^*X]^{-1}X'^*$$
$$= X[X'^*X]^{-1}X'^*$$
$$= P_N \ . \tag{A.16}$$

Order-Update Recursions

Sample Space

This derivation of the square root normalized recursive least squares lattice estimation algorithm will consider a single channel complex data case where Lee [22] applied it to a multichannel case for real data. An observation of time samples $\{x_t \in C, \ 0 \leq t \leq T\}$ in vector form is defined as

$$|x\rangle_T = [x_0, \ x_1, \ \ldots, \ x_T]' \ . \tag{A.17}$$

Also, a delay operator, z^{-n}, on $|x\rangle_T$ is defined as

$$|z^{-1}x\rangle_T = [0, \ x_0, \ \ldots, \ x_{T-1}]' \tag{A.18}$$

where x_t, $t < 0$ is assumed to be equal to zero.

The linear space H_T containing $|x\rangle_T$ is spanned by the $T+1$ observations vectors $\{|x\rangle_T, |z^{-1}x\rangle_T, \ \ldots, |z^{-T}x\rangle_T\}$. The vector inner product on H_T is defined as

$$\langle x|y\rangle_T = (|x\rangle_T'^*)(|y\rangle_T)$$
$$= \sum_{t=0}^{T} x_t^* y_t \tag{A.19}$$

where $|x\rangle_T$, $|y\rangle_T \in H_T$.

For convenience, the transpose of $|x\rangle_T$ is defined as $_T\langle x|$. A matrix composed of elements of H_T will be defined as $|X\rangle_T$ where the matrix transpose is noted as $_T\langle X|$, and the

matrix inner product is defined as

$$\langle X|Y\rangle_T = (|X\rangle_T'^*)(|Y\rangle_T) . \tag{A.20}$$

Subspace of Past Observations

The subspace of H_T containing past observations is denoted by $X_{1,n,T}$ and is spanned by

$$\{|z^{-1}x\rangle_T, \ldots, |z^{-n}x\rangle_T\}, \qquad n \leq T \tag{A.21}$$

where,

$$|X_{1,n}\rangle_T = [|z^{-1}x\rangle_T, \ldots, |z^{-n}x\rangle_T] . \tag{A.22}$$

The projection operator on the subspace $X_{1,n,T}$ is

$$P_{1,n,T} = |X_{1,n}\rangle_T\langle X_{1,n}|X_{1,n}\rangle_T^{-1}\langle X_{1,n}|_T^* . \tag{A.23}$$

Also, the orthogonal complement of the projection operator defined on $X_{1,n,T}$ is

$$P^{\perp}_{1,n,T} = (I - P_{1,n,T}). \tag{A.24}$$

Coordinate Map

In order to extract the most recent time sample, a coordinate map is defined such that $\Pi(|x\rangle_T) = x_T$. A vector form of this operator can be written as

$$|\Pi\rangle_T = [0, 0, \ldots, 0, 1]' \tag{A.25}$$

where $(_T\langle\Pi|)(|x\rangle_T) = x_T$. A coordinate projector can also be defined in terms of $|\Pi\rangle_T$ such that

$$P_T|x\rangle_T = [0,0, \ldots, x_T]' \tag{A.26}$$

where

$$P_T = |n\rangle_T\langle n|_T^* . \tag{A.27}$$

Forward and Backward Prediction Errors

Projecting $|x\rangle_T$ onto the subspace of past observations, $X_{1,n,T}$, yields an nth order forward prediction error

$$|e_n\rangle_T = |x\rangle_T - P_{1,n,T}|x\rangle_T = P^\perp_{1,n,T}|x\rangle_T \tag{A.28}$$

which is orthogonal to $X_{1,n,T}$ but lies in $X_{0,n,T}$. The forward prediction error covariance can be defined as

$$R^e_{n,T} = \langle e_n|e_n\rangle_T = \langle e_n|x\rangle_T = \langle x|e_n\rangle_T . \tag{A.29}$$

An nth-order backward prediction error vector can also be defined as

$$|r_n\rangle_T = |z^{-n}x\rangle_T - P_{0,n-1,T}|z^{-n}x\rangle_T$$
$$= P^\perp_{0,n-1,T}|z^{-n}x\rangle_T . \tag{A.30}$$

A delayed version of the backward prediction error

$$|z^{-1}r_n\rangle_T = P^\perp_{1,n,T}|z^{-n-1}x\rangle_T \tag{A.31}$$

will be needed in the lattice recursions. Its covariance is

$$R^r_{n,T-1} = \langle z^{-1}r_n|z^{-1}r_n\rangle_T = \langle r_n|r_n\rangle_{T-1} . \tag{A.32}$$

Decomposition of Subspaces

The fact that $|e_n\rangle_T$ lies in $X_{0,n,T}$ and is orthogonal to $X_{1,n,T}$ leads to the direct sum of the subspaces such that

$$X_{0,n,T} = X_{1,n,T} \oplus |e_n\rangle_T \quad . \tag{A.33}$$

The projection operators can be updated in a similar fashion with

$$P_{0,n,T} = P_{1,n,T} + |e_n\rangle_T \langle e_n | e_n\rangle_T^{-1} \langle e_n |_T^* \tag{A.34}$$

and its orthogonal complement

$$P^\perp_{0,n,T} = P^\perp_{1,n,T} - |e_n\rangle_T \langle e_n | e_n\rangle_T^{-1} \langle e_n |_T^* \quad . \tag{A.35}$$

Using the delayed backward prediction error, the projection operator, $P_{1,n,T}$, can be updated as

$$P_{1,n+1,T} = P_{1,n,T} + |z^{-1}r_n\rangle_T \langle z^{-1}r_n | z^{-1}r_n\rangle_T^{-1} \langle z^{-1}r_n |_T^* \tag{A.36}$$

and its orthogonal complement as

$$P^\perp_{1,n+1,T} = P^\perp_{1,n,T} - |z^{-1}r_n\rangle_T \langle z^{-1}r_n | z^{-1}r_n\rangle_T^{-1} \langle z^{-1}r_n |_T^*. \tag{A.37}$$

Error Order-Update

Equation (A.37) is an expression for the projection order-update at time T. The order-update of the forward prediction error is obtained by operating on $|x\rangle_T$ using Equation (A.37) to yield

$$|e_{n+1}\rangle_T = |e_n\rangle_T - |z^{-1}r_n\rangle_T \langle z^{-1}r_n | z^{-1}r_n\rangle_T^{-1} \langle z^{-1}r_n | e_n\rangle_T \quad . \tag{A.38}$$

At this point, a reflection coefficient, $k_{n+1,T}$, will be

defined as

$$k_{n+1,T} = \langle e_n | z^{-1} r_n \rangle_T .$$

(A.39)

Using the forward prediction error covariance in Equation (A.32) and the reflection coefficient in Equation (A.39), the forward prediction error order-update in Equation (A.38) can be written as

$$e_{n+1,T} = e_{n,T} - r_{n,T-1} R^{-r}_{n,T-1} k^*_{n+1,T}$$

(A.40)

while looking only at the Tth component. Comparing this to Lee [22], a conjugate of the reflection coefficient in Equation (A.40) is required for complex data due to the definition of the inner product in Equation (A.19) and the reflection coefficient in Equation (A.39). The covariance order-update for the forward prediction error in Equation (A.38) is given by

$$\langle e_{n+1} | e_{n+1} \rangle_T = \langle e_n | e_n \rangle_T - \langle e_n | z^{-1} r_n \rangle_T$$
$$\langle z^{-1} r_n | z^{-1} r_n \rangle_T^{-1} \langle z^{-1} r_n | e_n \rangle_T$$

(A.41)

or

$$R^e_{n+1,T} = R^e_{n,T} - k^*_{n+1,T} R^{-r}_{n,T-1} k_{n+1,T} .$$

(A.42)

Using Equation (A.35), a similar order-update can be obtained for the backward prediction error. Operating on $|z^{-n-1} x \rangle_T$ yields

$$|r_{n+1} \rangle_T = |z^{-1} r_n \rangle_T - |e_n \rangle_T \langle e_n | e_n \rangle_T^{-1} \langle e_n | z^{-1} r_n \rangle_T$$

(A.43)

or

$$r_{n+1,T} = r_{n,T-1} - e_{n,T} R^- e_{n,T} k_{n+1,T} \cdot \tag{A.44}$$

The covariance order-update for the backward prediction error is

$$\langle r_{n+1} | r_{n+1} \rangle_T = \langle z^{-1} r_n | z^{-1} r_n \rangle_T - \langle z^{-1} r_n | e_n \rangle_T$$
$$\langle e_n | e_n \rangle_T^{-1} \langle e_n | z^{-1} r_n \rangle_T \tag{A.45}$$

or

$$R^r_{n+1,T} = R^r_{n,T-1} - k_{n+1,T}^* R^- e_{n,T} k_{n+1,T} \cdot \tag{A.46}$$

Time-Update Recursions

Decomposition of Projections

A geometric approach will be taken to formulate the time-update for the least squares lattice algorithm. A simple example of projecting a vector $|y\rangle_T$ onto a vector $|x\rangle_T$, in a three dimensional real space (Figure A-1), by decomposing $|x\rangle_T$ into its past and present components will facilitate the development of the projection time-update. Using the coordinate projector defined in Equation (A.26), two new vectors, containing the past and present components of $|x\rangle_T$, will be defined as

$$|x_\Pi\rangle_T \equiv P_T |x\rangle_T = [0, 0, \ldots, X_T]' \tag{A.47}$$

and

$$|x_-\rangle_T \equiv P^\perp_T |x\rangle_T = [x_0, x_1, \ldots, x_{T-1}, 0]' \cdot \tag{A.48}$$
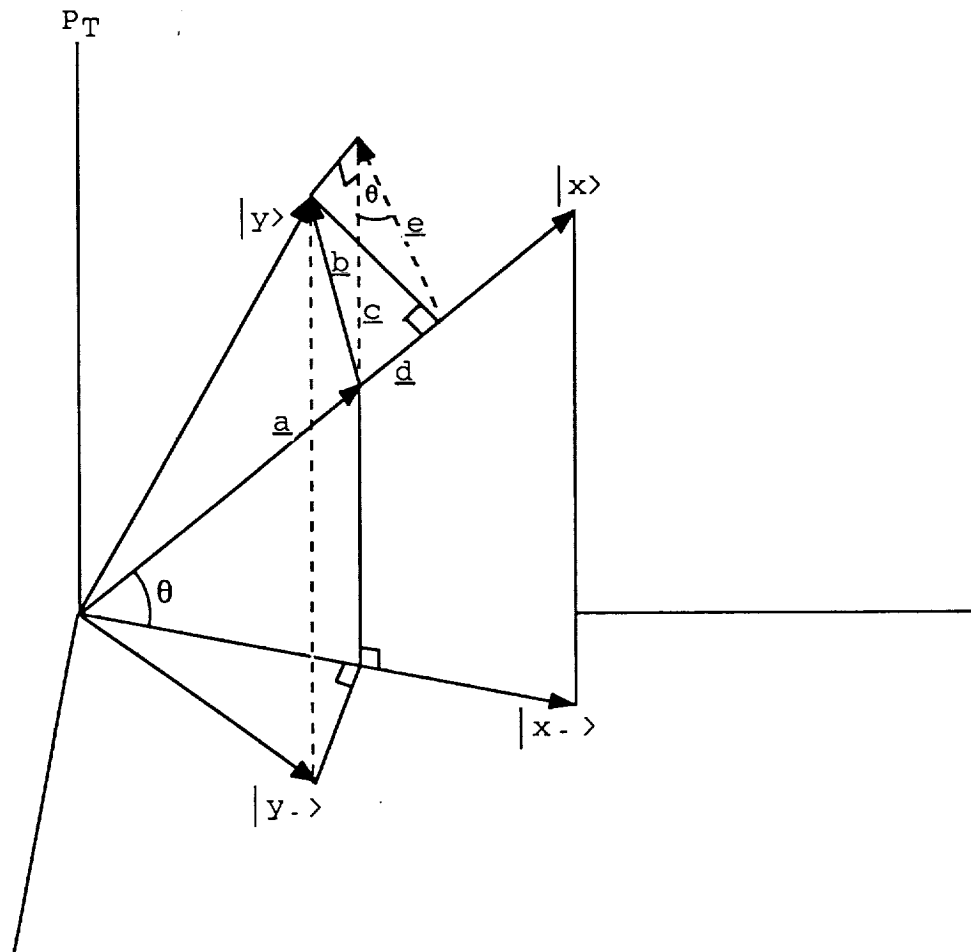
Figure A-1.   Decomposition of projections by oblique projection.

Several important relationships pertaining to Equations (A.47) and (A.48) are $\langle y_\Pi | x_\Pi \rangle_T = \langle y_\Pi | x \rangle_T = \langle y | x_\Pi \rangle_T$ and $\langle y_- | x_- \rangle_T = \langle y | x_- \rangle_T = \langle y_- | x \rangle_T$, respectively.

Taking a step in the opposite direction, the vector $|y\rangle_T$ may be decomposed into $|y_\Pi\rangle_T$ and $|y_-\rangle_T$ and then projected onto $|x\rangle_T$ such that

$$P_x |y\rangle_T = P_x |y_-\rangle_T + P_x |y_\Pi\rangle_T \ . \tag{A.49}$$

At this point the time index, T, will be dropped. Expanding Equation (A.49) yields

$$|x\rangle\langle x|x\rangle^{-1}\langle x|y\rangle = |x\rangle\langle x|x\rangle^{-1}\langle x|y_-\rangle + |x\rangle\langle x|x\rangle^{-1}\langle x|y_\Pi\rangle$$
$$= |x\rangle\langle x|x\rangle^{-1}\langle x_-|y\rangle + |x\rangle\langle x|x\rangle^{-1}\langle x_\Pi|y\rangle \ .$$

$$\tag{A.50}$$

The second equality of Equation (A.50) reveals a decomposition of $|x\rangle$ into $|x_\Pi\rangle$ and $|x_-\rangle$.

In order to develop a projection update in terms of $|x_\Pi\rangle$ and $|x_-\rangle$, an oblique projection needs to be defined. An oblique projection is a vector composed of the product of the magnitude of an orthogonal projection of $|y\rangle$ onto $|x_-\rangle$ and $|x\rangle$. The oblique projection takes the form

$$P_{x_-} |y\rangle = |x\rangle\langle x_-|x_-\rangle^{-1}\langle x_-|y\rangle \ . \tag{A.51}$$

A correction component based on the present time sample $|x_\Pi\rangle$ is needed to complete the projection of $|y\rangle$ onto $|x\rangle$.

The decomposition of $P_x|y\rangle$ based on the oblique projection in Equation (A.51) yields

$$P_x|y\rangle = P_{x_-}|y\rangle + P_x P_T P^{\perp}_{x_-}|y\rangle \qquad (A.52)$$

where the second term on the right-hand side of Equation (A.52) is the correction component based on the present time sample. A derivation of Equation (A.52) is given as a geometric formulation in the next section.

Geometric Formulation

The first term on the right-hand side of Equation (A.52) can be expressed as

$$P_{x_-}|y\rangle = |x\rangle\langle x_-|x_-\rangle^{-1}\langle x_-|y_-\rangle . \qquad (A.53)$$

Using previously defined relationships, the vector $|y\rangle$ in Equation (A.51) has been replaced by the vector $|y_-\rangle$ to form Equation (A.53). The inner products in Equation (A.53) represent the coefficient defined at time T-1. This relationship can be seen in Figure A-1 where $\underline{a}$ is $P_{x_-}|y\rangle$.

As stated previously the second term on the right-hand side of Equation (A.52) is a correction factor. Referring to Figure A-1, the term $P^{\perp}_{x_-}|y\rangle$ is the vector $\underline{b}$ where

$$P^{\perp}_{x_-}|y\rangle = |y\rangle - P_{x_-}|y\rangle . \qquad (A.54)$$

The coordinate projector P_T allows for the extraction of the most recent component. Therefore, $P^{\perp}_{x_-}|y\rangle$ is projected onto P_T to form $\underline{c}$ in Figure A-1. Finally, the result can be projected onto $|x\rangle$ to form $P_x P_T P^{\perp}_{x_-}|y\rangle$. This correction factor $\underline{d}$ can now be added to $\underline{a}$ to form $P_x|y\rangle$.

At this point a more rigorous proof that Equation (A.52) is equal to Equation (A.50) is given. Taking the first term on the right-hand side of Equation (A.50)

$$|x\rangle\langle x|x\rangle^{-1}\langle x|y\rangle = |x\rangle\langle x|x\rangle^{-1}[\langle x_-|x\rangle\langle x_-|x\rangle^{-1}]\langle x_-|y\rangle$$

$$= |x\rangle\langle x|x\rangle^{-1}[\langle x|x\rangle-\langle x_\Pi|x\rangle]$$

$$\langle x_-|x\rangle^{-1}\langle x_-|y\rangle$$

$$= |x\rangle\langle x_-|x_-\rangle^{-1}\langle x_-|y\rangle - |x\rangle\langle x|x\rangle^{-1}$$

$$\langle x_\Pi|x\rangle\langle x_-|x_-\rangle^{-1}\langle x_-|y\rangle$$

$$= P_{x_-}|y\rangle - P_x P_T P_{x_-}|y\rangle \tag{A.55}$$

and adding the second term of Equation (A.50) to (A.55) gives

$$P_x|y\rangle = P_{x_-}|y\rangle - P_x P_T P_{x_-}|y\rangle + P_x P_T|y\rangle$$

$$= P_{x_-}|y\rangle + P_x P_T P^\perp_{x_-}|y\rangle . \tag{A.56}$$

From Equation (A.56), the projection orthogonal to $P_x|y\rangle$ can be written as

$$P^\perp_x|y\rangle = P^\perp_{x_-}|y\rangle - P_x P_T P^\perp_{x_-}|y\rangle . \tag{A.57}$$

The inner product of $|y\rangle$ with Equation (A.57) will lead to the desired form needed for the reflection coefficient and error covariance time-updates. Therefore, taking the inner product and replacing the time indexes results in

$$\langle y|P^\perp_x|y\rangle_T = \langle y|P^\perp_x|y\rangle_{T-1} + \langle y|P^\perp_x|\pi\rangle_T\langle\pi|P^\perp_{x_-}|y\rangle_T . \tag{A.58}$$

This can be proven by writing Equation (A.57) as

$$P^\perp_x|y\rangle = P^\perp_{x_-}|y\rangle - P_T P^\perp_{x_-}|y\rangle + P_T P^\perp_{x_-}|y\rangle - P_x P_T P^\perp_{x_-}|y\rangle$$

$$(A.59)$$

and using the definition of the orthogonal projection to yield

$$P^\perp_x|y\rangle = P^\perp_T P^\perp_{x_-}|y\rangle + P^\perp_x P_T P^\perp_{x_-}|y\rangle \ .$$

$$(A.60)$$

The result of the inner product $|y\rangle$ and Equation (A.60) can be written as

$$\langle y|P^\perp_x|y\rangle = \langle y| P^\perp_T P^\perp_{x_-}|y\rangle + \langle y|P^\perp_x P_T P^\perp_{x_-}|y\rangle \ .$$

$$(A.61)$$

The first term on the right hand side of Equation (A.61) is the inner product of the error in projecting $|y_-\rangle$ onto $|x_-\rangle$ which is illustrated in Figure A-1. Given this projection, the time-update for the inner product can be written as

$$\langle y|P^\perp_x|y\rangle_T = \langle y|P^\perp_x|y\rangle_{T-1} + \langle y|P^\perp_x|n\rangle_T \langle n|P^\perp_{x_-}|y\rangle_T \ .$$

$$(A.62)$$

Angle Between Two Subspaces

The concept of an angle between two subspaces will be developed in this section in order to expand on the time-update of the inner product in Equation (A.58). Referring to Figure A-1 let the angle between $|x_-\rangle$ and $|x\rangle$ be denoted by θ. The geometric relation can be expressed as

$$\cos^2\theta = 1 - \langle x_\Pi|x_\Pi\rangle/\langle x|x\rangle = \langle x_-|x_-\rangle/\langle x|x\rangle$$

$$(A.63)$$

or

$$\sin^2\theta = \langle x_\Pi | x_\Pi \rangle / \langle x | x \rangle \ . \tag{A.64}$$

An alternative form of $\sin^2\theta$ can be written in terms of projections defined in the previous section where

$$\sin^2\theta = \langle \Pi |^* P_X | \Pi \rangle \ . \tag{A.65}$$

Considering an n-dimensional complex space, $X_{1,n}$, Equation (A.64) can be written as

$$\begin{aligned}
\sin^2\theta_{1,n} &= \langle \Pi | X_{1,n} \rangle \langle X_{1,n} | X_{1,n} \rangle^{-1} \langle X_{1,n} | \Pi \rangle \\
&= \langle \Pi |^* P_{1,n} | \Pi \rangle
\end{aligned} \tag{A.66}$$

or Equation (A.63) as

$$\cos^2\theta_{1,n} = \langle \Pi |^* P^\perp_{1,n} | \Pi \rangle \ . \tag{A.67}$$

An order-update for $\cos^2\theta_{1,n,T}$ can be found using Equation (A.37) where

$$\cos^2\theta_{1,n+1,T} = \cos^2\theta_{1,n,T} - r^*_{n,T-1} R^{-r}_{n,T-1} r_{n,T-1} \ . \tag{A.68}$$

Another update that will be needed in developing an algorithm to determine the filter coefficients is

$$\cos^2\theta_{0,n,T} = \cos^2\theta_{0,n-1,T} - r^*_{n,T} R^{-r}_{n,T} r_{n,T} \tag{A.69}$$

where it should be noted that $\cos^2\theta_{1,n,T} = \cos^2\theta_{0,n-1,T-1}$. Also, for notational purposes in later sections let $\gamma_{n,T} = \cos^2\theta_{0,n-1,T}$.

Having defined $\cos^2\theta$, it is possible to show the relationship between the orthogonal and oblique projections

on $|x\rangle$. Multiplying Equation (A.57) by P_T and using Equation (A.67), the relationship is found to be

$$
\begin{aligned}
P_T P^{\perp}_x |y\rangle &= P_T P^{\perp}_{x-} |y\rangle - P_T P_x P_T P^{\perp}_{x-} |x\rangle \\
&= [P_T - P_T P_x] P_T P^{\perp}_{x-} |y\rangle \\
&= P_T P^{\perp}_x P_T P^{\perp}_{x-} |y\rangle \\
&= P_T P^{\perp}_{x-} |y\rangle \cos^2\theta \; .
\end{aligned}
\tag{A.70}
$$

Exact Time-Update Formula

Using Equations (A.58) and (A.70), the time update of the inner product using the orthogonal projection, $P^{\perp}_{1,n,T}$, can now be written as

$$
\begin{aligned}
\Phi \langle u|^* P^{\perp}_{1,n,T} |v\rangle_T &\equiv \langle u|^* P^{\perp}_{1,n,T} |v\rangle_T - \\
&\quad \langle u|^* P^{\perp}_{1,n,T-1} |v\rangle_{T-1} \\
&= \langle u|^* P^{\perp}_{1,n,T} |\pi\rangle_T \\
&\quad \langle \pi|^* P^{\perp}_{1,n,T} |v\rangle \sec^2\theta_{1,n,T}
\end{aligned}
\tag{A.71}
$$

where $|u\rangle$, $|v\rangle \in H_T$.

Time-Updates

Using Equation (A.71), the time-update for the reflection coefficients can be written as

$$
\begin{aligned}
k_{n+1,T} &= k_{n+1,T-1} + \langle x| P^{\perp}_{1,n,T} |\pi\rangle_T \\
&\quad \langle \pi| P^{\perp}_{1,n,T} |z^{-n-1} x\rangle_T \sec^2\theta_{1,n,T} \\
&= k_{n+1,T-1} + e^*_{n,T} r_{n,T-1} \sec^2\theta_{1,n,T} \; .
\end{aligned}
\tag{A.72}
$$

The conjugate placed on the forward error in Equation (A.72) is due to the complex inner product defined in Equation

(A.19). This point is made due to the difference seen when comparing Equation (A.72) to that in Lee [22]. The covariance terms for the backward and forward errors can also be updated to form

$$R^e_{n,T} = R^e_{n,T-1} + e^*_{n,T} e_{n,T} \sec^2\theta_{1,n,T} \qquad (A.73)$$

and

$$R^r_{n,T} = R^r_{n,T-1} + r^*_{n,T} r_{n,T} \sec^2\theta_{0,n-1,T} \ . \qquad (A.74)$$

Sliding Exponential Windows

A window to reduce the effect of past data samples can be incorporated into the algorithm through the definition of the complex inner product. Referring to the complex inner product defined in Equation (A.19), a new inner product can be now be defined as

$$\langle x|y \rangle_T = \sum_{t=0}^{T} x^*_t \alpha^{T-t} y_t \qquad 0 < \alpha \le 1 \ . \qquad (A.75)$$

This definition of the complex inner product can be used to transform the time-update of the reflection coefficient in Equation (A.72) to

$$k_{n+1,T} = \alpha k_{n+1,T-1} + e^*_{n,T} r_{n,T-1} \sec^2\theta_{1,n,T} \ . \qquad (A.76)$$

The normalizations in the next section will eliminate the window α from every order of the lattice structure except the zeroth.

The Complex Unnormalized Recursive Least Squares Lattice Estimation Algorithm

Table A-I contains the necessary equations and initializations needed to implement the complex unnormalized recursive least squares lattice estimation algorithm. For notational purposes in Table A-I, let $\gamma_{n,T} = \cos^2\theta_{0,n-1,T}$. The resulting lattice structure is given in Figure A-2.

Normalized Ladder Recursions

In this section, a normalization of the recursive least squares lattice algorithm will be used to reduce the number of equations needed in for the time and order updates in Table A-I. The normalizations in this section will lead to a form of the algorithm which consists of a time-update for the reflection coefficient and an order-update for the backward and forward prediction errors.

Variance Normalization

In this section, the forward and backward prediction errors and the reflection coefficients will be normalized by the square root of their respective covariances. The normalized prediction errors are defined as

$$|\underline{v}_n\rangle_T \equiv |e_n\rangle_T \langle e_n|e_n\rangle_T^{-1/2} \qquad (A.77)$$

$$|\underline{n}_n\rangle_T \equiv |r_n\rangle_T \langle r_n|r_n\rangle_T^{-1/2} . \qquad (A.78)$$

The reflection coefficient is normalized in a similar manner and takes the form

TABLE A-I

Complex Least Squares Adaptive Lattice Algorithm

Input parameters:

N = maximum order of lattice

y_T = data sample at time T

α = exponential weighting factor

Do for T = 0 to T_{max}

$e_{0,T} = r_{0,T} = x_T$

$R^e_{0,T} = R^r_{0,T} = \alpha R^e_{0,T-1} + y_T y^*_T$

$\gamma_{0,T} = 1$

Do for n = 0 to $\{min(N,T)-1\}$

$k_{n+1,T} = \alpha k_{n+1,T-1} + e^*_{n,T} r_{n,T-1}/\gamma_{n,T-1}$

$\gamma_{n+1,T} = \gamma_{n,T} - r^*_{n,T} R^{-r}_{n,T} r_{n,T}$

$k^r_{n+1,T} = k_{n+1,T} R^{-r}_{n,T-1}$

$e_{n+1,T} = e_{n,T} - k^{*r}_{n+1,T} r_{n,T-1}$

$R^e_{n+1,T} = R^e_{n,T} - k^r_{n+1,T} k^*_{n+1,T}$

$k^e_{n+1,T} = R^{-e}_{n,T} k_{n+1,T}$

$r_{n+1,T} = r_{n,T-1} - k^e_{n+1,T} e_{n,T}$

$R^r_{n+1,T} = R^r_{n,T-1} - k^*_{n+1,T} k^e_{n+1,T}$

Note: Division by zero where $y = \gamma$, R^r, R^e, set $1/y = 0$.
Initialize the variables k, r, R^e, R^r, and γ to zero.

Figure A-2. Least squares adaptive lattice prediction error filter.

$$\Gamma_{n+1,T} = \langle \underline{v}_n | z^{-1} \underline{n}_n \rangle_T$$

$$= \langle e_n | e_n \rangle_T^{-1/2} k_{n+1,T} \langle z^{-1} r_n | z^{-1} r_n \rangle_T^{-1/2} \cdot \quad \text{(A.79)}$$

Having defined the normalizations in Equation (A.77), (A.78), and (A.79), a normalization of the order-updates for the backward and forward prediction errors can now be developed. A useful relationship involving the order-update of the forward prediction error covariance in Equation (A.41) will be needed to express the order-update in terms of the normalized variables defined in Equations (A.77), (A.78), and (A.79). Multiplying both sides of Equation (A.41) by $\langle e_n | e_n \rangle_T$ yields

$$\langle e_{n+1} | e_{n+1} \rangle_T \langle e_n | e_n \rangle_T = \langle e_n | e_n \rangle_T \langle e_n | e_n \rangle_T - \langle e_n | z^{-1} r_n \rangle_T$$

$$\langle e_n | e_n \rangle_T \langle z^{-1} r_n | z^{-1} r_n \rangle_T^{-1}$$

$$\langle z^{-1} r_n | e_n \rangle_T \quad \text{(A.80)}$$

or

$$\langle e_{n+1} | e_{n+1} \rangle_T \langle e_n | e_n \rangle_T = \langle e_n | e_n \rangle_T \langle e_n | e_n \rangle_T [1 - \langle e_n | e_n \rangle_T^{-1/2}$$

$$k_{n+1,T} \langle z^{-1} r_n | z^{-1} r_n \rangle_T^{-1/2}$$

$$\langle e_n | e_n \rangle_T^{-1/2} k^*_{n+1,T}$$

$$\langle z^{-1} r_n | z^{-1} r_n \rangle_T^{-1/2}] \cdot \quad \text{(A.81)}$$

Using the normalization of the reflection coefficients in Equation (A.79), Equation (A.81) can be written as

$$\langle e_{n+1} | e_{n+1} \rangle_T \langle e_n | e_n \rangle_T = \langle e_n | e_n \rangle_T \langle e_n | e_n \rangle_T$$

$$[1 - \Gamma^*_{n+1,T} \Gamma_{n+1,T}] \cdot \quad \text{(A.82)}$$

Dividing both sides of Equation (A.82) by $\langle e_n | e_n \rangle_T \langle e_n | e_n \rangle_T$

and taking the square root yields

$$\langle e_{n+1}|e_{n+1}\rangle_T^{1/2}\langle e_n|e_n\rangle_T^{-1/2} = [1 - \Gamma^*_{n+1,T}\Gamma_{n+1,T}]^{1/2} .$$

<div align="right">(A.83)</div>

Taking the order-update of the forward prediction error in Equation (A.40) and dividing both sides by $\langle e_{n+1}|e_{n+1}\rangle_T^{1/2}$ yields

$$|e_{n+1}\rangle_T\langle e_{n+1}|e_{n+1}\rangle_T^{-1/2} = \langle e_{n+1}|e_{n+1}\rangle_T^{-1/2}\langle e_n|e_n\rangle_T^{1/2}$$
$$[|e_n\rangle_T\langle e_n|e_n\rangle_T^{-1/2} -$$
$$|z^{-1}r_n\rangle_T\langle z^{-1}r_n|z^{-1}r_n\rangle_T^{-1}$$
$$k^*_{n+1,T}\langle e_n|e_n\rangle_T^{-1/2}] .$$

<div align="right">(A.84)</div>

Using the normalizations defined previously and Equation (A.83), Equation (A.84) takes the form

$$|\underline{v}_{n+1}\rangle_T = [|\underline{v}_n\rangle_T - |z^{-1}\underline{n}_n\rangle_T\Gamma^*_{n+1,T}]$$
$$[1- \Gamma^*_{n+1,T}\Gamma_{n+1,T}]^{-1/2}$$

<div align="right">(A.85)</div>

The same type of normalization applies to the order-update for the backward error which can be written as

$$|\underline{n}_{n+1}\rangle_T = [|z^{-1}\underline{n}_n\rangle_T - |\underline{v}_n\rangle_T\Gamma_{n+1,T}] [1- \Gamma^*_{n+1,T}\Gamma_{n+1,T}]^{-1/2}$$

<div align="right">(A.86)</div>

Angle Normalization

The next normalization is defined as

$$|v_n\rangle_T = |\underline{v}_n\rangle_T\sec\theta_{1,n,T}$$

<div align="right">(A.87)</div>

and

$$|z^{-1}\eta_n\rangle_T = |z^{-1}\underline{\eta}_n\rangle_T \sec\theta_{1,n,T} \; . \tag{A.88}$$

This normalization defines the forward and backward prediction errors in terms that are no longer observable, but the definition of the reflection coefficients will remain unchanged.

At this point, a useful relationship, needed in the normalization of the time-update of the reflection coefficients, will be developed. Applying the inner product defined in Equation (A.75), the time-update for the forward prediction error covariance in Equation (A.73) takes the form

$$\alpha\langle e_n|e_n\rangle_{T-1} = \langle e_n|e_n\rangle_T - \langle e_n|\underline{\eta}\rangle_T\langle\underline{\eta}|e_n\rangle_T\sec^2\theta_{1,n,T} \; . \tag{A.89}$$

Factoring $\langle e_n|e_n\rangle_T$ from the right hand side of Equation (A.89) yields

$$\alpha\langle e_n|e_n\rangle_{T-1} = \langle e_n|e_n\rangle_T[1 - \langle e_n|e_n\rangle_T^{-1}$$
$$\langle e_n|\underline{\eta}\rangle_T\langle\underline{\eta}|e_n\rangle_T\sec^2\theta_{1,n,T}] \; . \tag{A.90}$$

Dividing both sides of Equation (A.90) by $\langle e_n|e_n\rangle_T$ and grouping terms gives

$$\alpha\langle e_n|e_n\rangle_{T-1}\langle e_n|e_n\rangle_T^{-1} = 1 - \langle e_n|e_n\rangle_T^{-1/2}e^*_{n,T}\sec\theta_{1,n,T}$$
$$\langle e_n|e_n\rangle_T^{-1/2}e_{n,T}\sec\theta_{1,n,T} \; . \tag{A.91}$$

Using the normalization defined in Equation (A.87), Equation (A.91) takes the form

$$\alpha \langle e_n | e_n \rangle_{T-1} \langle e_n | e_n \rangle_T^{-1} = [1 - v^*_{n,T} v_{n,T}] \ . \qquad \text{(A.92)}$$

Finally, dividing by α and taking the square root of Equation (A.92) yields

$$\langle e_n | e_n \rangle_{T-1}^{1/2} \langle e_n | e_n \rangle_T^{-1/2} = \alpha^{-1/2} [1 - v^*_{n,T} v_{n,T}]^{1/2} \ .$$

$$\text{(A.93)}$$

Using the time-update for the backward prediction error covariance in Equation (A.74), a similar development yields

$$\langle z^{-1} r_n | z^{-1} r_n \rangle_{T-1}^{1/2} \langle z^{-1} r_n | z^{-1} r_n \rangle_T^{-1/2}$$
$$= \alpha^{-1/2} [1 - \langle z^{-1} \eta_n | \eta \rangle_T \langle \eta | z^{-1} \eta_n \rangle_T]^{1/2} \ . \qquad \text{(A.94)}$$

Using the time-update for the reflection coefficient in Equation (A.76) and the normalization in Equation (A.79), the normalized time-update of the reflection coefficient can be written as

$$\Gamma_{n+1,T} = \langle e_n | e_n \rangle_T^{-1/2} \langle e_n | e_n \rangle_{T-1}^{1/2} \langle e_n | e_n \rangle_{T-1}^{-1/2}$$
$$\alpha k_{n+1,T-1} \langle z^{-1} r_n | z^{-1} r_n \rangle_{T-1}^{-1/2}$$
$$\langle z^{-1} r_n | z^{-1} r_n \rangle_{T-1}^{1/2} \langle z^{-1} r_n | z^{-1} r_n \rangle_T^{-1/2} +$$
$$\langle e_n | e_n \rangle_T^{-1/2} \langle e_n | \eta \rangle_T \sec\theta_{1,n,T}$$
$$\langle z^{-1} r_n | z^{-1} r_n \rangle_T^{-1/2} \langle \eta | z^{-1} r_n \rangle_T \sec\theta_{1,n,T} \ . \qquad \text{(A.95)}$$

Equation (A.95) can now be written in terms of normalized variables as

$$\Gamma_{n+1,T} = [1 - v^*_{n,T}v_{n,T}]^{1/2}\Gamma_{n+1,T-1}$$
$$[1-\eta^*_{n,T-1}\eta_{n,T-1}]^{1/2} + v^*_{n,T}\eta_{n,T-1} \qquad (A.96)$$

using Equations (A.77), (A.78), (A.79), (A.87), (A.93), and (A.94).

Ladder Recursions

At this point, a second normalization of the order-updates for the forward and backward prediction errors is possible. This normalization is based on the terms defined in Equations (A.87) and (A.88). Equation (A.85), the normalized order-update for the forward prediction, can be normalized in the manner given in Equation (A.87). Equation (A.66) can be written as

$$|\underline{v}_{n+1}\rangle_T \sec\theta_{1,n+1,T}/\sec\theta_{1,n+1,T} = \sec\theta_{1,n,T}/\sec\theta_{1,n,T}$$
$$[|\underline{v}_n\rangle_T - |z^{-1}\underline{\eta}_n\rangle_T$$
$$\Gamma^*_{n+1,T}] [1 - \Gamma^*_{n+1,T}$$
$$\Gamma_{n+1,T}]^{-1/2} . \qquad (A.97)$$

Using the normalizations in Equations (A.87) and (A.88), Equation (A.97) takes the form

$$|v_{n+1}\rangle_T \sec\theta_{1,n,T}/\sec\theta_{1,n+1,T} = [|v_n\rangle_T - |z^{-1}\eta_n\rangle_T\Gamma^*_{n+1,T}]$$
$$[1-\Gamma^*_{n+1,T}\Gamma_{n+1,T}]^{-1/2} .$$

$$(A.98)$$

In order to complete the normalization, a relationship between $\sec\theta_{1,n,T}/\sec\theta_{1,n+1,T}$ and the normalized variables must be developed. Writing the order-update for $\cos^2\theta_{1,n,T}$ in Equation (A.68) as

$$\cos^2\theta_{1,n+1,T}/\cos^2\theta_{1,n,T} = [1 - r^*_{n,T-1}\cos^{-1}\theta_{1,n,T}$$
$$R^{-r}_{n,T-1}r_{n,T-1}\cos^{-1}\theta_{1,n,T}]$$

(A.99)

will lead to the desired relationship. The trigonometric relationship

$$\sec^2\theta_{1,n,T} = 1/\cos^2\theta_{1,n,T} \qquad \text{(A.100)}$$

is stated here as a reminder. Using the relationship stated in Equation (A.100) and the normalizations given in Equations (A.77), (A.78), and (A.87), Equation (A.99) takes the form

$$\sec^2\theta_{1,n,T}/\sec^2\theta_{1,n+1,T} = [1 - \eta^*_{n,T-1}\eta_{n,T-1}] \; . \quad \text{(A.101)}$$

Using the relationship given in Equation (A.101), the normalized order-update of the forward prediction error in Equation (A.98) can be written as

$$v_{n+1,T} = [1 - \Gamma^*_{n+1,T}\Gamma_{n+1,T}]^{-1/2}[v_{n,T} - \Gamma^*_{n+1,T}\eta_{n,T-1}]$$
$$[1 - \eta^*_{n,T-1}\eta_{n,T-1}]^{-1/2} \qquad \text{(A.102)}$$

while looking only at the Tth component. A similar development leads to the normalized order-update of the backward prediction error which can be written as

$$\eta_{n+1,T} = [1 - \Gamma^*_{n+1,T}\Gamma_{n+1,T}]^{-1/2}[\eta_{n,T-1} - \Gamma_{n+1,T}v_{n,T}]$$

$$[1 - v^*_{n,T}v_{n,T}]^{-1/2} . \qquad\qquad (A.103)$$

The Complex Normalized Recursive Least Squares Lattice Estimation Algorithm

The order-updates for the backward and forward prediction error covariances and for the trigonometric relationship $\cos^2\theta$ have been embedded in the normalizations defined in this section. A reduction in the number of equations, from six to three, required in the lattice recursions has been achieved. Table A-II gives the complex square root normalized recursive least squares lattice estimation including the necessary initializations, and Figure A-3 gives the resulting lattice structure.

Complex Prediction Error Filter Coefficients

Introduction

An algorithm for determining the coefficients of the prediction error filter is given by Honig [18] as a lattice structure implementation for the real data case. The complex form of this algorithm is presented in this section to support the complex square root normalized recursive least square lattice estimation algorithm. A transfer function relationship will be defined for the forward and backward prediction errors which can then be implemented as a lattice structure. The coefficients of the filter can then be obtained from the transfer function.

TABLE A-II

Complex Square Root Normalized Recursive Least
Squares Lattice Estimation Algorithm

Initialize:

$R_{-1} = \sigma$ σ is a small positive value

for $T = 0, T_{max}$

$R_T = \alpha R_{T-1} + y^*_T y_T$

$v_{0,T} = \eta_{0,T} = y_T (R_T)^{-1/2}$

for $n = 0$ to $[\min\{T,N\} - 1]$

$\Gamma_{n+1,T} = [1 - v^*_{n,T} v_{n,T}]^{1/2} \, \Gamma_{n+1,T-1}$

$\qquad\qquad [1 - \eta^*_{n,T-1} \eta_{n,T-1}]^{1/2} + v^*_{n,T} \eta_{n,T-1}$

$v_{n+1,T} = [1 - \Gamma^*_{n+1,T} \Gamma_{n+1,T}]^{-1/2} [v_{n,T} - \Gamma^*_{n+1,T} \eta_{n,T-1}]$

$\qquad\qquad [1 - \eta^*_{n,T-1} \eta_{n,T-1}]^{-1/2}$

$\eta_{n+1,T} = [1 - \Gamma^*_{n+1,T} \Gamma_{n+1,T}]^{-1/2} [\eta_{n,T-1} - \Gamma_{n+1,T} v_{n,T}]$

$\qquad\qquad [1 - v^*_{n,T} v_{n,T}]^{-1/2}$

Note: Division by zero where $y = 1/x$: $x = 0$ should result in
$y = 0$. Initialize the variables Γ, v, and η to zero.

Figure A-3. Complex square root normalized least squares adaptive lattice prediction error filter.

Transfer Functions

The nth order forward prediction error, at time T, can be written as

$$e_{n,T} = x_T + a_{n,1,T} x_{T-1} + \ldots + a_{n,n,T} x_{T-n} . \qquad \text{(A.104)}$$

Taking the Z-transform of this forward prediction error and dividing through by $x(z)$, the transfer function can be defined as

$$A_{n,T}(z) = 1 + a_{n,1,T} z^{-1} + \ldots + a_{n,n,T} z^{-n} . \qquad \text{(A.105)}$$

$A_{n,T}(z)$ can be written in vector form as

$$A_{n,T}(z) = 1 + A'_{n,T} z^{-1} \underline{z}_n \qquad \text{(A.106)}$$

where

$$A_{n,T} = [\, a_{n,1,T} \cdots a_{n,n,T} \,]'$$

and

$$\underline{z}_n = [\, 1 \ z^{-1} \ \ldots \ z^{-n+1}]' .$$

Similarly, the nth order backward prediction error, at time T, can be written as

$$r_{n,T} = x_{T-n} + b_{n,0,T} x_T + \ldots + b_{n,n-1,T} x_{T-n+1} \qquad \text{(A.107)}$$

where the transfer function for this filter is

$$B_{n,T}(z) = z^{-n} + b_{n,0,T} + \ldots + b_{n,n-1,T} z^{-n+1} . \qquad \text{(A.108)}$$

The vector form of $B_{n,T}(z)$ can be written as

$$B_{n,T}(z) = z^{-n} + B'_{n,T}z_n \qquad (A.109)$$

where

$$B_{n,T} = [\; b_{n,0,T} \cdots b_{n,n-1,T} \;]' \; .$$

A version of the backward prediction error based on estimating x_{T-n} using the coefficients obtained at time $T-1$ will be needed in the order updates of the transfer functions and can be written as

$$r_{n,T}|_{T-1} = x_{T-n} + b_{n,0,T-1}x_T$$
$$+ \cdots + b_{n,n-1,T-1}x_{T-n-1} \qquad (A.110)$$

and the associated transfer function as

$$B_{n,T-1}(z) = [z^{-n} + B'_{n,T-1}z_n] \qquad (A.111)$$

where

$$B_{n,T-1} = [\; b_{n,0,T-1} \cdots b_{n,n-1,T-1} \;]' \; .$$

An order update for the forward and backward prediction errors is given in Equations (A.40) and (A.44), respectively. The transfer functions for the forward error order update, $e_{n+1,T}$, and the backward error order update, $r_{n+1,T}$, can be written as

$$A_{n+1,T}(z) = A_{n,T}(z) - z^{-1}B_{n,T-1}(z)R^{-r}_{n,T-1}k^*_{n+1,T}$$
$$(A.112)$$

and

$$B_{n+1,T}(z) = z^{-1}B_{n,T-1}(z) - A_{n,T}(z)R^{-e}_{n,T}k_{n+1,T} \qquad (A.113)$$

respectively.

In order to implement the transfer functions in terms of a lattice structure, a relationship between $B_{n,T}(z)$ and $B_{n,T-1}(z)$ needs to be developed. The time-update formula given in Equation (A.57) can be used to form the time-update

$$P^{\perp}_{0,n-1,T} = P_{-}^{\perp}_{0,n-1,T} - P_{0,n-1,T}P_T P_{-}^{\perp}_{0,n-1,T} \qquad (A.114)$$

where $P_{-}^{\perp}_{0,n-1,T}$ is the orthogonal oblique projection operator. Using Equation (A.70), Equation (A.114) can be written as

$$P^{\perp}_{0,n-1,T} = P_{-}^{\perp}_{0,n-1,T} -$$
$$P_{0,n-1,T}P_T P^{\perp}_{0,n-1,T}\sec^2\theta_{0,n-1,T} \ . \qquad (A.115)$$

The backward prediction error at time T, $r_{n+1,T}$, can be obtained by pre and post multiplying Equation (A.115) by $_T\langle\pi|$ and $|z^{-n}x\rangle_T$, respectively, to form

$$_T\langle\pi| P^{\perp}_{0,n-1,T}| z^{-n}x\rangle_T = \ _T\langle\pi| P^{\perp}_{0,n-1,T-1}| z^{-n}x\rangle_T -$$
$$_T\langle\pi| P_{0,n-1,T}P_T P^{\perp}_{0,n-1,T} |z^{-n}x\rangle_T$$
$$\sec^2\theta_{0,n-1,T} \ . \qquad (A.116)$$

From Equation (A.30), the term on the left hand side of the equals sign in Equation (A.116) is the backward prediction error at time T. The first term on the left hand side of the equals sign represents the estimate of the backward prediction error at time T using the coefficients defined at

time T-1. The second term on the right side of Equation (A.116) is not so apparent. The second term can be written as

$$_T\langle\pi|P_{0,n-1,T}P_TP^\perp_{0,n-1,T}|z^{-n}x\rangle_T \sec^2\theta_{0,n-1,T}$$
$$= {}_T\langle\pi|P_{0,n-1,T}|\pi\rangle_T\langle\pi|^*_TP^\perp_{0,n-1,T}|z^{-n}x\rangle_T$$
$$\sec^2\theta_{0,n-1,T}. \tag{A.117}$$

From Equation (A.30), Equation (A.117) can be written as

$$_T\langle\pi|P_{0,n-1,T}P_TP^\perp_{0,n-1,T}|z^{-n}x\rangle_T\sec^2\theta_{0,n-1,T}$$
$$= {}_T\langle\pi|P_{0,n-1,T}|\pi\rangle_T r_{n,T}\sec^2\theta_{0,n-1,T}. \tag{A.118}$$

The projection of $|\pi\rangle_T$ on to the subspace $X_{0,n-1,T}$ in Equation (A.118) can be written as

$$_T\langle\pi|P_{0,n-1,T}|\pi\rangle_T = {}_T\langle\pi||X_{0,n-1}\rangle_T\langle X_{0,n-1}|X_{0,n-1}\rangle_T^{-1}$$
$$\langle X_{0,n-1}|^*_T|\pi\rangle_T . \tag{A.119}$$

Using the least squares estimate defined in Equation (A.11), Equation (A.119) can be written as

$$_T\langle\pi|P_{0,n-1,T}|\pi\rangle_T = {}_T\langle\pi||X_{0,n-1}\rangle_T C_{n,T} \tag{A.120}$$

where

$$C_{n,T} = [c_{n,0,T} \cdots c_{n,n-1,T}]' .$$

Equation (A.118) can now be written as

$$_T\langle\pi|P_{0,n-1,T}|\pi\rangle_T r_{n,T}\sec^2\theta_{0,n-1,T} = {}_T\langle\pi||X_{0,n-1}\rangle_T C_{n,T}$$
$$r_{n,T}\sec^2\theta_{0,n-1,T} \ .$$

$$(A.121)$$

Taking the z-transform of Equation (A.121) and dividing through by x(z) yields

$$C_{n,T}(z) = c_{n,0} + c_{n,1}z^{-1} + \ldots + c_{n,n-1}z^{-n+1}$$
$$= C'_{n,T}\underline{z}_{n-1} \ . \qquad\qquad (A.122)$$

The z-transform of Equation (A.116) divided by x(z) can now be written as

$$B_{n,T}(z) = B_{n,T-1}(z) - C_{n,T}(z)r_{n,T}/\gamma_{n,T} \qquad (A.123)$$

where

$$\gamma_{n,T} = \cos^2\theta_{0,n-1,T} \ .$$

An order-update of $C_{n,T}(z)$ is needed to implement the lattice structure. Using the concept of the decomposition of subspaces defined in Equation (A.33), the projection operator $P_{0,n,T}$ can be written as

$$P_{0,n,T} = P_{0,n-1,T} + |r_n\rangle_T\langle r_n|r_n\rangle_T^{-1}\langle r_n|_T^* \ . \qquad (A.124)$$

Pre and post multiplying Equation (A.124) by $_T\langle\pi|$ and $|\pi\rangle_T$, respectively, yields

$$_T\langle\pi|P_{0,n,T}|\pi\rangle_T = {}_T\langle\pi|P_{0,n-1,T}|\pi\rangle_T +$$
$$_T\langle\pi||r_n\rangle_T\langle r_n|r_n\rangle_T^{-1}\langle r_n|_T^*|\pi\rangle_T \ . \quad (A.125)$$

Using the transfer functions defined in Equations (A.108) and

(A.122), the transfer function associated with Equation (A.125) can be written as

$$C_{n+1,T}(z) = C_{n,T}(z) + B_{n,T}(z)R^{-r}_{n,T}r^{*}_{n,T} . \qquad (A.126)$$

Unnormalized Prediction Error
Filter Coefficients

The coefficients of the prediction error filter can be obtained from the lattice implementation of the transfer functions by associating terms in the transfer functions that are multiplied by the same power of the variable z^{-p} $p = 0,\ldots,n$. Table A-III gives the algorithm for the lattice implementation of the coefficients associated with the prediction error filter, and Figure A-4 gives the associated lattice structure.

Normalized Transfer Functions

A normalized lattice structure implementation of the transfer functions which involves the normalized forward and backward prediction errors and the normalized reflection coefficient defined for normalized lattice structure given in the previous section will be developed. The normalized transfer functions will be defined as

$$A_{n,T}(z) = A_{n,T}(z) \langle e_n | e_n \rangle_T^{-1/2} \qquad (A.127)$$

$$B_{n,T}(z) = B_{n,T}(z) \langle r_n | r_n \rangle_T^{-1/2} \qquad (A.128)$$

$$B_{n,T-1}(z) = B_{n,T-1}(z) \langle r_n | r_n \rangle_{T-1}^{-1/2} \qquad (A.129)$$

and

TABLE A-III

Algorithm for Determining the AR Model Coefficeints
Based on a Complex LS Adaptive Lattice Structure

For $i = 0, \ldots, N$ do the following

$b_{p,-1,T} = 0$ for $p = 0, \ldots, N-1$

$a_{0,0,T} = b_{0,0,T} = 1$ for $i = 0$

$c_{0,0,T} = 0$ for $i = 0$

$a_{0,i,T} = b_{0,i,T} = c_{0,i,T} = 0$ for $i > 0$

For $p = 0, \ldots, N-1$

$b_{p,i,T-1} = b_{p,i,T} + c_{p,i,T} r_{p,T} / \gamma_{p,T}$

$c_{p+1,i,T} = c_{p,i,T} + b_{p,i,T} R^{-r}_{p,T} r^{*}_{p,T}$

$a_{p+1,i,T} = a_{p,i,T} - b_{p,i-1,T-1} R^{-r}_{p,T-1} k^{*}_{p+1,T}$

$b_{p+1,i,T} = b_{p,i-1,T-1} - a_{p,i,T} R^{-e}_{p,T} k_{p+1,T}$
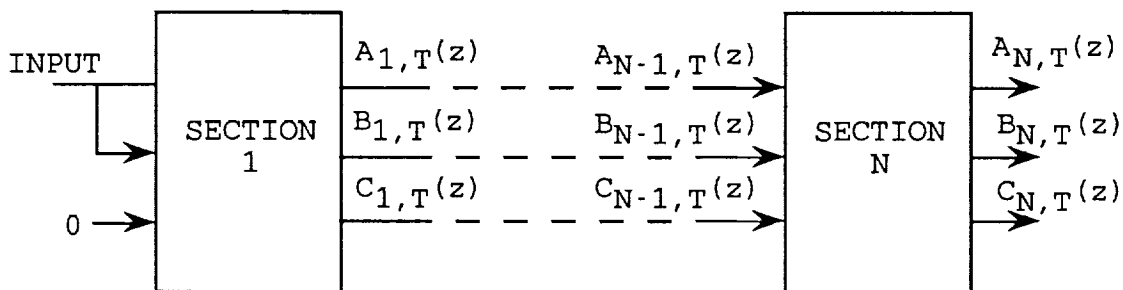
(a) The overall structure.
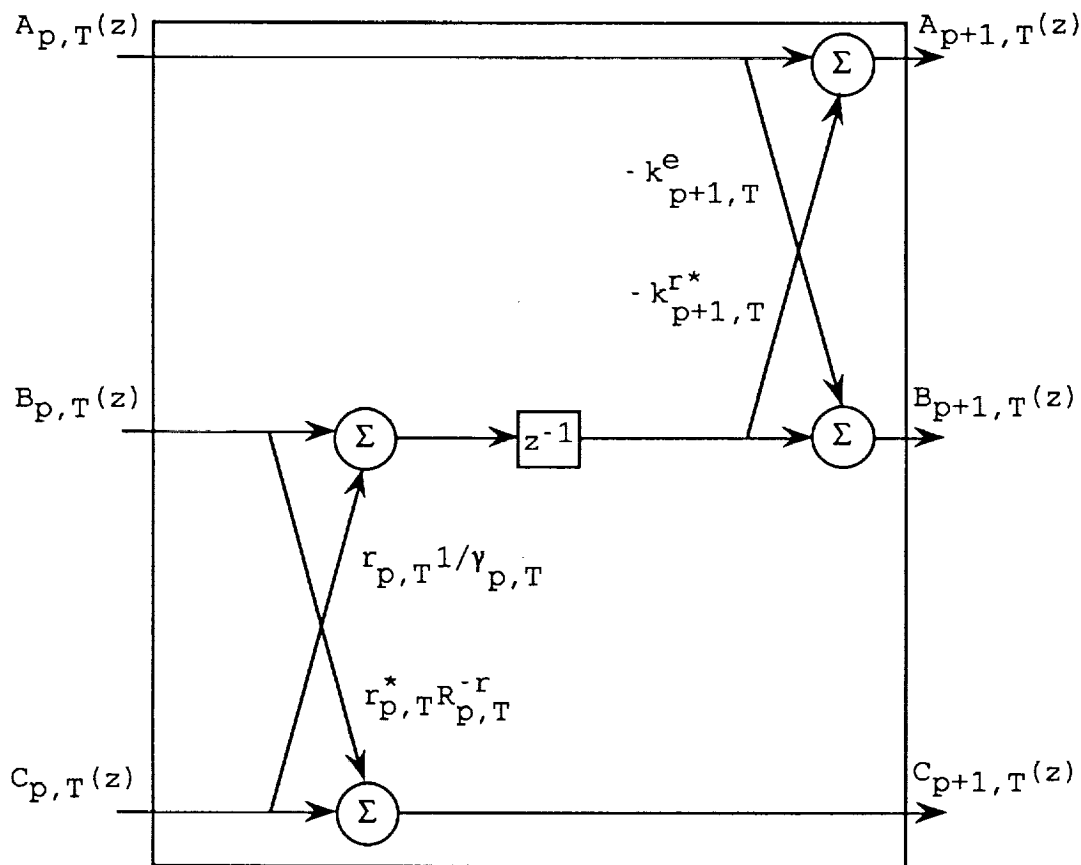
(b) A single section.

Figure A-4. Transfer function implemented as a lattice structure for the least squares adaptive prediction error filter case.

$$C_{n,T}(z) = C_{n,T}(z)\sec\theta_{0,n-1,T} \quad . \tag{A.130}$$

Based on Equations (A.127), (A.129), (A.79), and (A.82), Equation (A.112) can be normalized as

$$A_{n+1,T}(z) = [A_{n,T}(z) - z^{-1}B_{n,T-1}(z)\Gamma^*_{n+1,T}]$$
$$[1-\Gamma^*_{n+1,T}\Gamma_{n+1,T}]^{-1/2} \quad . \tag{A.131}$$

A similar normalization holds for Equations (A.113) and where

$$B_{n+1,T}(z) = [z^{-1}B_{n,T-1}(z) - A_{n,T}(z)\Gamma_{n+1,T}]$$
$$[1-\Gamma^*_{n+1,T}\Gamma_{n+1,T}]^{-1/2} \quad . \tag{A.132}$$

Using the previously defined normalizations and Equation (A.94) with the time index T replaced with T+1, Equation (A.123) can be normalized as

$$B_{n,T-1}(z) = [B_{n,T}(z) + C_{n,T}(z)\eta_{n,T}]$$
$$[1-\eta^*_{n,T}\eta_{n,T}]^{-1/2}. \tag{A.133}$$

The final normalization requires the relationship

$$\sec^2\theta_{0,n-1,T}/\sec^2\theta_{0,n,T} = [1 - \eta^*_{n,T}\eta_{n,T}] \tag{A.134}$$

to form the normalized transfer function

$$C_{n+1,T}(z) = [C_{n,T}(z) + B_{n,T}(z)\eta^*_{n,T}]$$
$$[1-\eta^*_{n,T}\eta_{n,T}]^{-1/2} \quad . \tag{A.135}$$

The coefficients of the prediction error filter can be obtained from the normalized lattice implementation of the transfer functions in a similar manner as that used for the

unnormalized case. Table A-IV gives the algorithm for obtaining the filter coefficients from the normalized lattice structure and Figure A-5 gives the associated lattice structure.

TABLE A-IV

Algorithm for Determining the AR Model Coefficients Based
on a Normalized Complex LS Adaptive Lattice Structure

$R_T = \alpha R_{T-1} + x^*_T x_T$

For $i = 0, \ldots, N$ do the following

$b_{p,-1,T} = 0$ for $p = 0, \ldots, N-1$

$a_{0,0,T} = b_{0,0,T} = R_T^{-1/2}$ for $i = 0$

$c_{0,0,T} = 0$ for $i = 0$

$a_{0,i,T} = b_{0,i,T} = c_{0,i,T} = 0$ for $i > 0$

For $p = 0, \ldots, N-1$

$b_{p,i,T-1} = [b_{p,i,T} + c_{p,i,T}\eta_{p,T}]$
$$[1-\eta^*_{p,T}\eta_{p,T}]^{-1/2}$$

$c_{p+1,i,T} = [c_{p,i,T} + b_{p,i,T}\eta^*_{p,T}] [1-\eta^*_{p,T}\eta_{p,T}]^{-1/2}$

$a_{p+1,i,T} = [a_{p,i,T} - b_{p,i-1,T-1}\Gamma^*_{p+1,T}]$
$$[1-\Gamma^*_{p+1,T}\Gamma_{p+1,T}]^{-1/2}$$

$b_{p+1,i,T} = [b_{p,i-1,T-1} - a_{p,i,T}\Gamma_{p+1,T}]$
$$[1-\Gamma^*_{p+1,T}\Gamma_{p+1,T}]^{-1/2}$$

where

$a_{p,i} = a_{p,i}/a_{p,0}$

(a) The overall structure.

$$x^c = [1 - x^*x]^{-1/2}$$
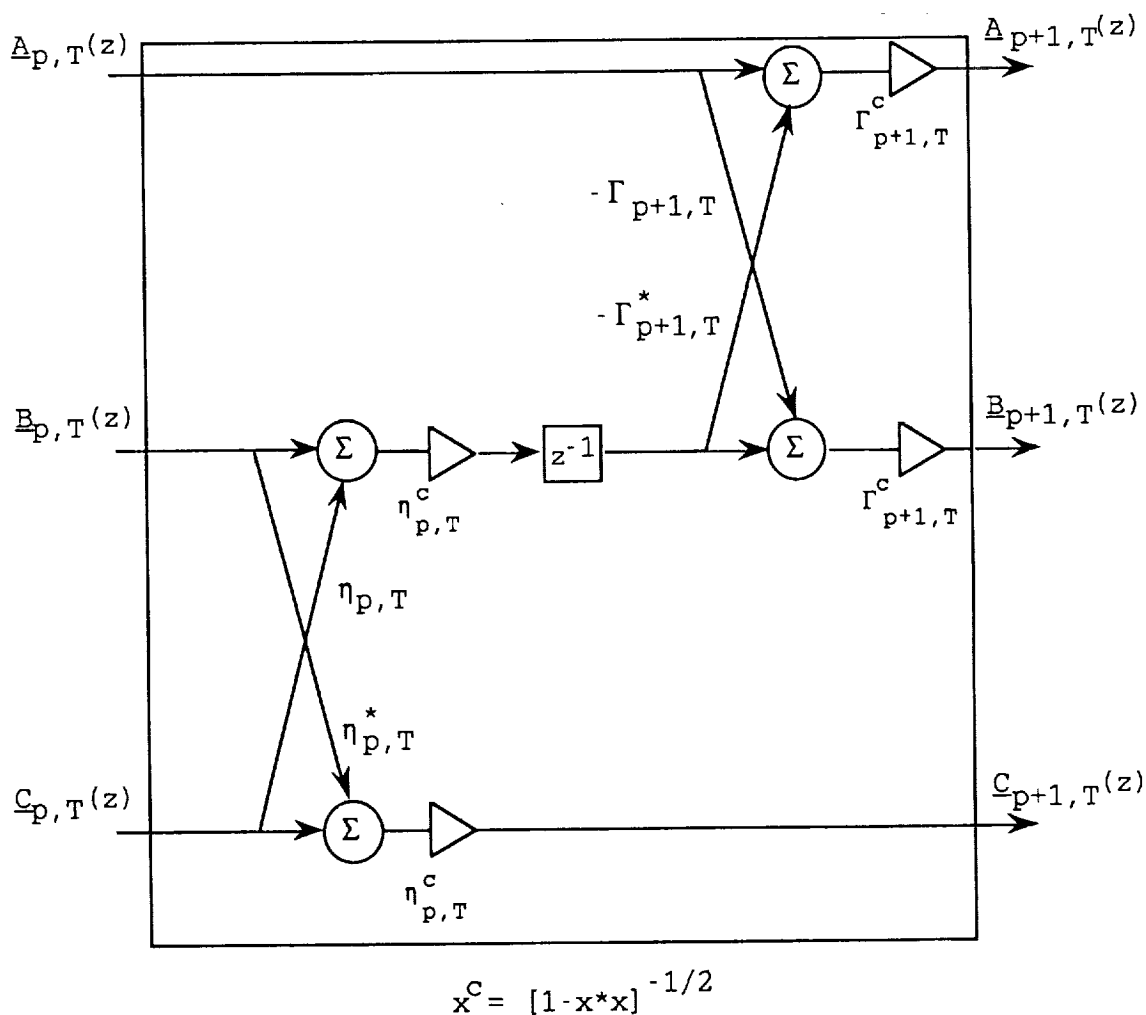
(b) A single section.

Figure A-5. Transfer function implemented as a lattice structure for the complex square root normalized least squares adaptive prediction error filter case.

Appendix B

NASA Model Parameters

SIMULATION PARAMETERS

A/C Distance to touchdown (kM)	7.0
Aircraft Velocity (kts)	150.0
Glideslope Angle (deg)	3.0
Roll Attitude (deg)	0.0
Pitch Attitude (deg)	0.0
Yaw Attitude (deg)	0.0
Az Integration Range/2 (deg)	6.0
Az Integration Increment (deg)	0.3
El Integration Range/2 (deg)	4.0
El Integration Increment (deg)	0.2
Rng Integration Increment (m)	100.0
Random Number Seed (0-1)	0.224

MICROBURST & CLUTTER

Along Track Offset from TD (km)	-2.0
Cross Track Offset from TD (km)	0.0
Rain Standard Deviation (m/s)	1.0
Clutter Standard Deviation (m/s)	0.5
Clutter Calc. Flag	(1=on, 0=off)
Reflectivity Calc. Thres. (dBz)	1.0 (wet)
	-20.0 (dry)
	200.0 (clutter)
Minimum Reflectivity (dBz)	-15.0
Attenuation Code (0,1,2)	2.0

RADAR PARAMETERS

Initial Radar Range (km)	1.0
Number of Range Cells	40.0
Antenna Az - if no scan (deg)	0.0
Azimuth Scan Range/2 (deg)	0.0
Azimuth Scan Increment (deg)	3.0
Antenna Elevation (deg)	1.0
Transmitted Power (watts)	2000.0
Frequency (GHz)	9.3
Pulse Width (microsecs)	1.0
Pulse Interval (microsecs)	268.6
Receiver Noise Figure (dB)	4.0
Receiver Losses (dB)	3.0
Antenna Type (1=para., 2=flat)	1.0

Appendix C

Fourier Spectral Estimates of a Dry
Microburst Plus Clutter

Range Cell 10, Range Cell 11, Range Cell 12, Range Cell 13, Range Cell 14, Range Cell 15, Range Cell 16, Range Cell 17, Range Cell 18 (dB vs meters/sec plots)

Range Cell 37

Range Cell 38

Range Cell 39

Range Cell 40
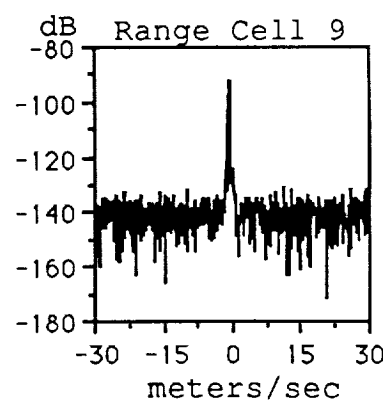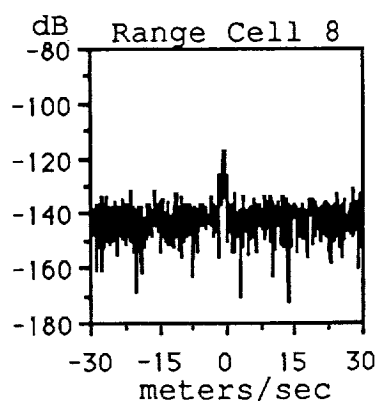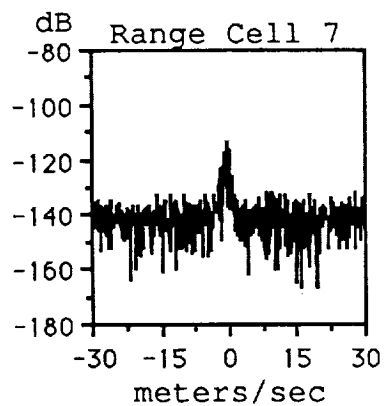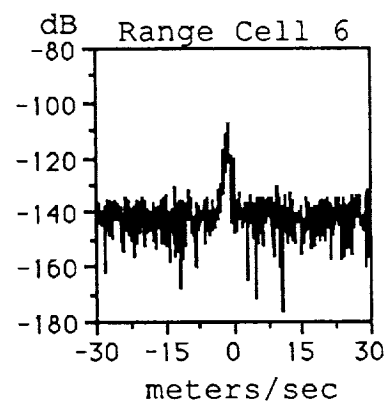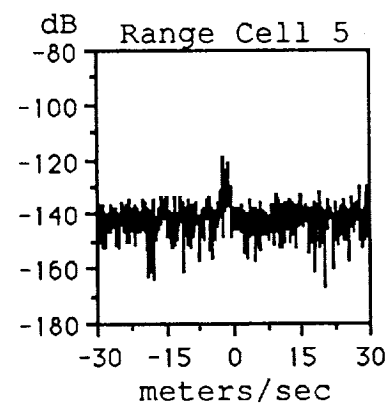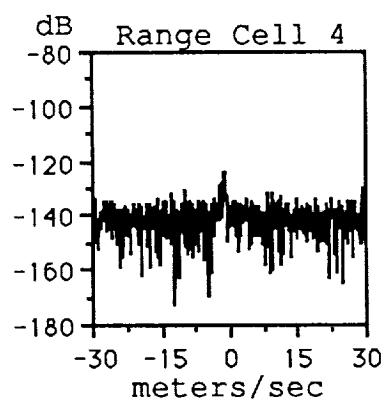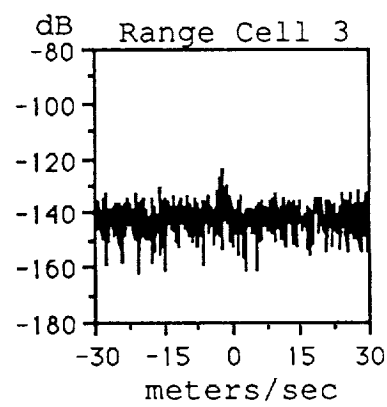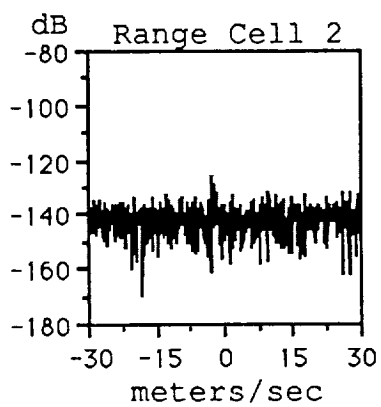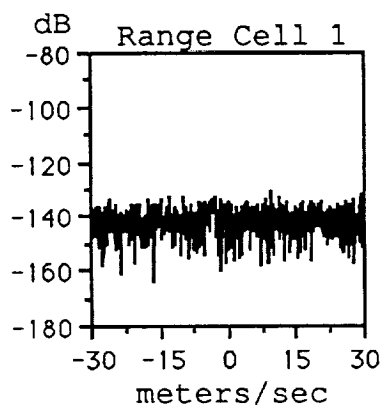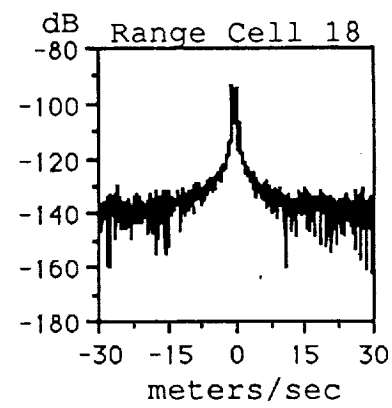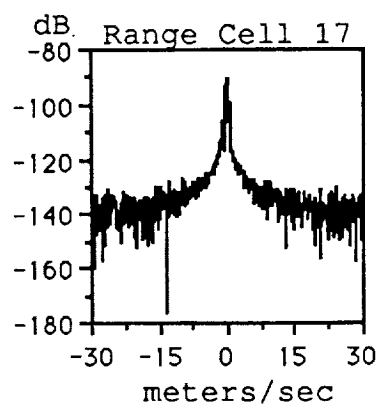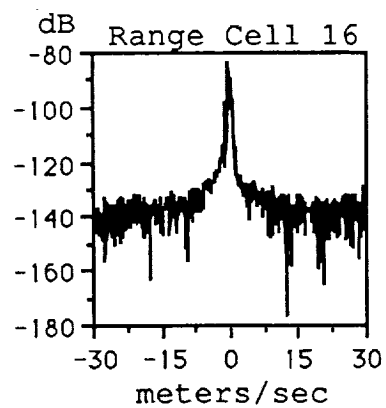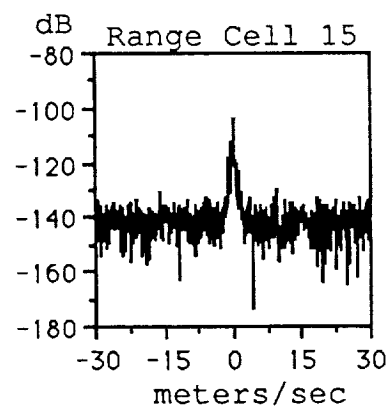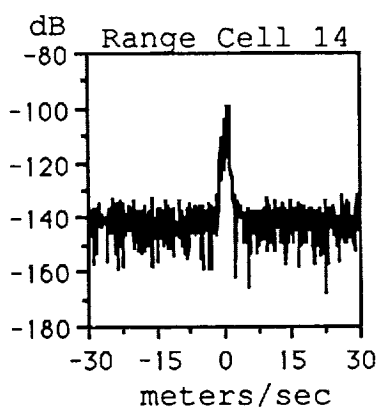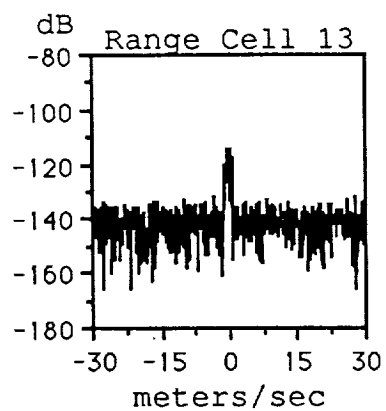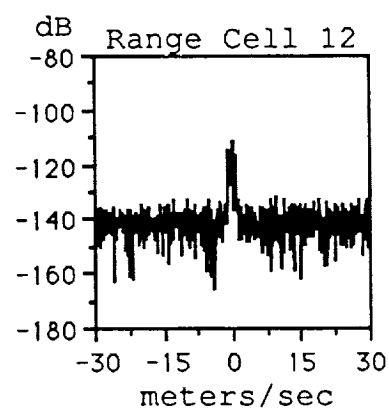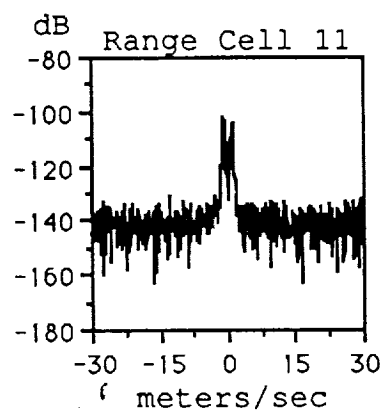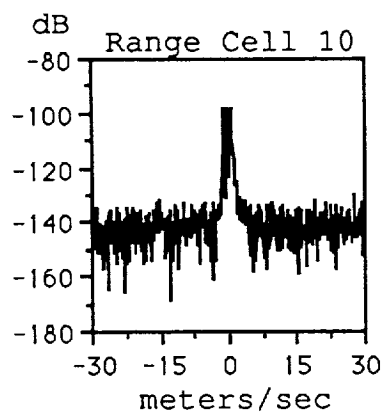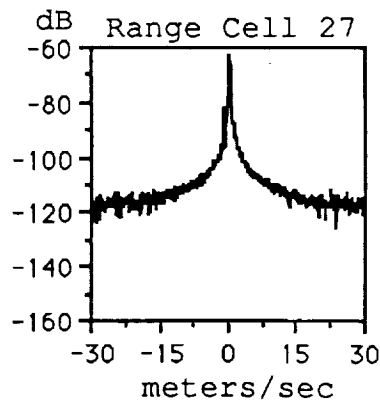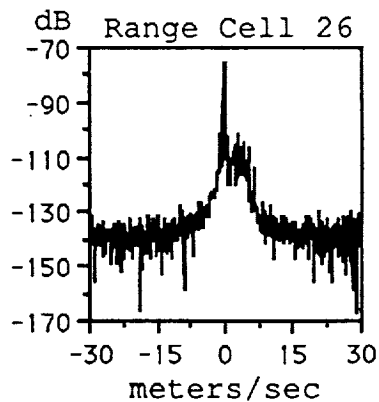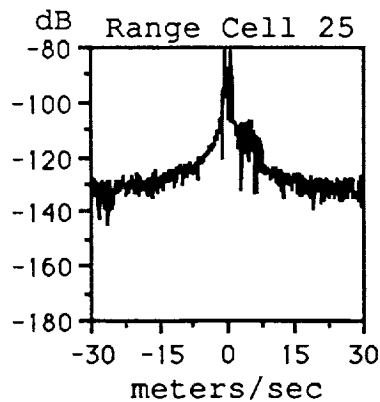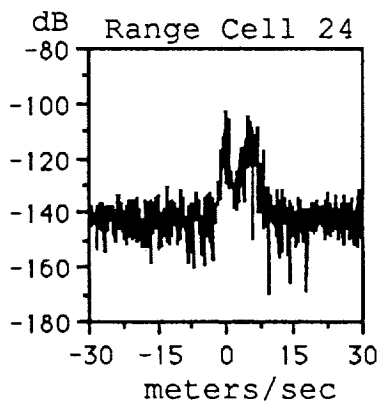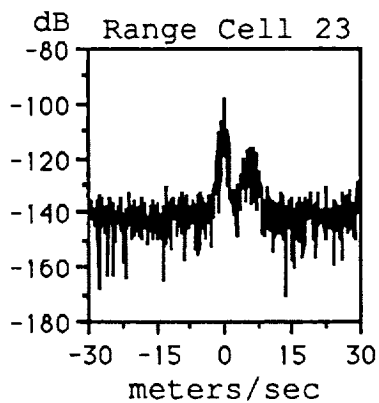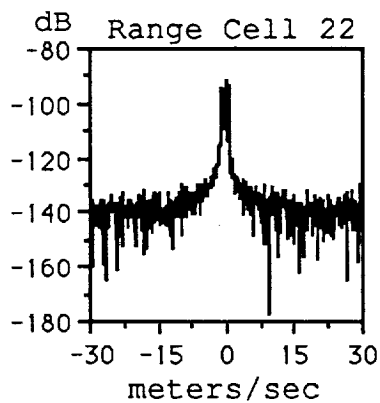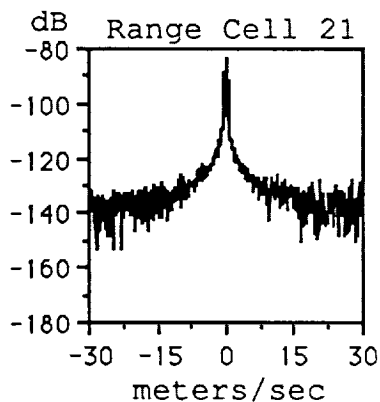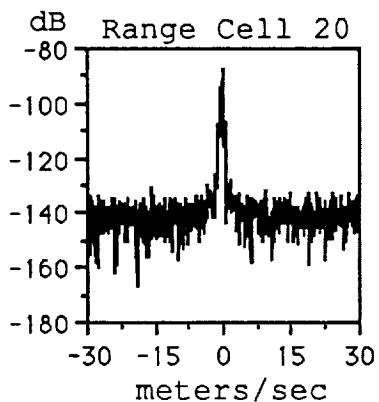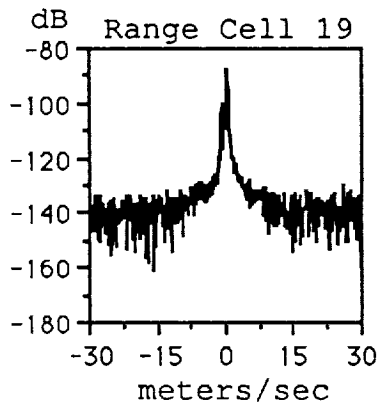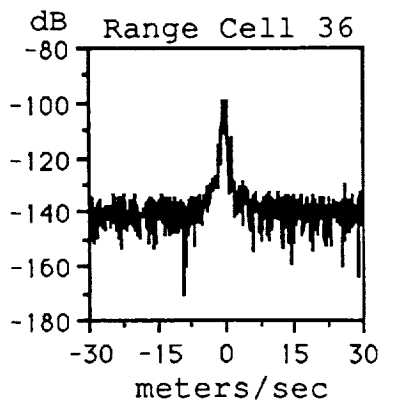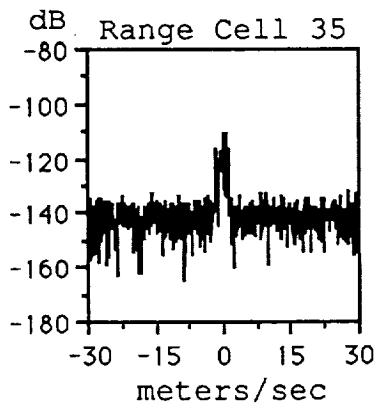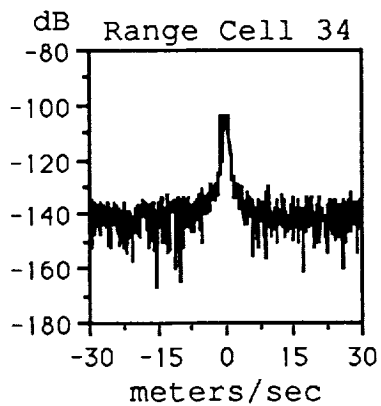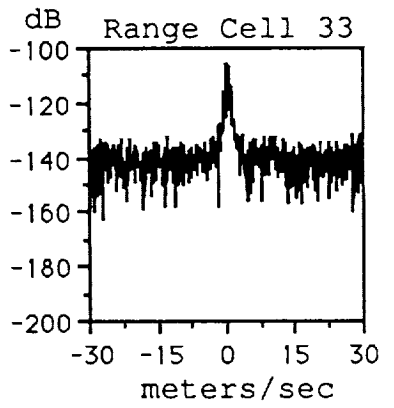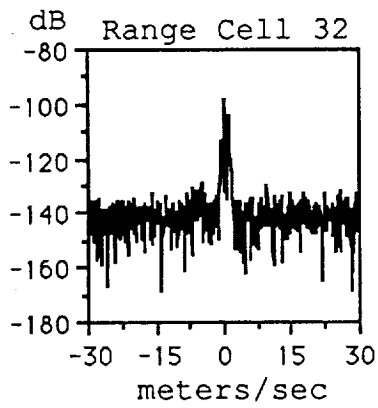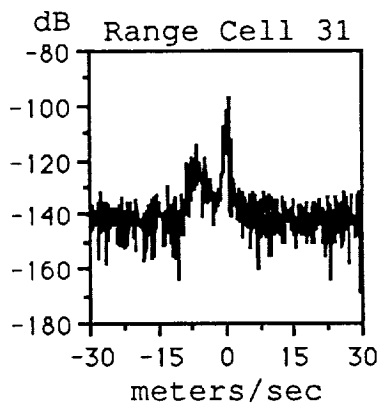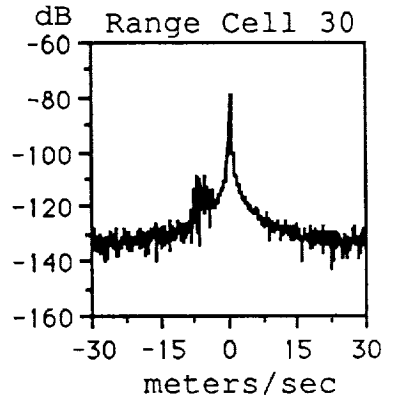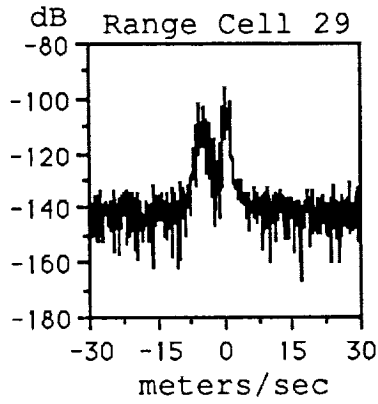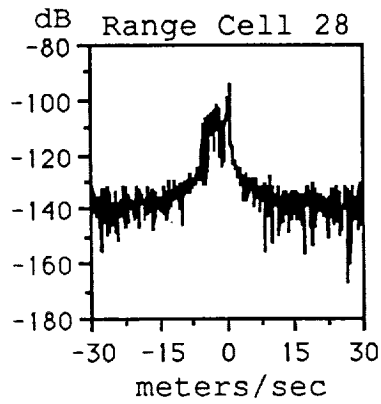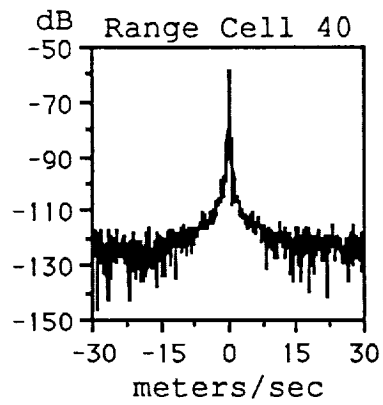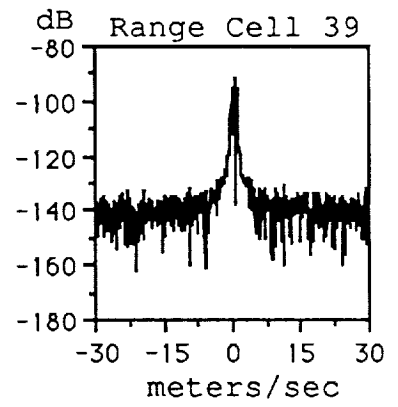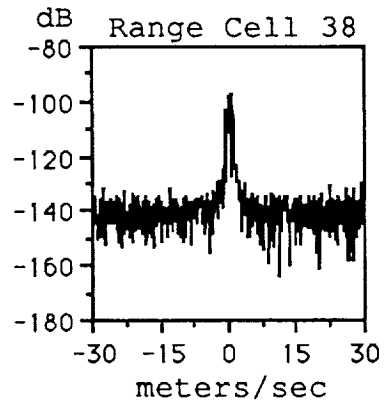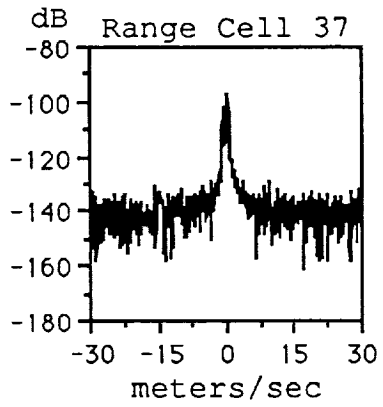
Appendix D

Fourier Spectral Estimates of a Dry
Microburst Without Clutter

Range Cell 37

Range Cell 38

Range Cell 39

Range Cell 40
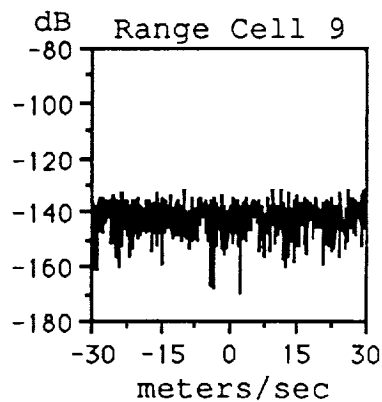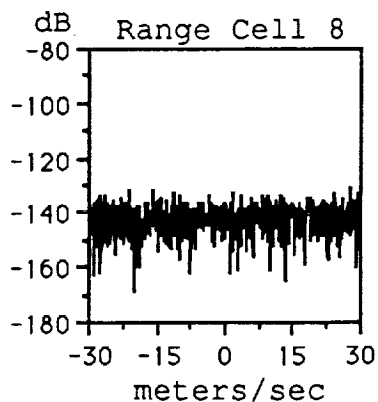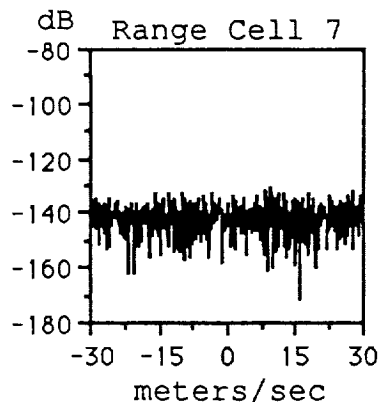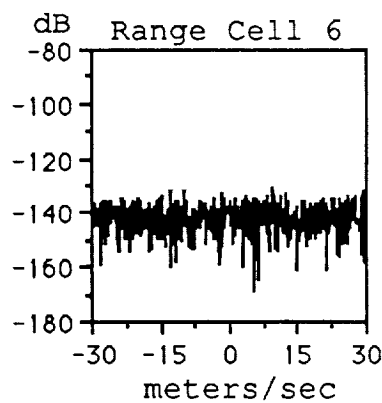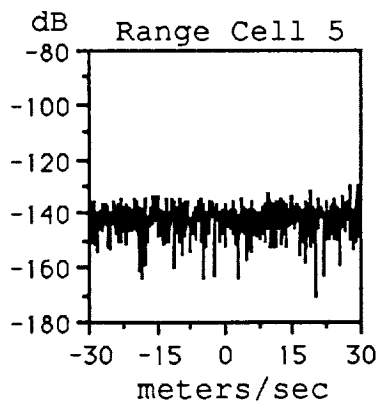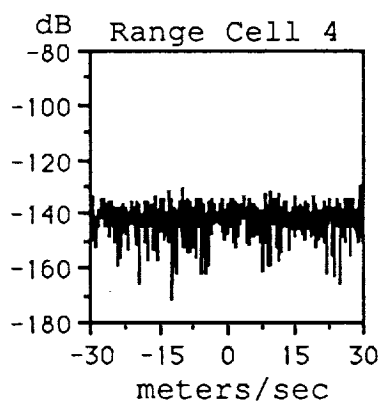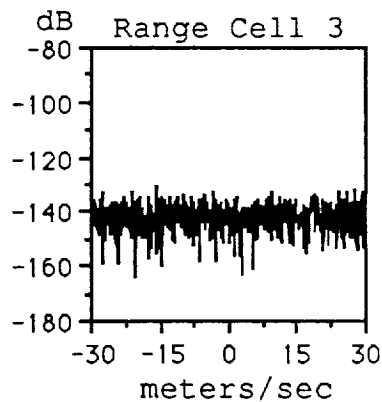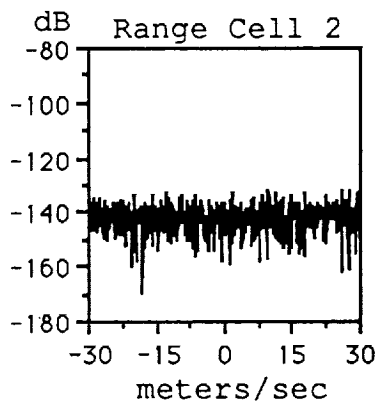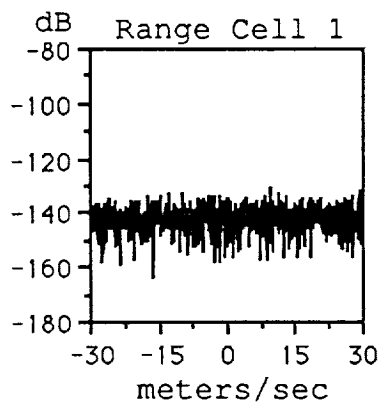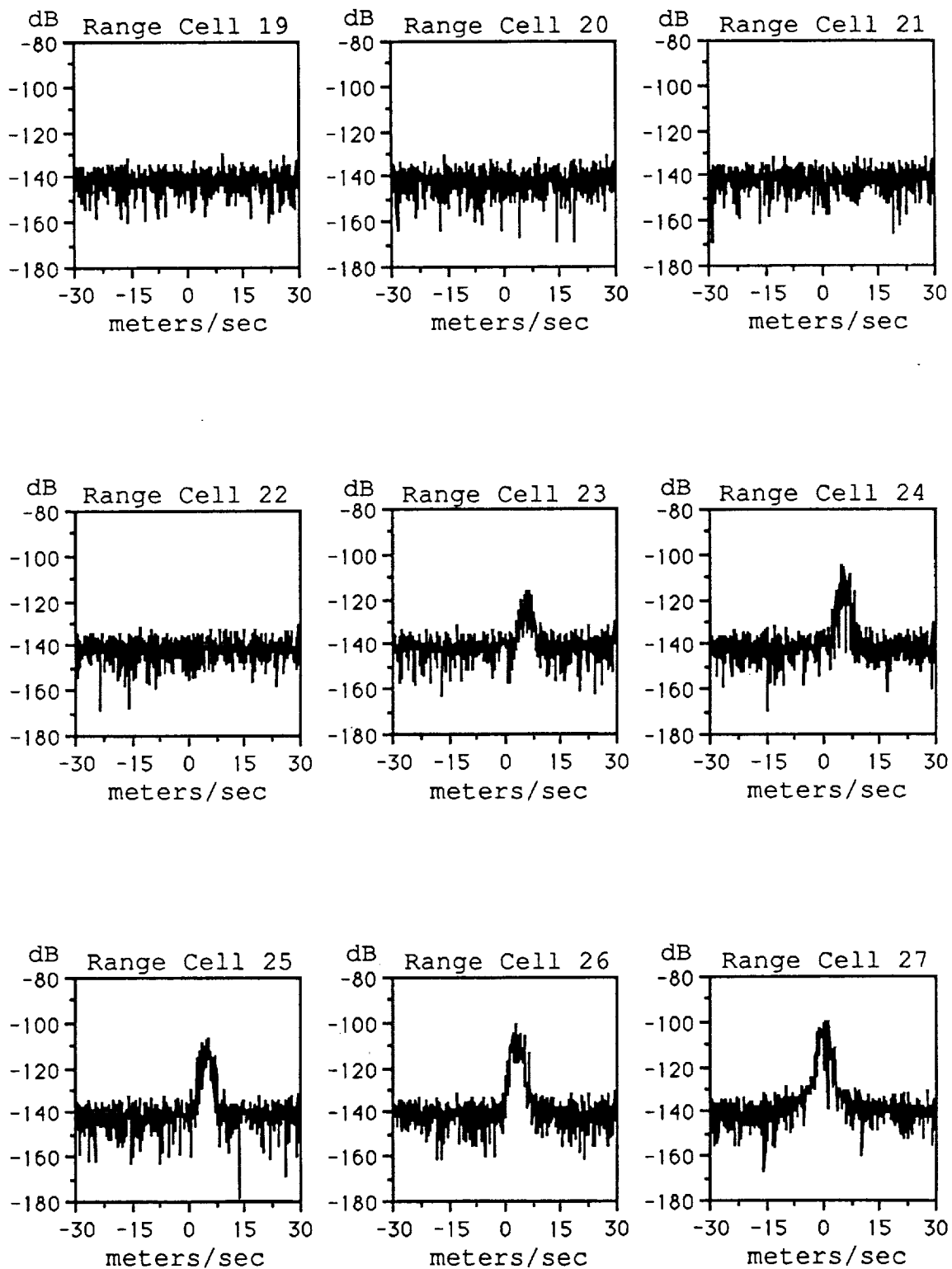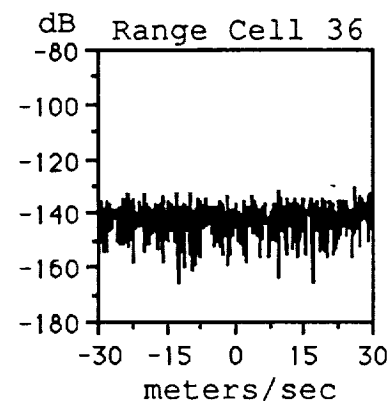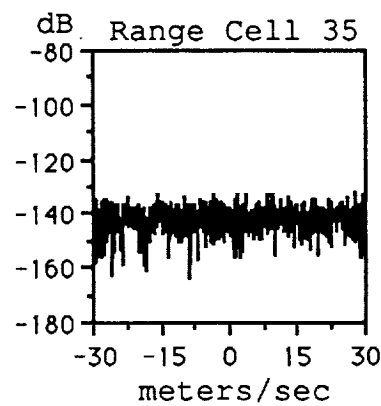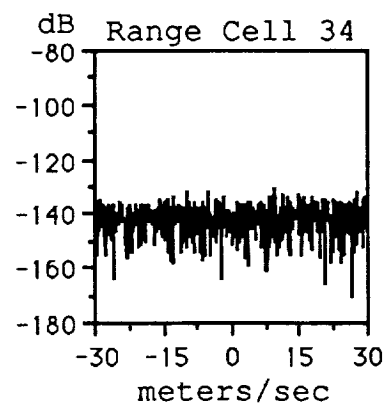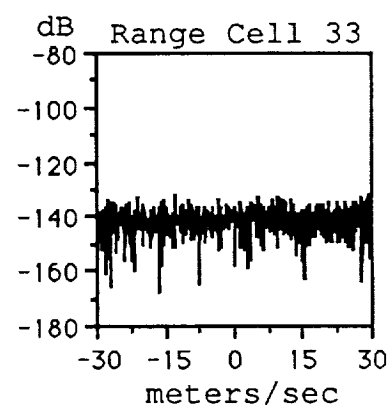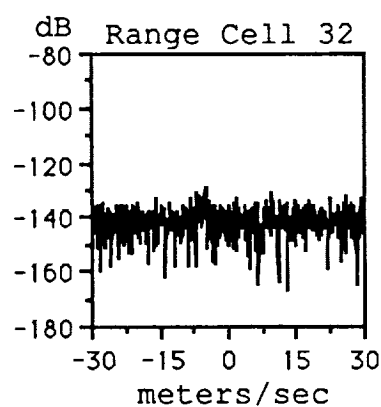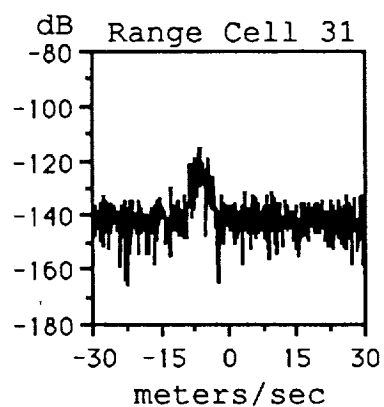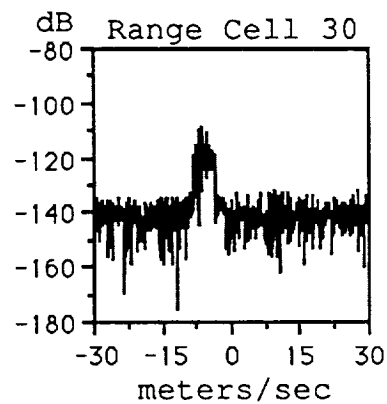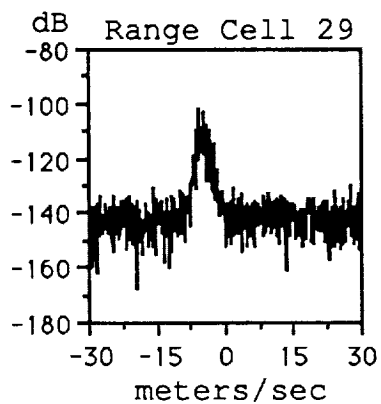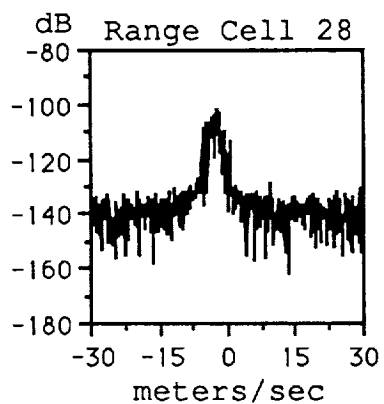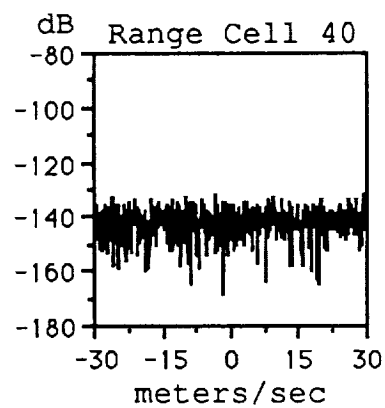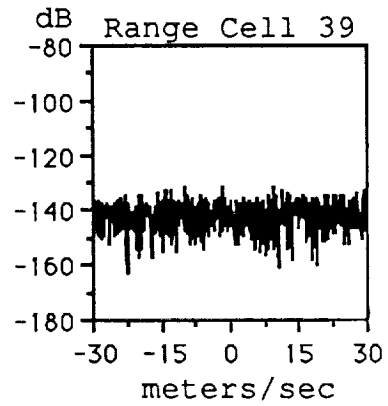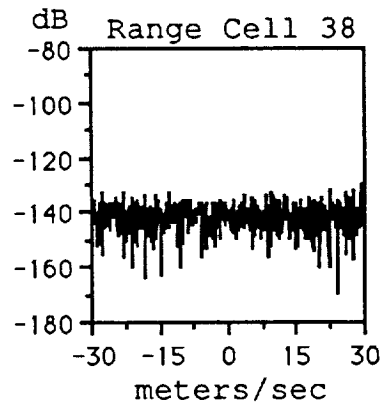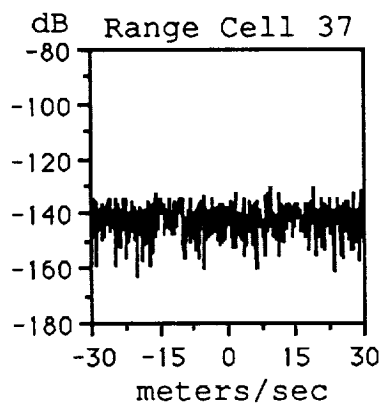
Appendix E

Fourier Spectral Estimates of Clutter

Range Cell 28, Range Cell 29, Range Cell 30, Range Cell 31, Range Cell 32, Range Cell 33, Range Cell 34, Range Cell 35, Range Cell 36
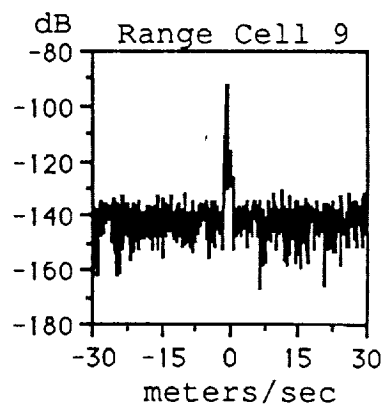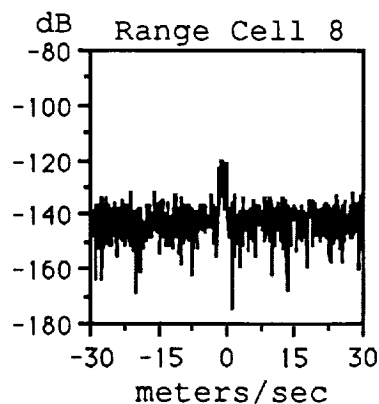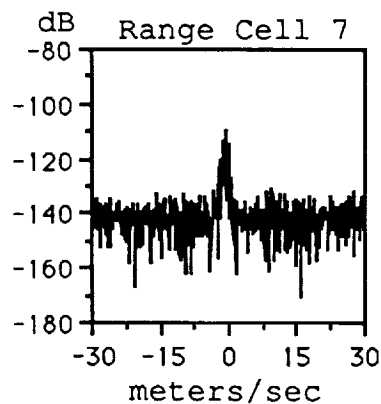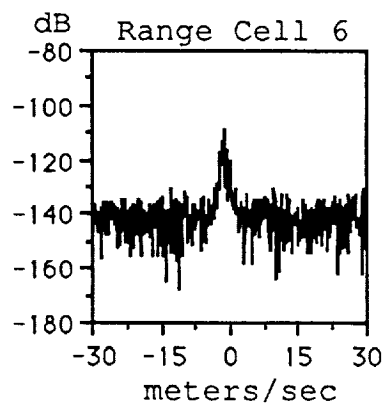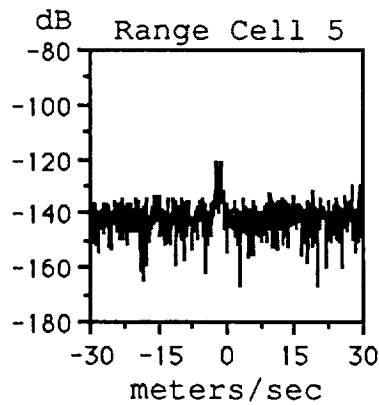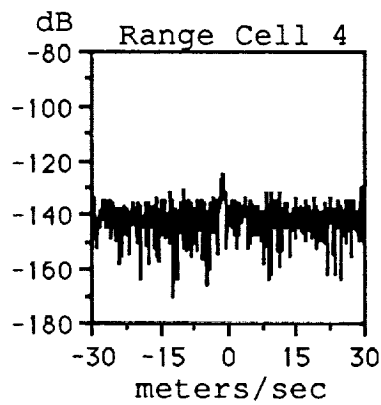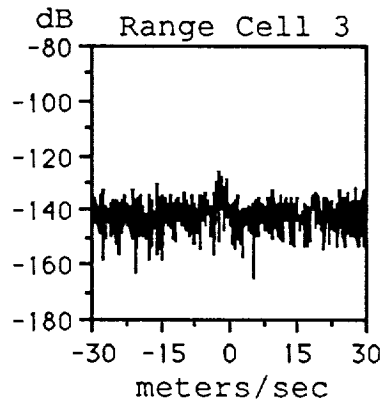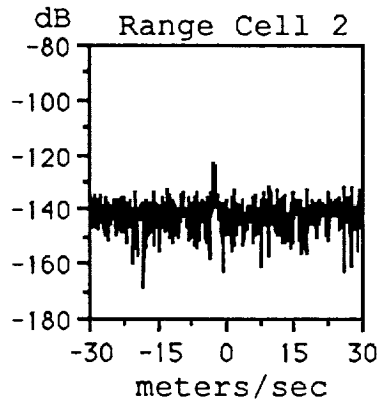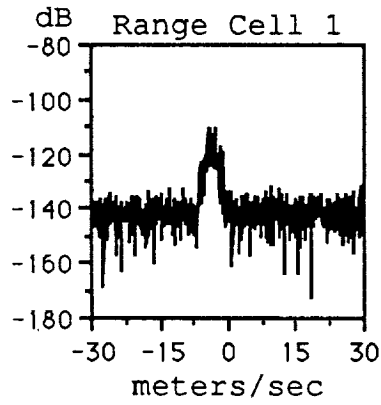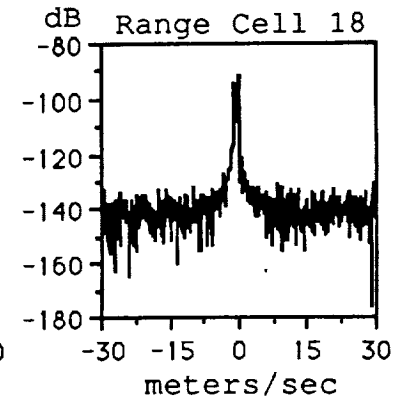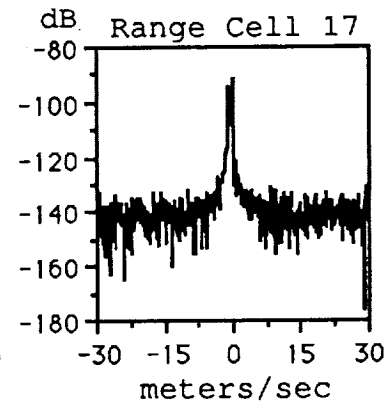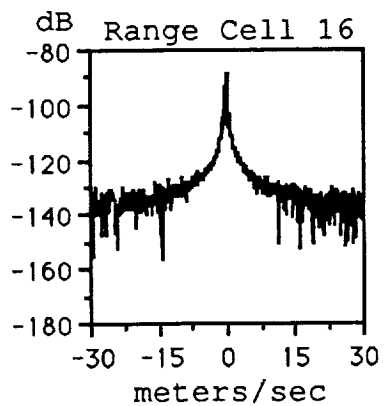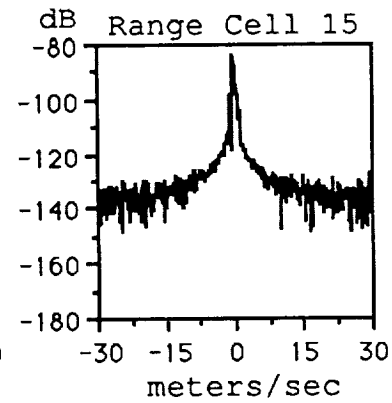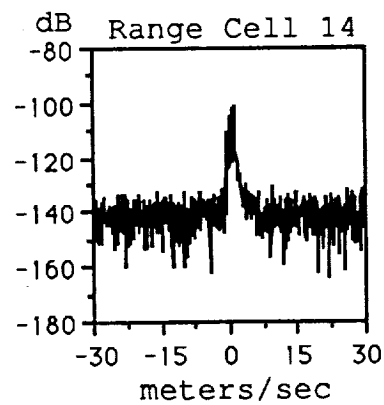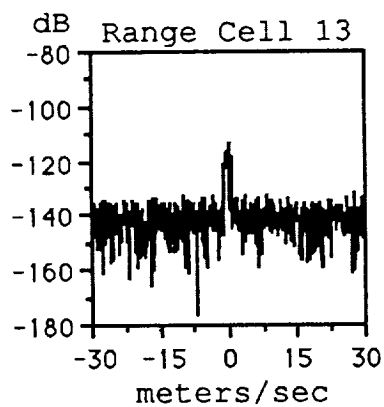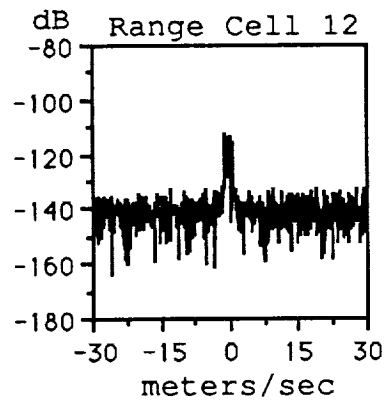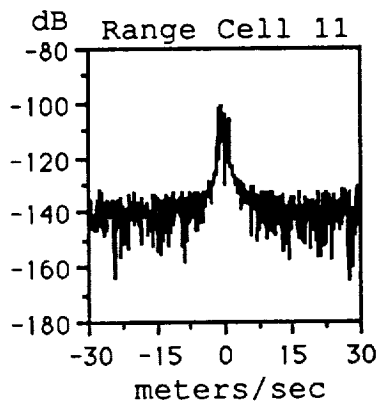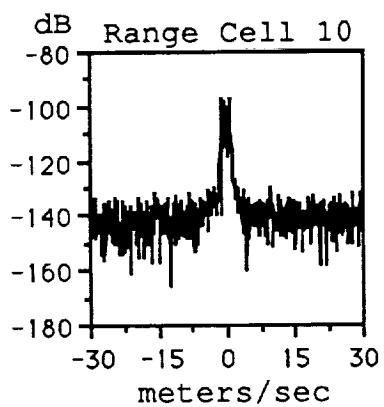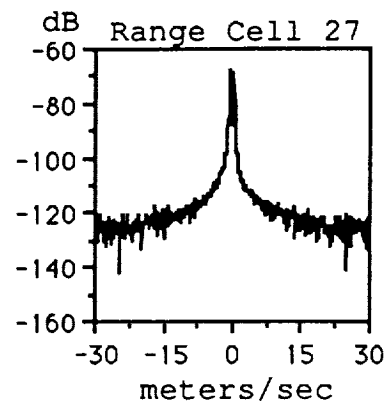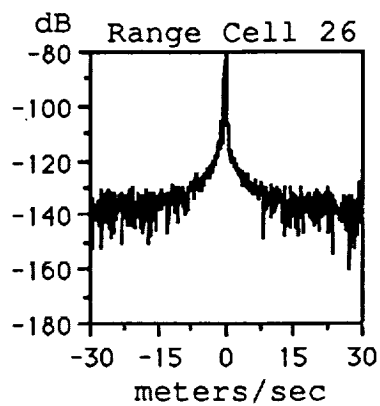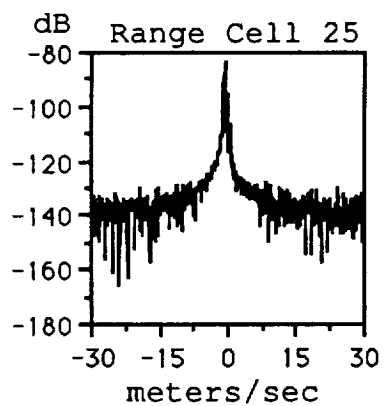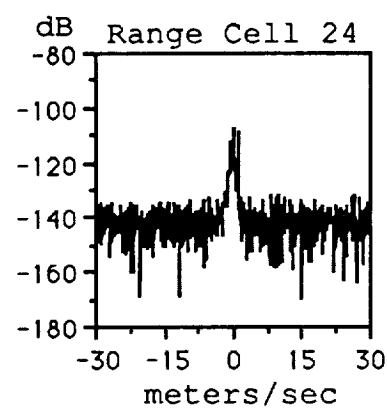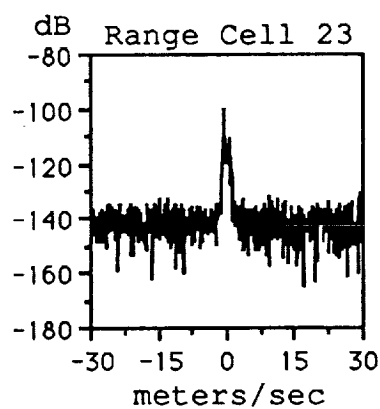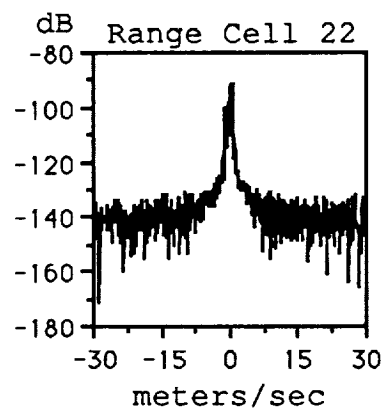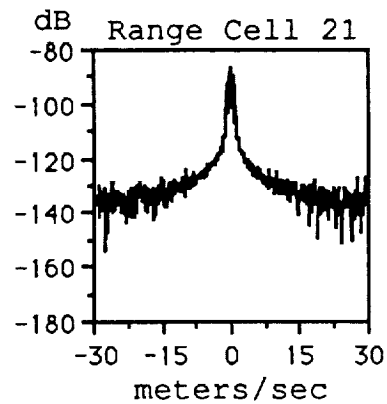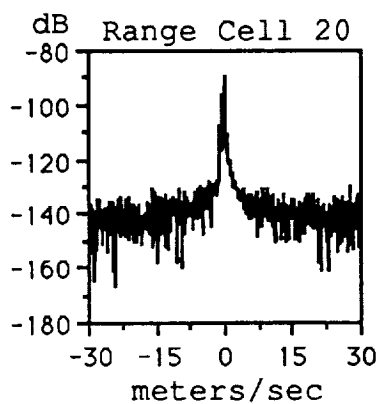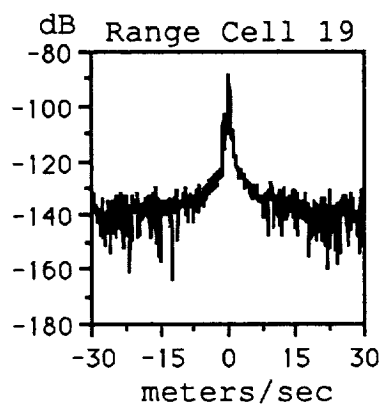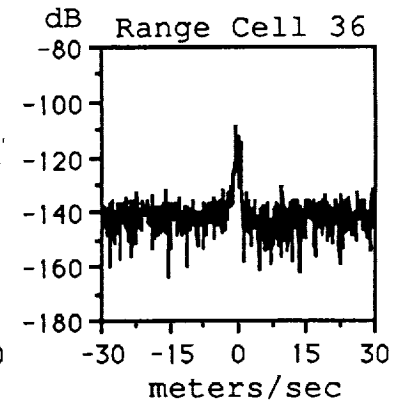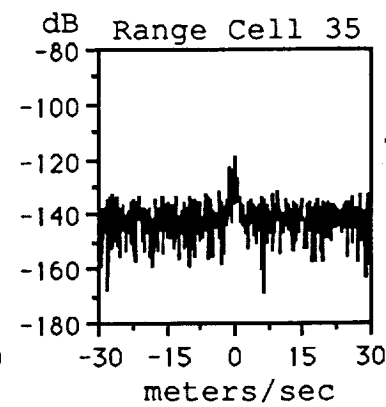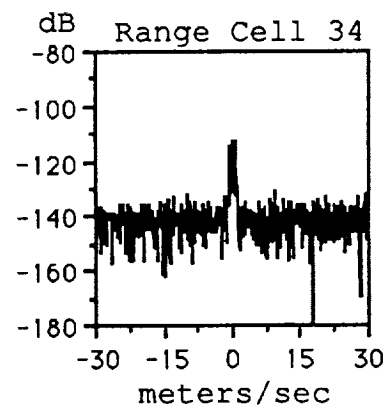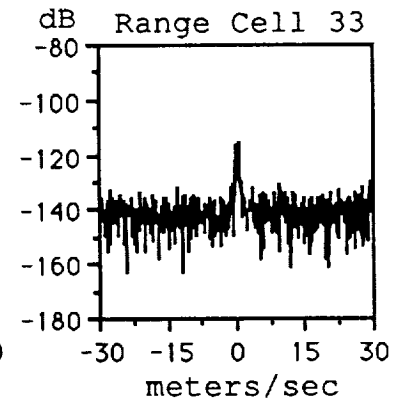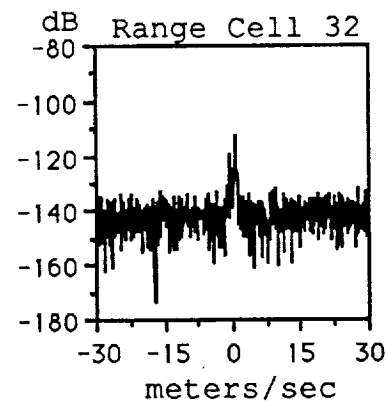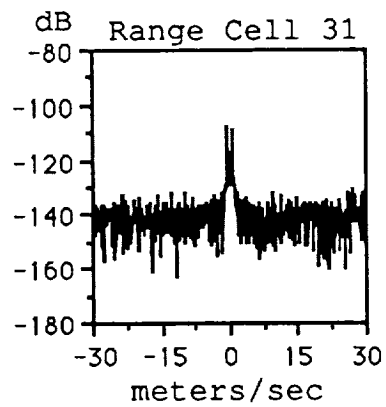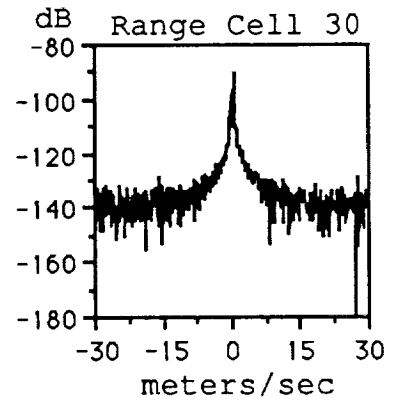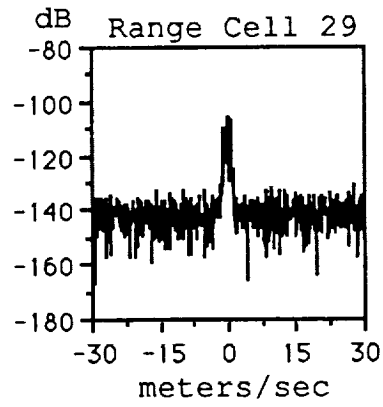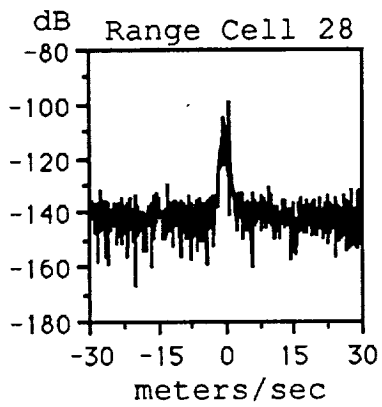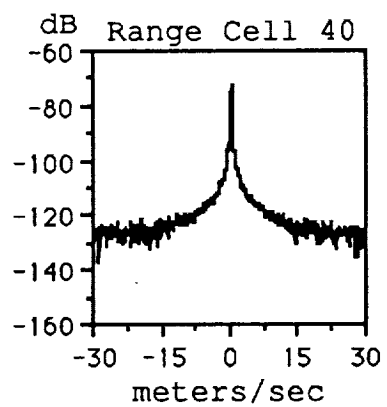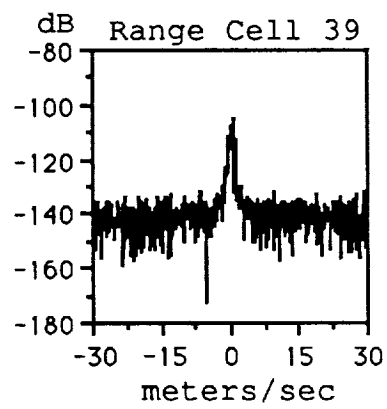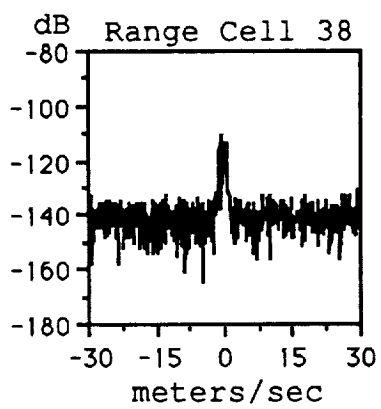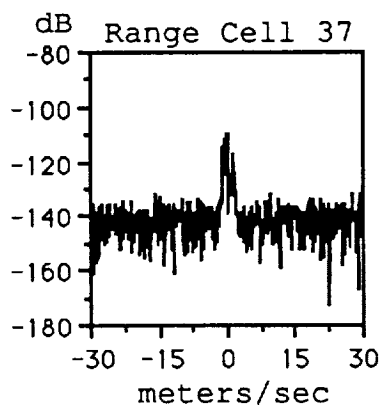
Appendix F

Magnitude Response of the 10th Order
FIR Filters

Range Cell 19, Range Cell 20, Range Cell 21, Range Cell 22, Range Cell 23, Range Cell 24, Range Cell 25, Range Cell 26, Range Cell 27

Range Cell 37

Range Cell 38

Range Cell 39
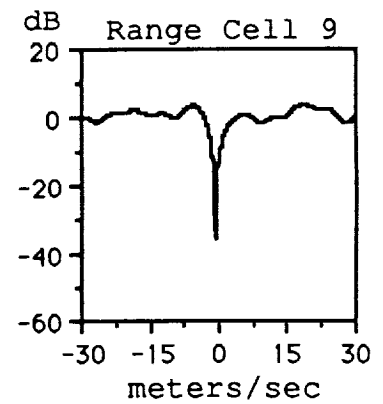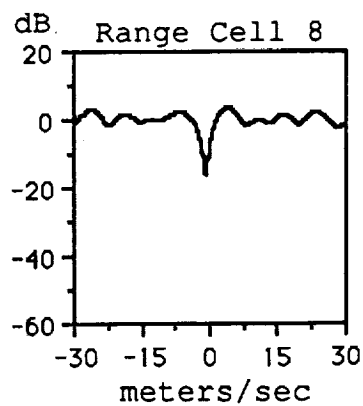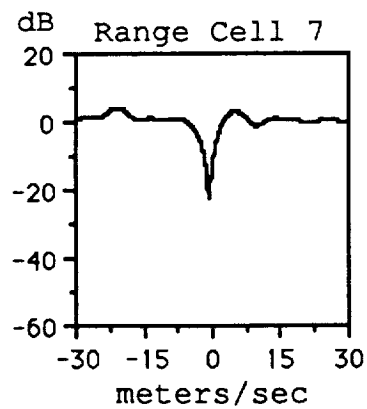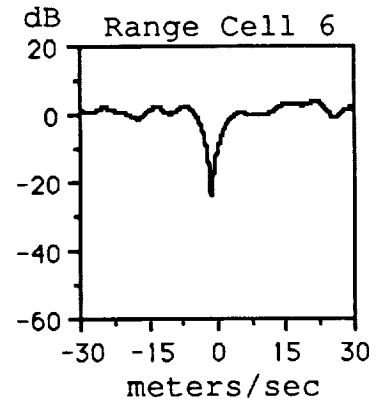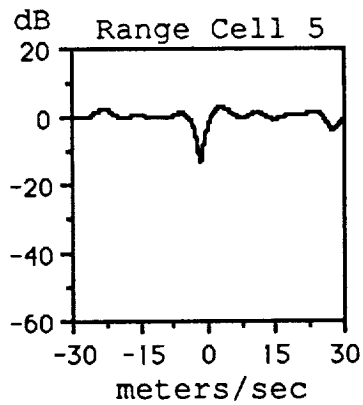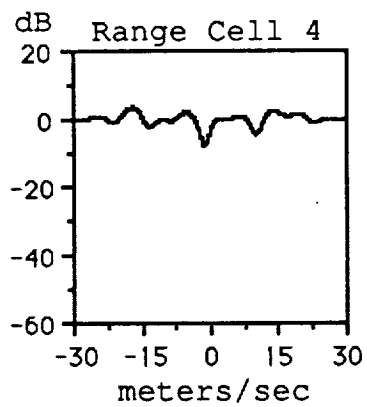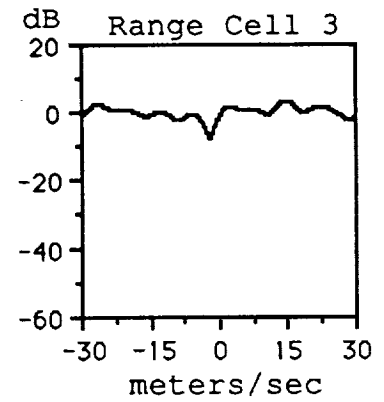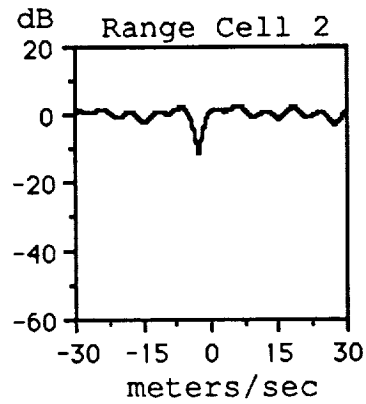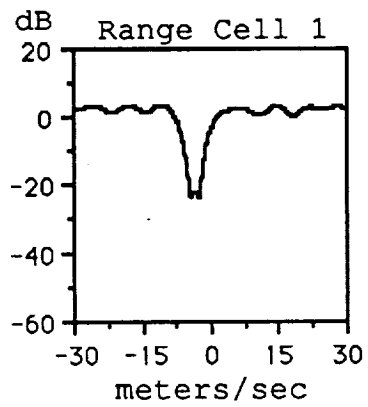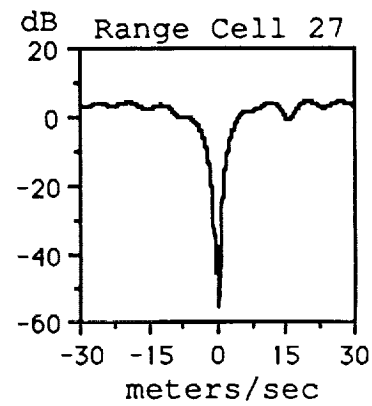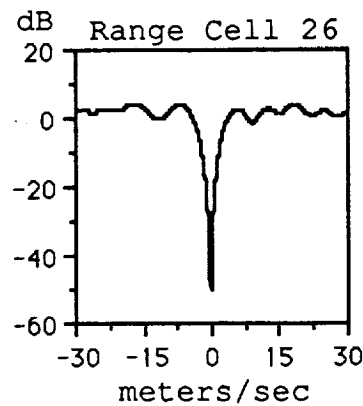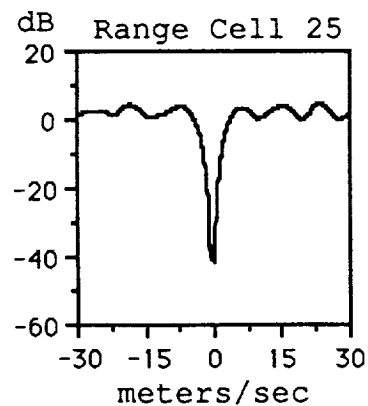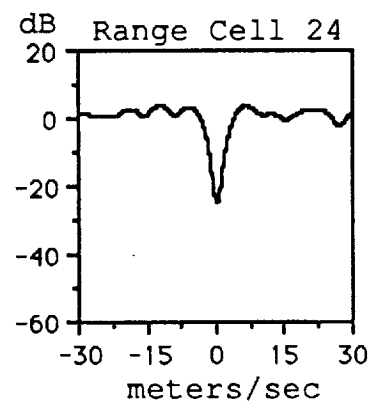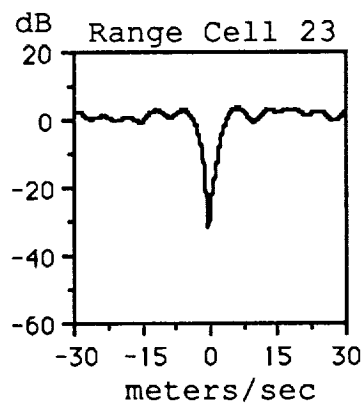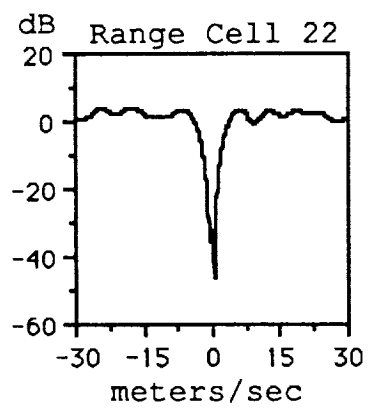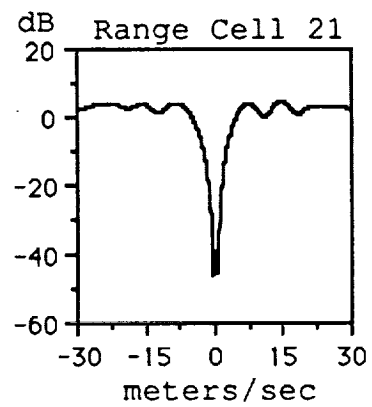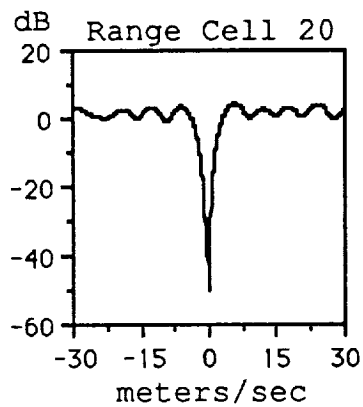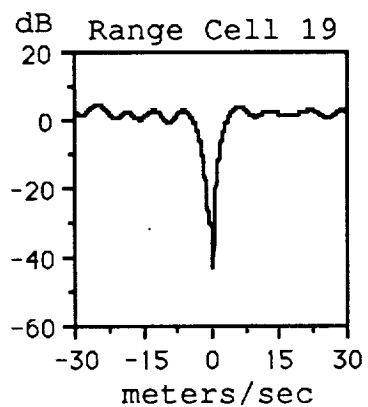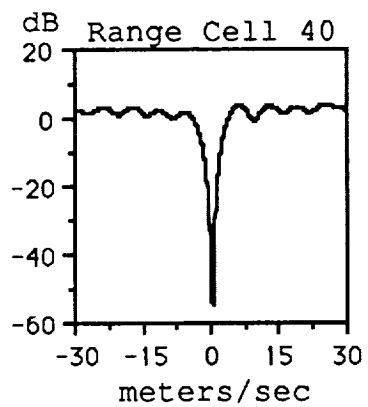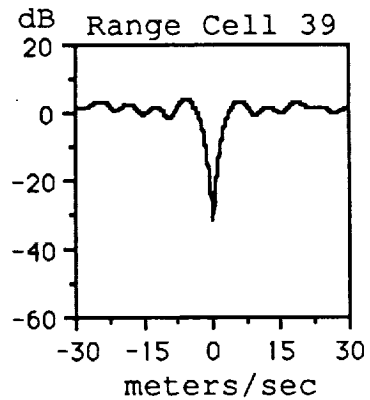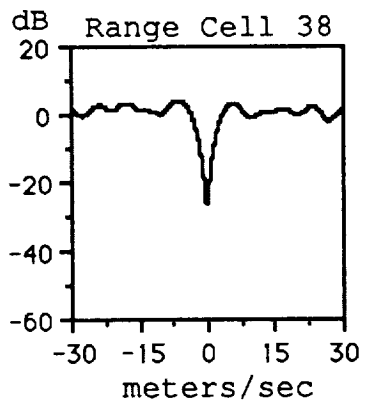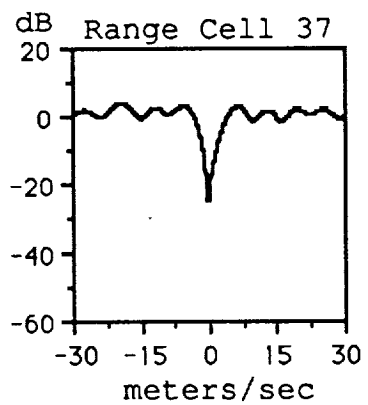
Range Cell 40

Appendix G

Phase Response of the 10th Order
FIR Filters

Range Cell 28

Range Cell 29

Range Cell 30

Range Cell 31

Range Cell 32

Range Cell 33

Range Cell 34

Range Cell 35

Range Cell 36

Range Cell 37

Range Cell 38

Range Cell 39
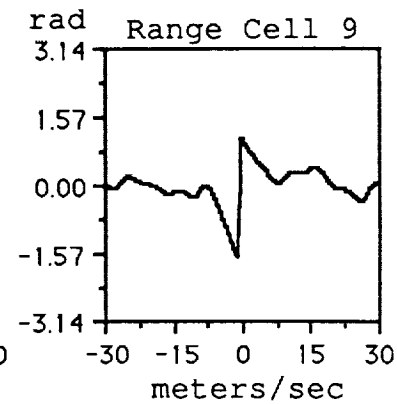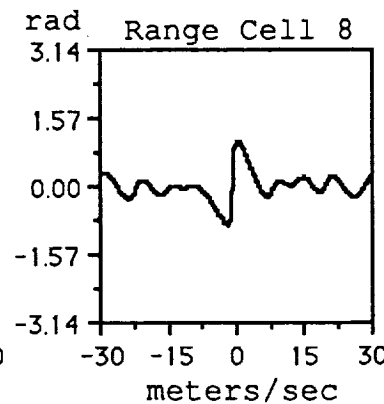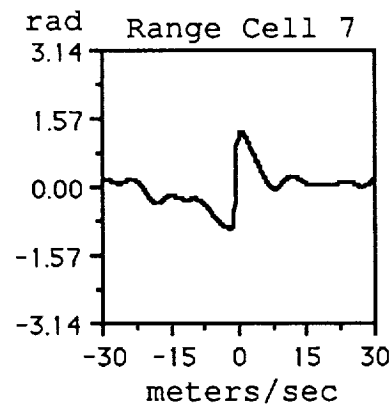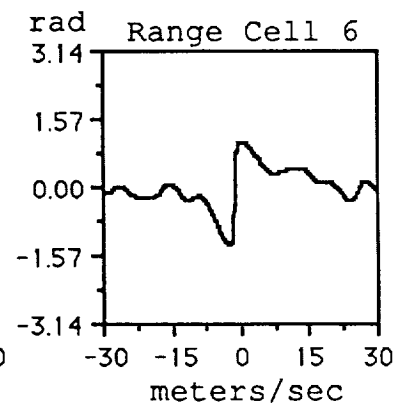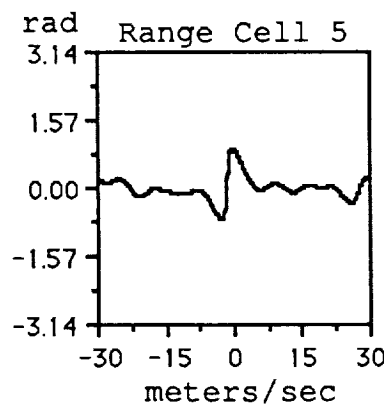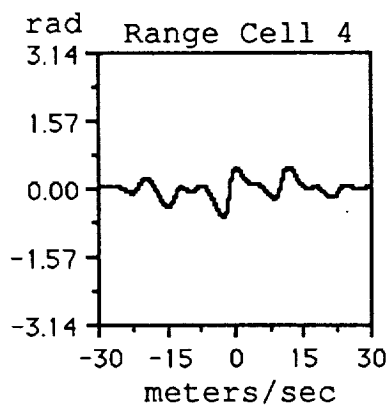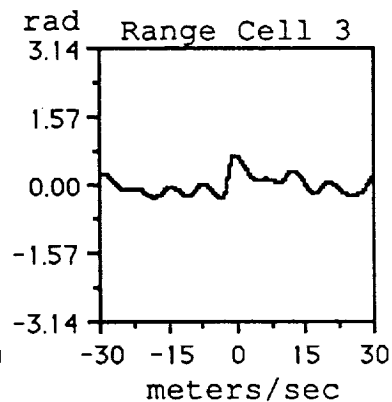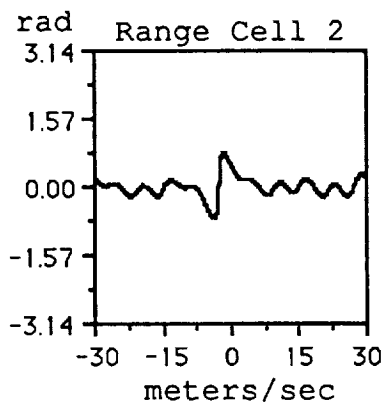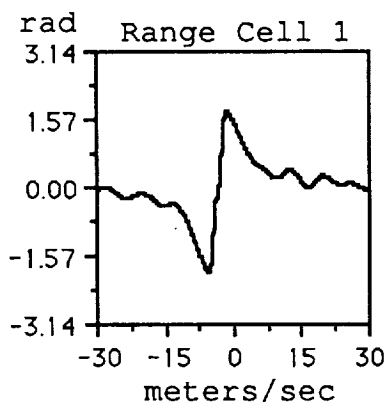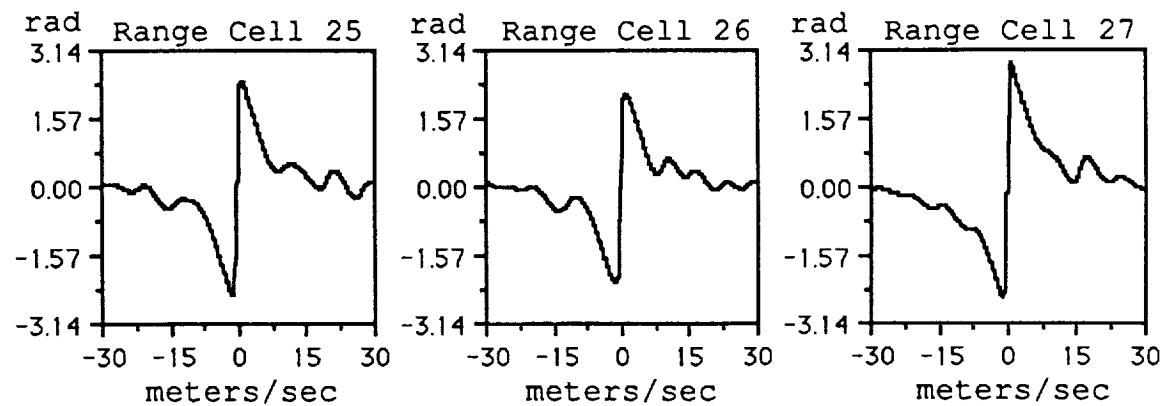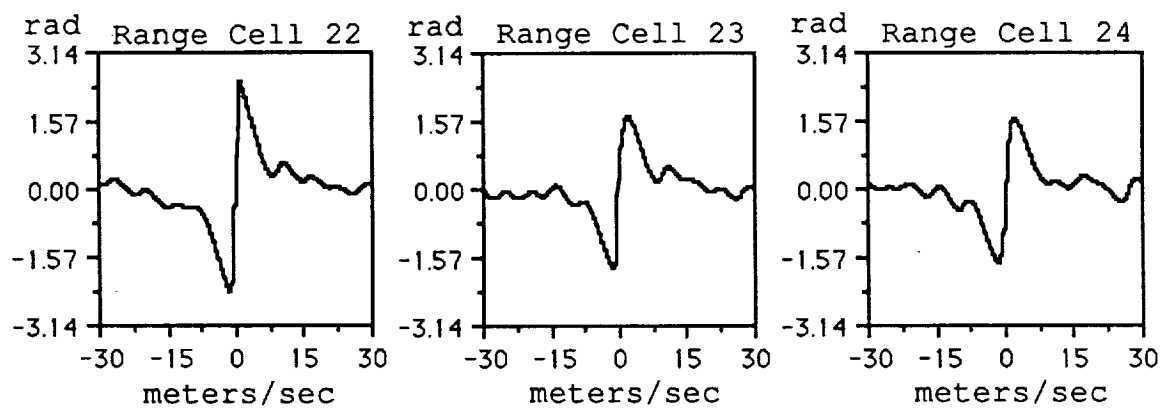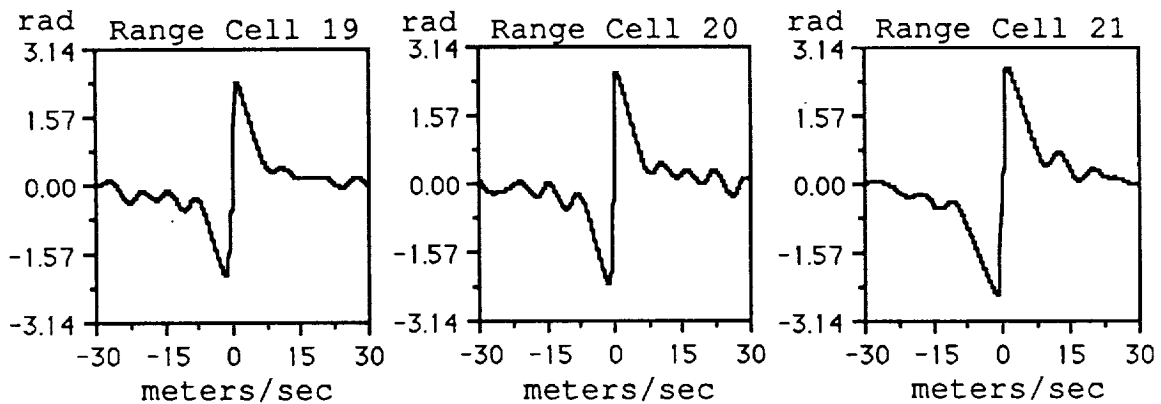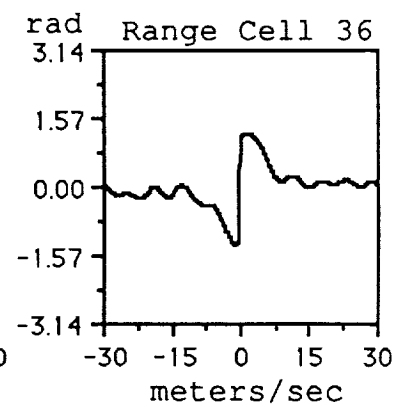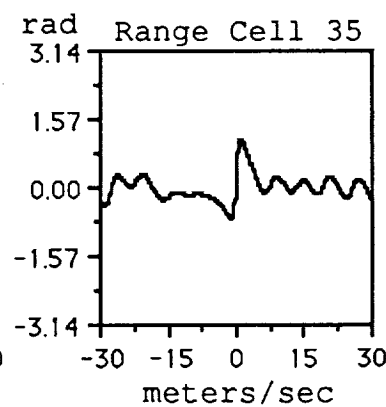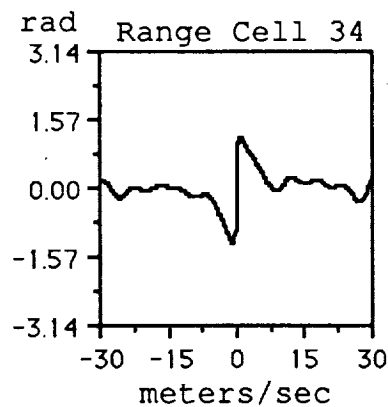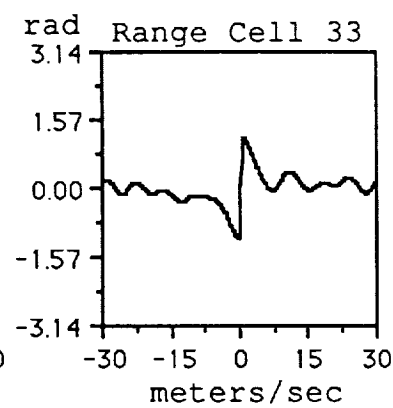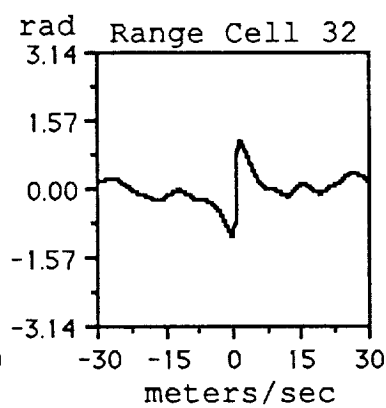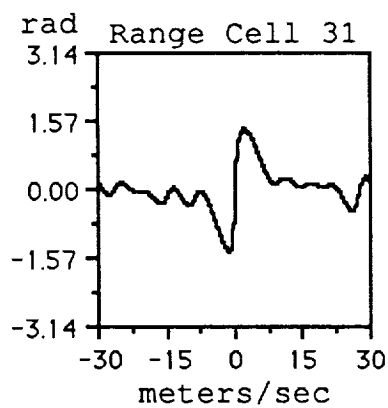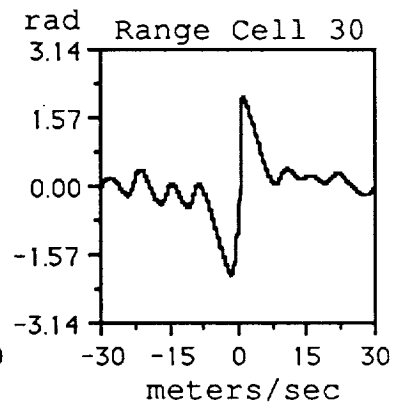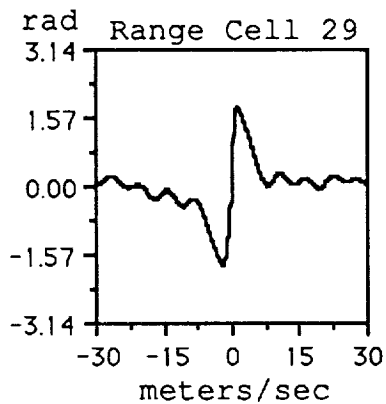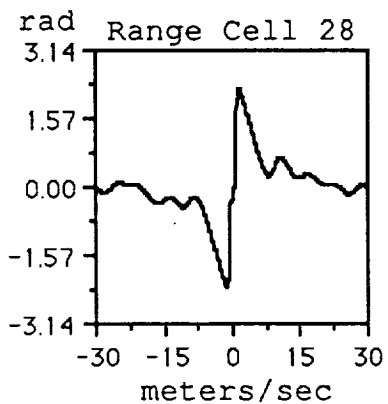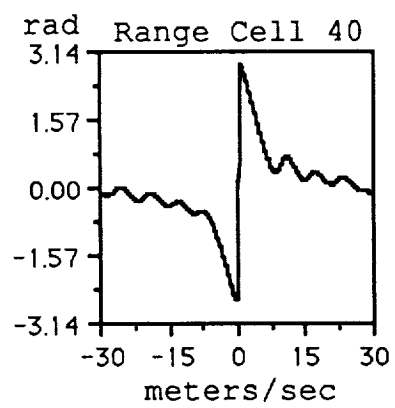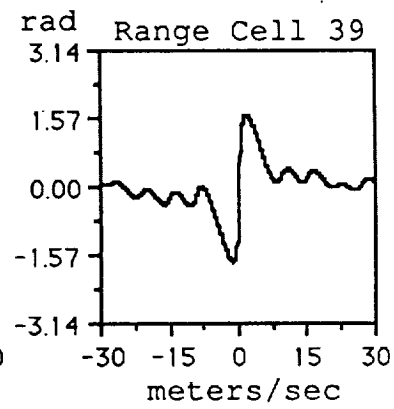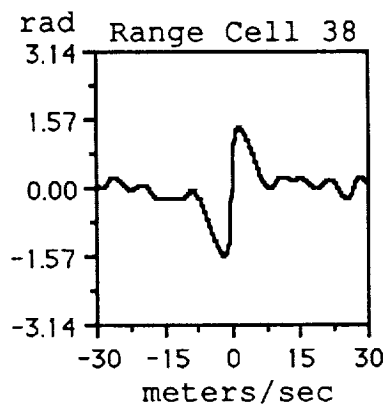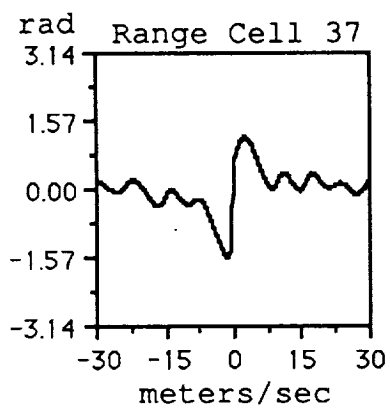
Range Cell 40

Appendix H

Filtered Spectrum Using the Appropriate
Model Based Filter Coefficients
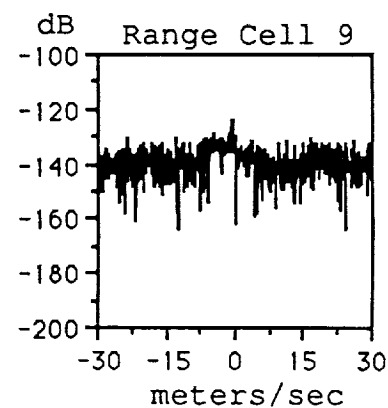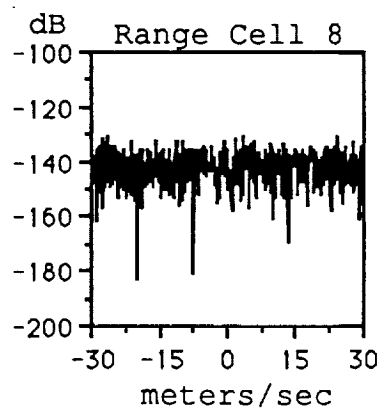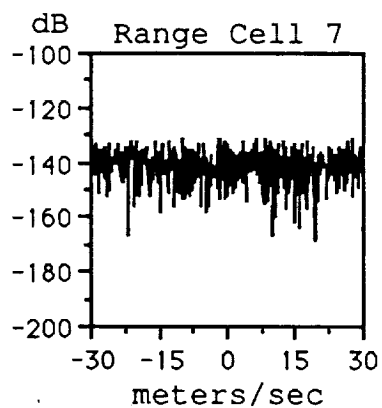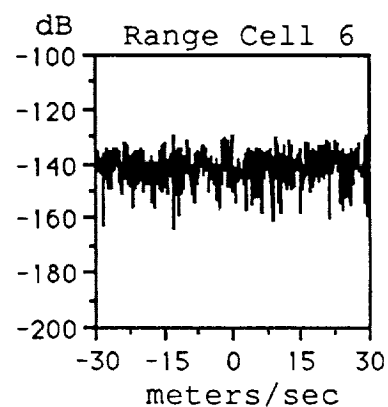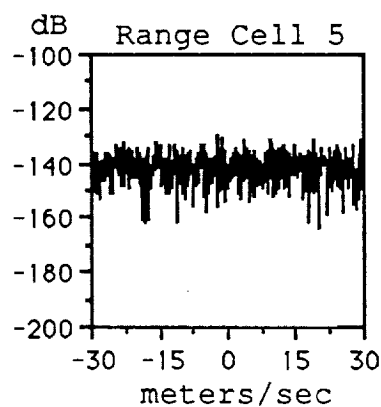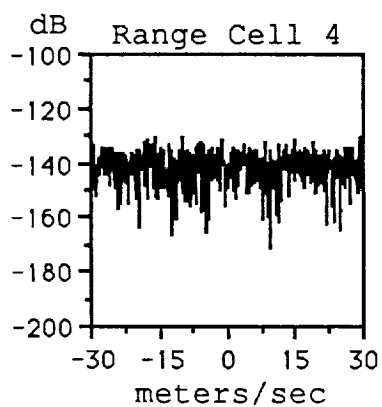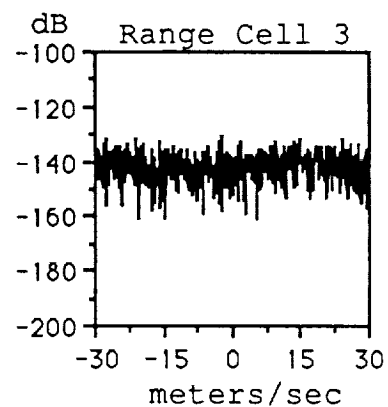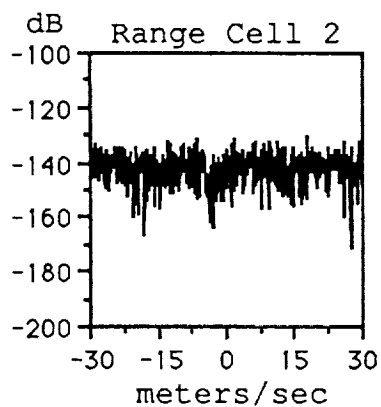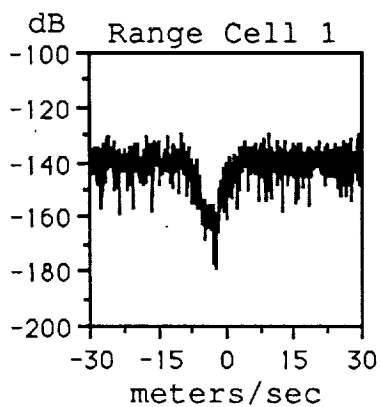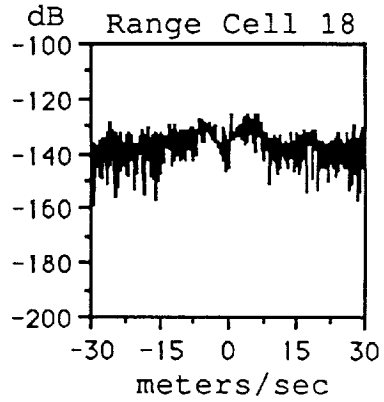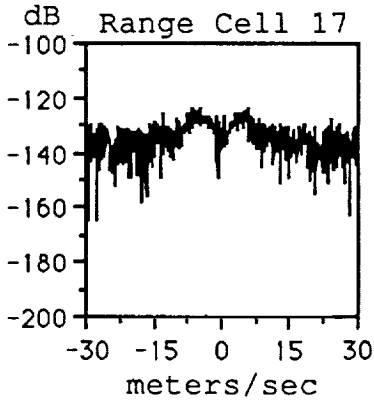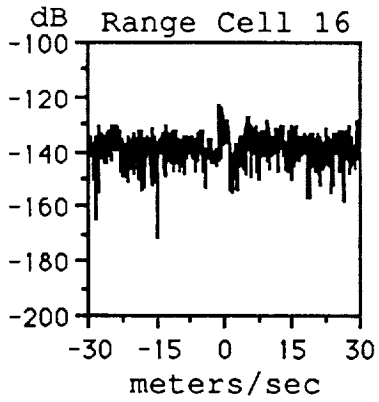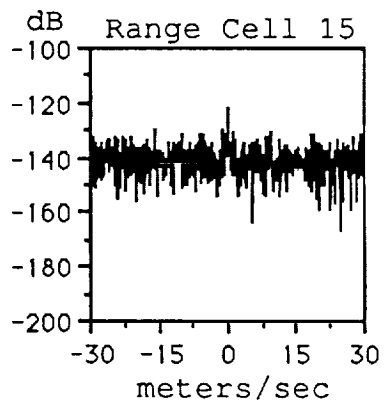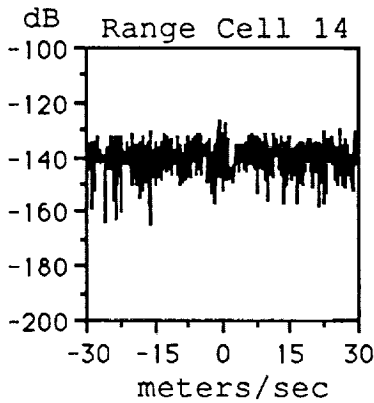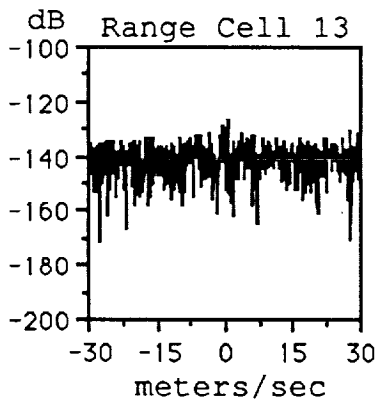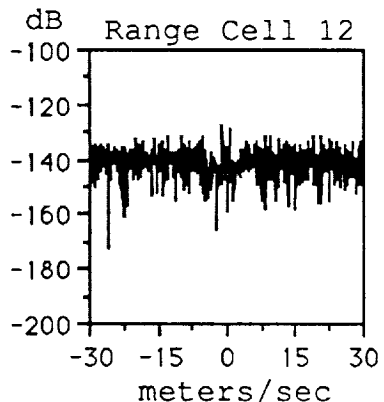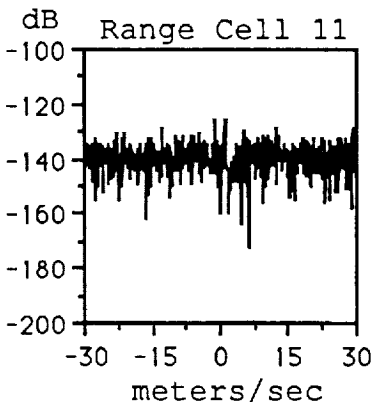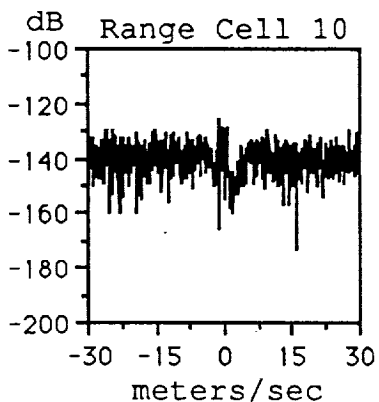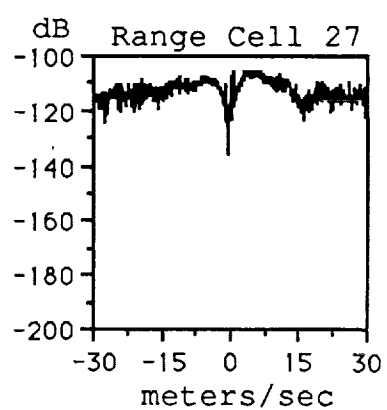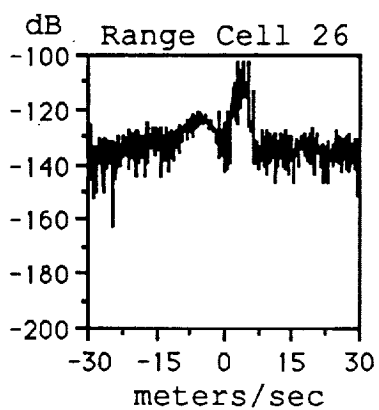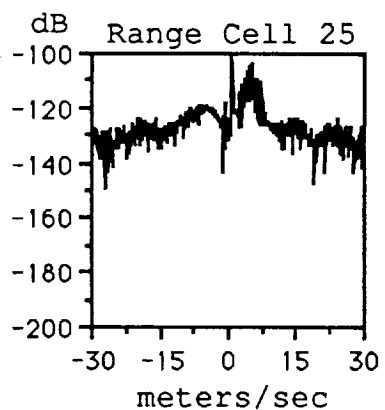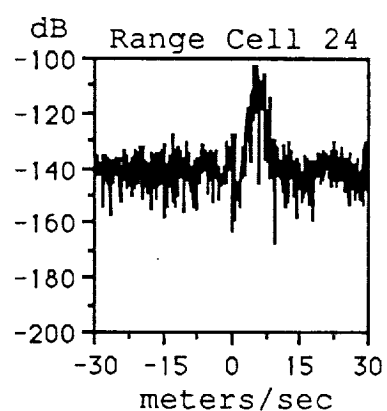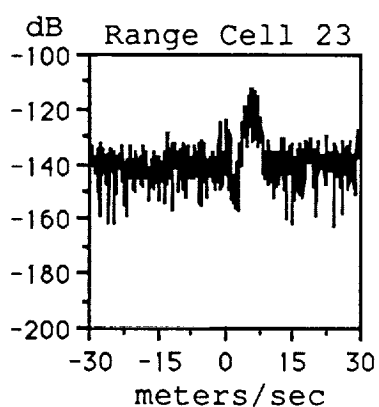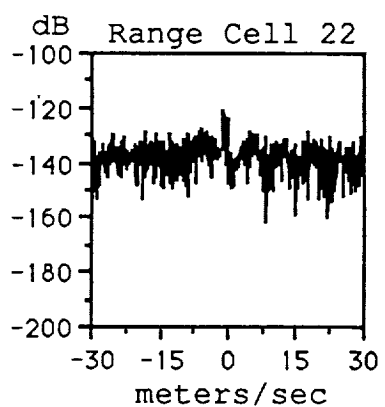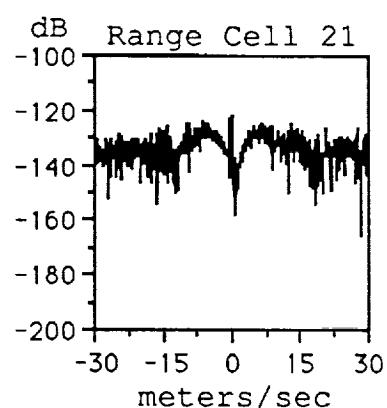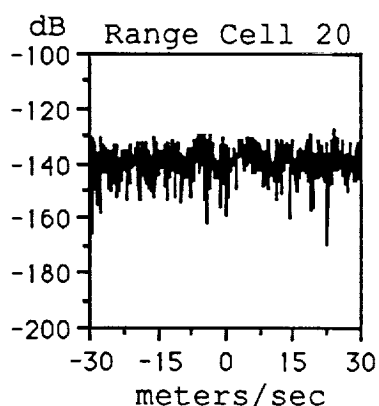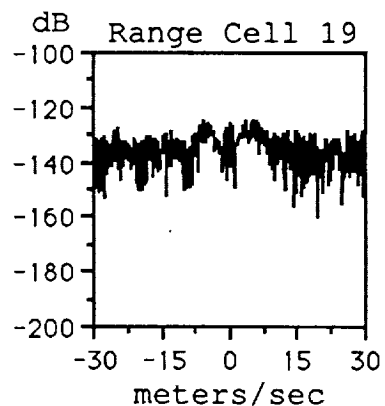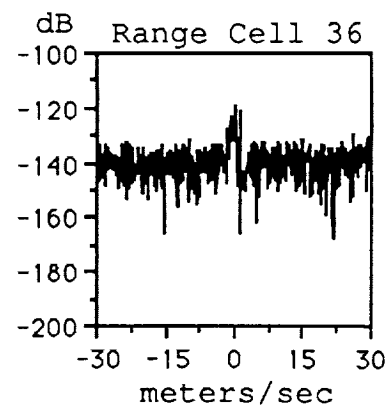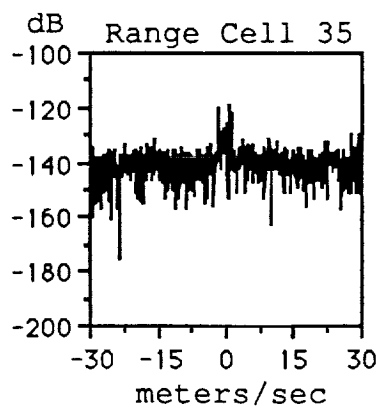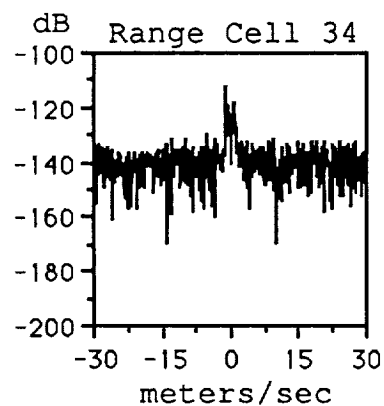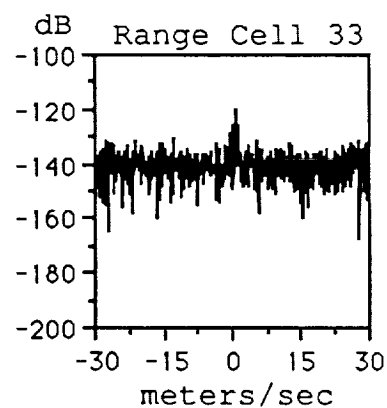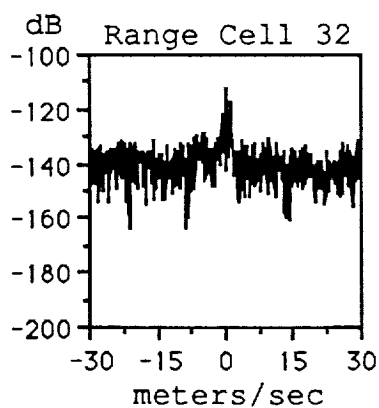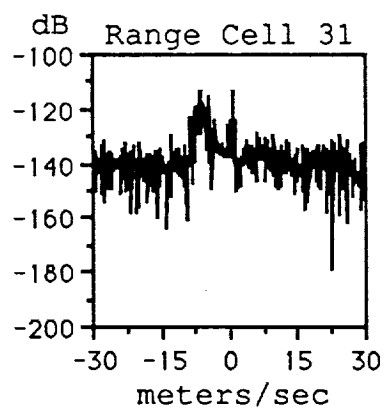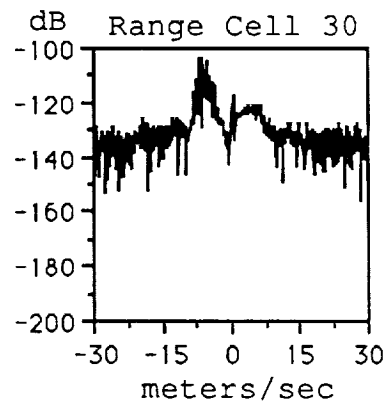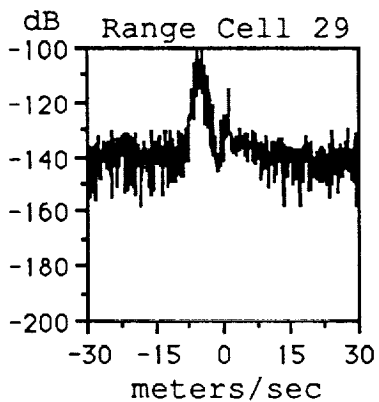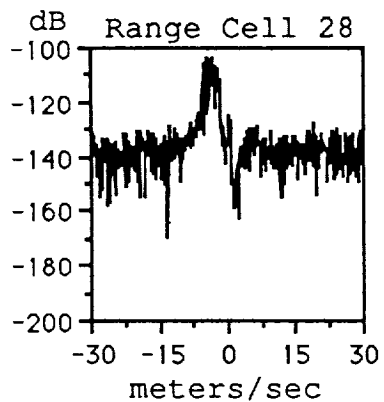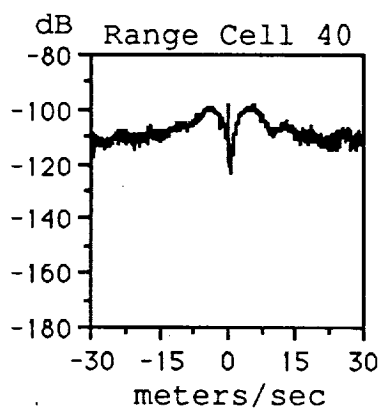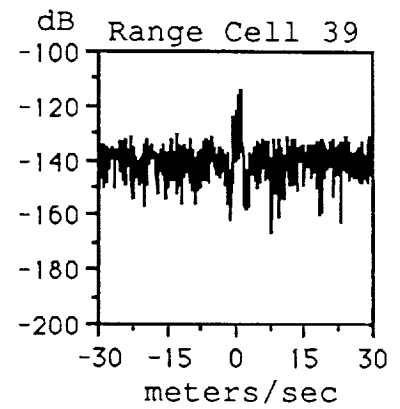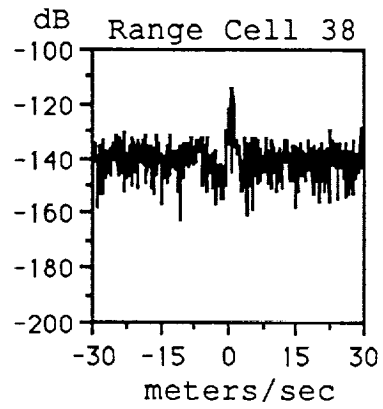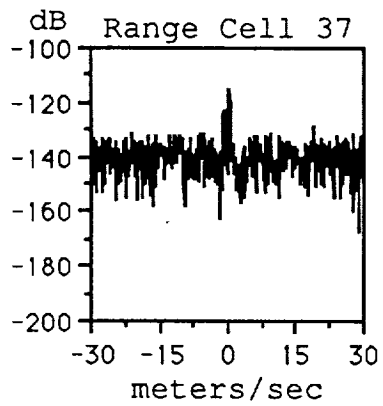
Appendix I

Filtered Spectrum Using the Filter
Coefficients for Range Cell 20

Range Cell 1 — Range Cell 2 — Range Cell 3 — Range Cell 4 — Range Cell 5 — Range Cell 6 — Range Cell 7 — Range Cell 8 — Range Cell 9

Range Cell 19 / Range Cell 20 / Range Cell 21 / Range Cell 22 / Range Cell 23 / Range Cell 24 / Range Cell 25 / Range Cell 26 / Range Cell 27

Range Cell 28

Range Cell 29

Range Cell 30

Range Cell 31

Range Cell 32

Range Cell 33

Range Cell 34

Range Cell 35

Range Cell 36

Range Cell 37

Range Cell 38

Range Cell 39

Range Cell 40

Appendix J

Filtered Spectrum Using a Pulse
Canceller Filter

Range Cell 37

Range Cell 38

Range Cell 39

Range Cell 40
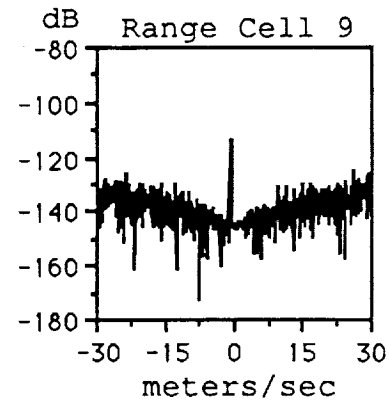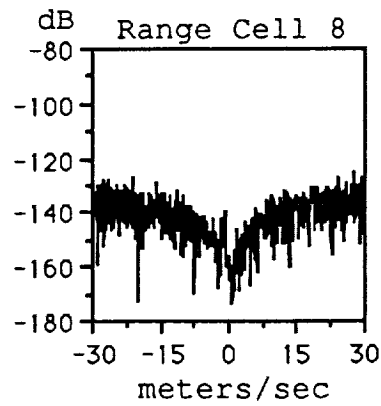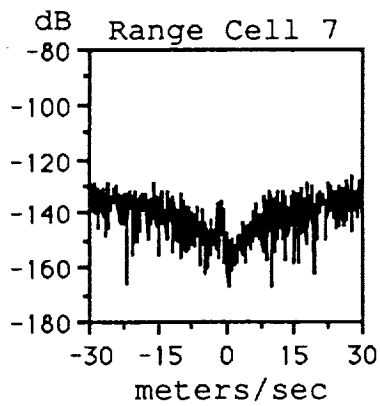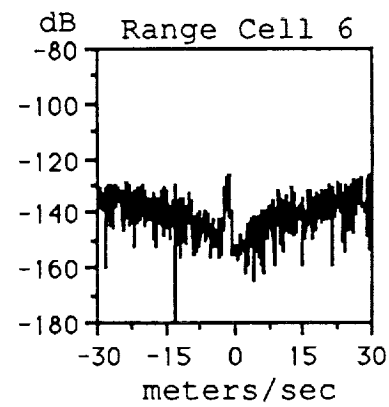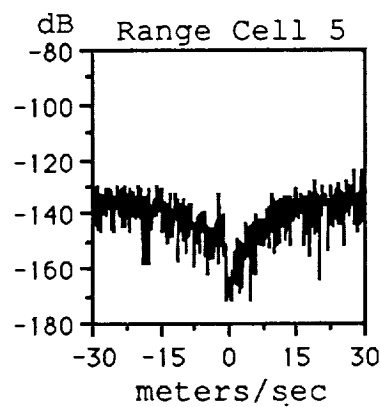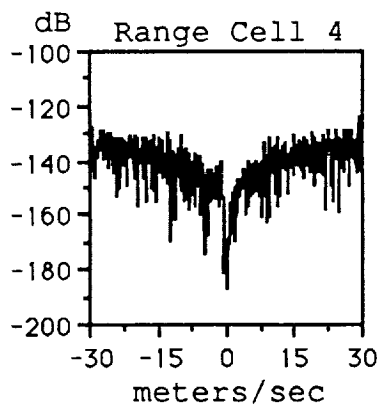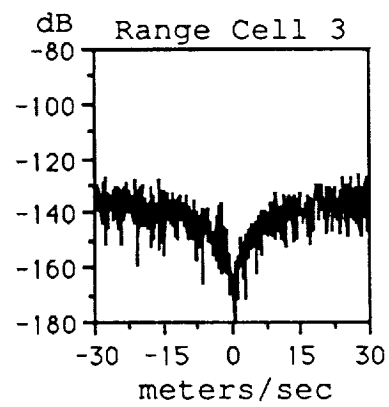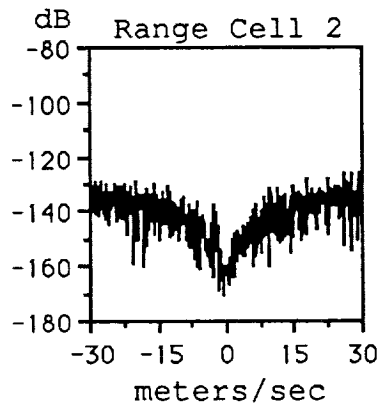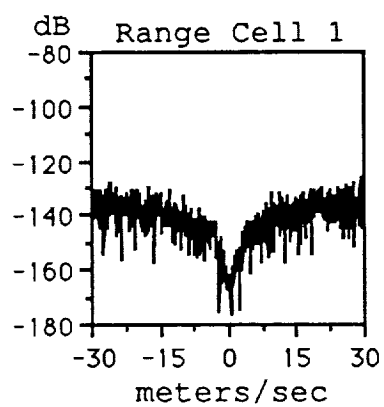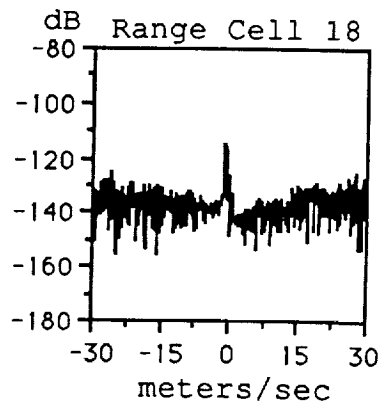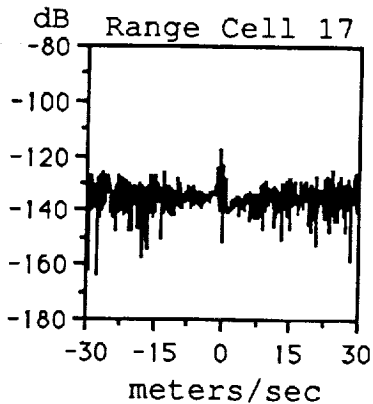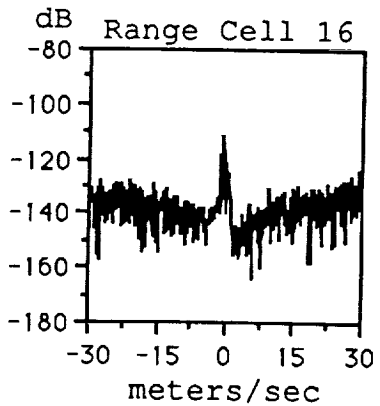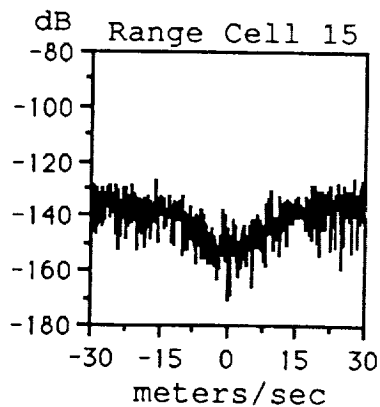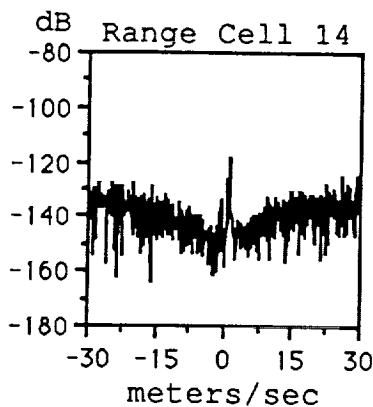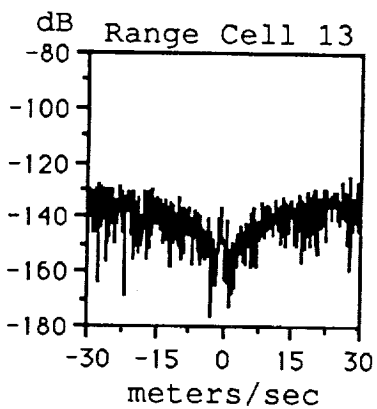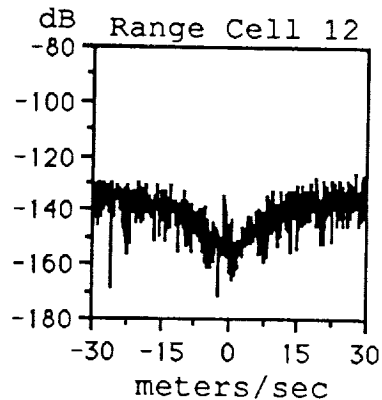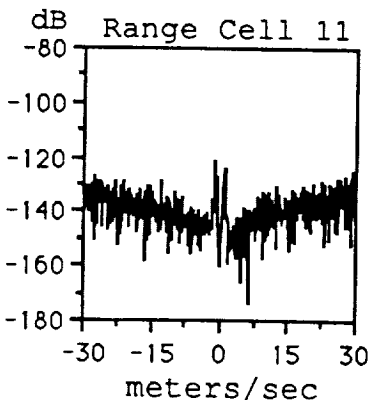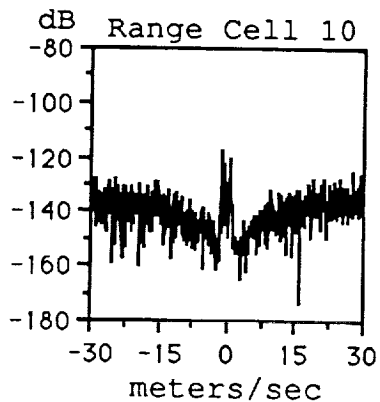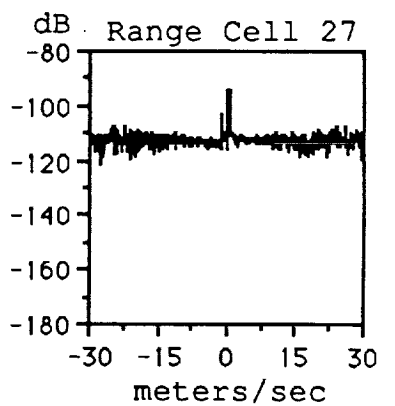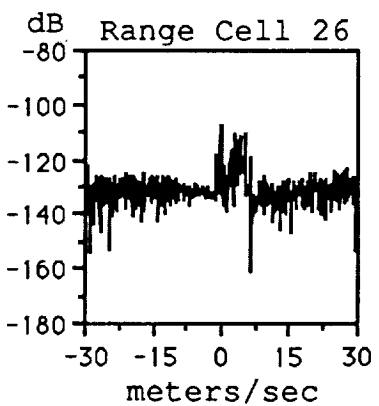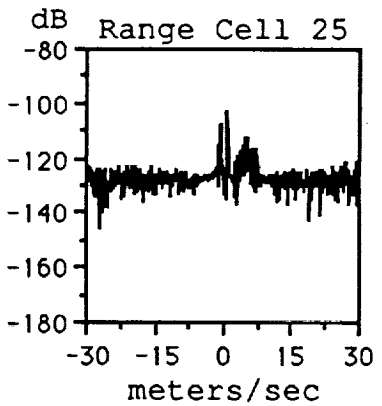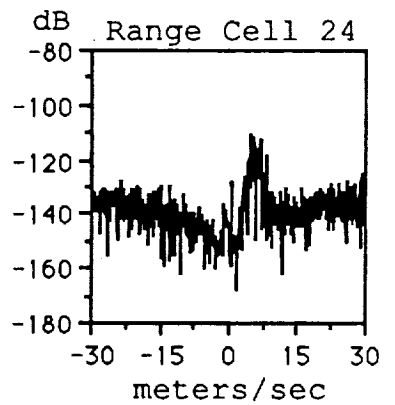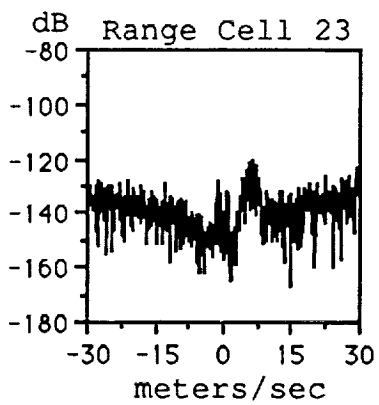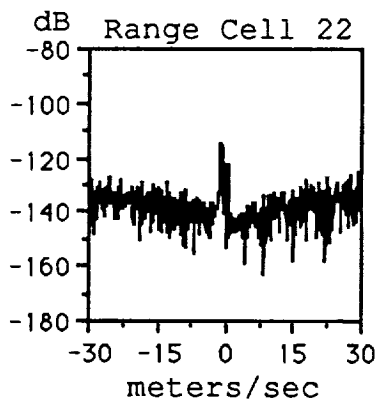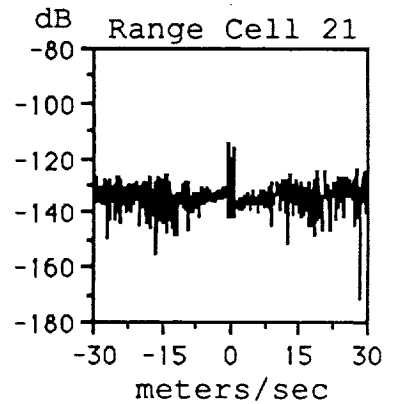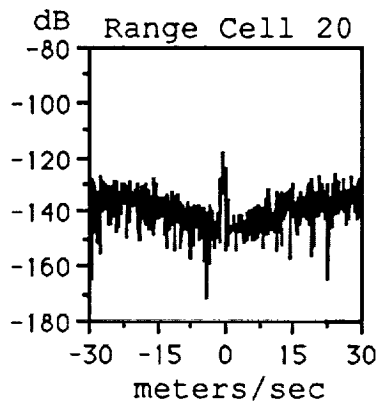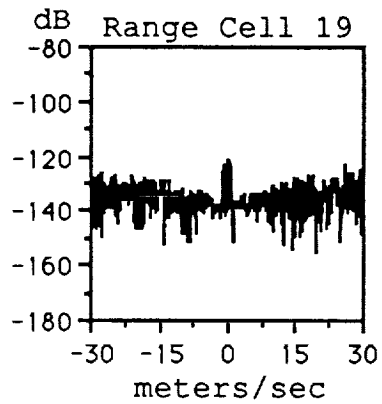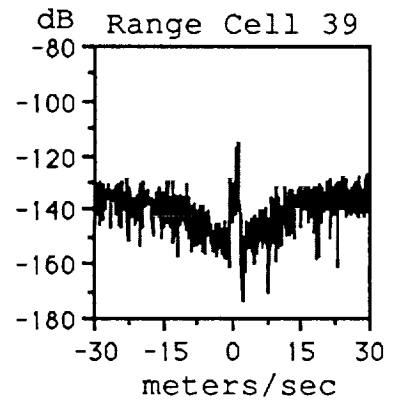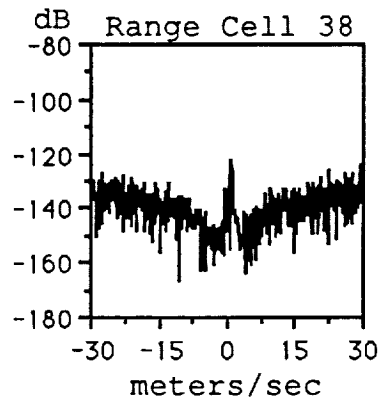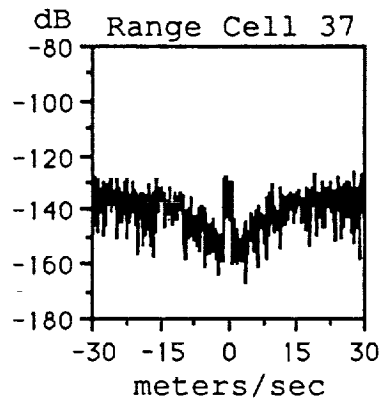
LITERATURE CITED

1. Fujita, T. Theodore, <u>The Downburst</u>. The University of Chicago, Department of the Geophysical Sciences, 1985.

2. Bracalente, Emedio M., Jones, R. William, and Britt, Charles L., "Airborne Doppler Radar Detection of Low Altitude Windshear," Presented at the AIAA Conference on Sensor and Measurement Techniques for Aeronautical Application, Atlanta, Georgia, September 7-9, 1988.

3. Morris, Guy V., <u>Airborne Pulsed Doppler Radar</u>. Norwood, Massachusetts: Artech House, 1988.

4. Doviak, Richard J., and Zrnic', D. S., <u>Doppler Radar and Weather Observations</u>. Orlando, Florida: Academic Press, 1984.

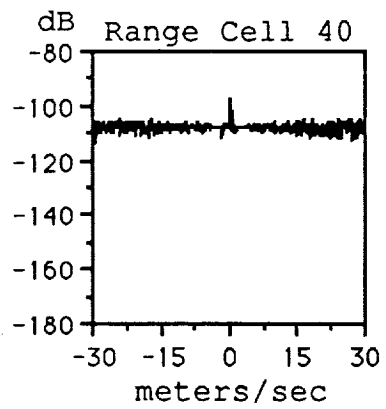5. Rummler, W. D., "Introduction of a New Estimator for Velocity Spectral Parameters," Bell Telephone Labs, Whippany, New Jersey, Tech. Memo. MM-68-4121-5, 1968.

6. Sitterle, Jeffrey J., "Estimation of Spectral Momentes in Small Wavelength Doppler Weather Radar," Master's Thesis, Clemson University, Clemson, South Carolina, August 1983.

7. Bowles, R. L., and Targ, R., "Windshear Detection and Avoidance: Airborne Systems Perspective," Presented at the 16th Congress of the ICAS, Jerusalem, Israel, August 28 - September 2, 1988.

8. Haykin, Simon, Currie, Brian W., and Kesler, Stanislav B., "Maximum-Entropy Spectral Analysis of Radar Clutter," Proceedings of the IEEE, Vol. 70, pp. 953 - 962, September 1982.

9. Gibson, C., and Haykin, S., "Radar Performance Studies of Adaptive Lattice Clutter-Suppression Filters," IEE Proceedings, Vol. 30, pp. 357 - 367, August 1983.

10. Haykin, Simon, <u>Adaptive Filter Theory</u>. Englewood Cliffs, New Jersey: Prentice-Hall, 1986.

11. ____, _Modern Filters_. New York, New York: Macmillian, 1989.

12. Marple Jr., S. Lawrence, _Digital Spectral Analysis with Applications_. Englewood Cliffs, New Jersey: Prentice Hall, 1987.

13. Park, Jinwoo, "Spectral Analysis of Time Series Using Periodogram and Maximum Entropy Methods," Master's Thesis, Clemson University, Clemson, South Carolina, August, 1983.

14. Friedlander, Benjamin, "Lattice Filters for Adaptive Processing," Proceedings of the IEEE, Vol. 70, pp. 829 - 867, August 1982.

15. Kay, Steven M., and Marple Jr., Lawrence Stanley, "Spectrum Analysis - A Modern Perspective," Proceedings of the IEEE, Vol. 69, pp. 1380 - 1418, November 1981.

16. Symons Jr., Frank W., "The Complex Adaptive Lattice Structure," IEEE Transactions on Acoustics, Speech, and Signal Processing, Vol. ASSP-27, pp. 292 - 294, June 1979.

17. Griffiths, L. J., "A Continuously Adaptive Filter Implemented as a Lattice Structure," Proceedings IEEE Conference ASSP, pp. 683 - 686, May 1977.

18. Honig, Micheal L., and Messerschmitt, David G., _Adaptive Filters_. Hingham, MA: Kluwer Academic Publishers, 1984.

19. Akaike, H., "Power Spectrum Estimation through Autoregression Modeling Filtering," Ann. Inst. Stat. Math., vol. 21, pp. 407 - 419, 1969.

20. ____, "A New Look at the Statistical Model Identification," Automatic Control, vol. AC-19, pp. 716 - 723, December 1974.

21. Davis, Willie T., "The Effects of Clutter-Rejection Filtering on Estimating Weather Spectrum Parameters," Master's Thesis, Clemson University, Clemson, South Carolina, August 1989.

22. Lee, Daniel T., Morf, Martin, and Friedlander, Benjamin, "Recursive Least Squares Ladder Estimation Algorithms, " IEEE Transactions on Acoustics, Speech, and Signal Processing, Vol. ASSP-29, pp. 627 - 641, June 1981.

23.   Miller, Kenneth S., <u>Complex Stochastic Processes</u>.
Reading, Massachusetts: Addison Wesley, 1974.